FLOW FIELD AND PERFORMANCE CHARACTERIZATION OF A TWO-DIMENSIONAL CONSTANT-AREA AIR/AIR EJECTOR OPERATED AT DIFFERENT LEVELS OF PRIMARY UNDEREXPANSION

By

MAXIMINO F. DUFFLOCQ

A DISSERTATION PRESENTED TO THE GRADUATE SCHOOL
OF THE UNIVERSITY OF FLORIDA IN PARTIAL FULFILLMENT
OF THE REQUIREMENTS FOR THE DEGREE OF
DOCTOR OF PHILOSOPHY

UNIVERSITY OF FLORIDA

1996

UNIVERSITY OF FLORIDA LIBRARIES

Copyright © 1996

by

Maximino F. Dafflocq

To the memory of my father Adrian Dufflocq G.,

and to Jo Ann

ACKNOWLEDGMENTS

I would like to express my appreciation to Professor Vernon P. Roan, my committee chairman and advisor, for all his help during the conception and planning stages of this investigation and through the entire project. His vision proved essential in defining the research goals, and his expert guidance was instrumental to the successful completion of this effort.

I also would like to thank the other members of the supervisory committee, Dr. William E. Lear, Dr. Jim Klausner, Dr. Elmer C. Hansen, and Professor Ulrich H. Kurzweg, for their participation in this project. In particular, I want to thank Dr. Klausner, who facilitated much of the instrumentation used in the investigation.

I wish to give special thanks to Professor Emeritus Calvin C. Oliver for his interest in this project, for the insightful conversations we had, and for all his very helpful suggestions.

The implementation of the experimental facility was possible in part by grant NAG3-1187 awarded by the Propulsion Systems Branch of the NASA Lewis Research Center, and also by additional funding provided by the Department of Mechanical Engineering. These sponsorships are gratefully acknowledged.

I also would like to acknowledge and thank the staff at the Engineering Machine Shop: Carl Cox, Herman Bailer, Charles Simmons, Tommy Skipper, and Dale Wilcox, for all their help in the fabrication of the hardware. In particular, I want to thank Charles for his

superior machining skills and for the patience he showed every time I presented to him a rather unusual—if not unworkable—hardware design. Likewise, I would like to thank Dr. Jiri Tlusty, who facilitated the CNC machining capabilities of the Machine Tool Research Center for the fabrication of the contoured nozzle and plenum walls, and his graduate assistant William Cobb, who laboriously performed this time-consuming task.

Many others deserve credit for their role in making this investigation possible. Among them is fellow graduate student and coworker Michael A. Benjamin, who patiently developed the computerized data-acquisition and test-control system and worked with me in the development of the experimental facilities. The assistance provided in the laboratory by electronics technician Robert Harker and machine-shop technicians Jeff Studstill and Howard Purdy is greatly appreciated. Students assistants Michael Ferguson, Doug Hyland, Michael Cowles, Bradley Chung, Reed Strickland, Stephanie Webb, Mitch Stokes, Chris Covington, Greg Brase, and Brian Holloway also contributed in different ways to this effort, and their help is appreciated.

Lastly, I want to thank my wife Jo Ann, who for seventeen months endured (among other tribulations) many hours of commuting on Interstate 75, so that we could pretend being married on weekends. Her love, understanding, and endless optimism helped me through the times when "the light at the end of the tunnel" seemed so hopelessly dim.

TABLE OF CONTENTS

page

ACKNOWLEDGMENTS iv

LIST OF TABLES x

LIST OF FIGURES xi

NOMENCLATURE xviii

ABSTRACT xxiii

CHAPTERS

1 INTRODUCTION 1

2 LITERATURE SURVEY 8

- 2.1 Shear-Layer Development 9
  - 2.1.1 Incompressible Shear Layers 9
  - 2.1.2 Compressible Shear layers 11
- 2.2 Underexpanded Flows: Free Jets and Ejectors 18
  - 2.2.1 Acoustic Emissions in Underexpanded Free Jets 19
  - 2.2.2 Aeroacoustic Interactions in Underexpanded Ejectors 28
- 2.3 Ejector Background 31

3 EXPERIMENTAL INVESTIGATION 38

- 3.1 Scope of Investigation 38
- 3.2 Test Matrix 39
- 3.3 Test Facilities 41
  - 3.3.1 Gas Storage and Delivery System 43
  - 3.3.2 Ejector Test Section 46
    - 3.3.2.1 Primary and secondary plenums 46
    - 3.3.2.2 Primary nozzle 51
    - 3.3.2.3 Mixing tube 54
  - 3.3.3 Traversing Impact Pressure Probe 58
  - 3.3.4 Schlieren Visualization System 61

- 3.3.5 Vacuum Exhaust System 64
- 3.4 Instrumentation 66
  - 3.4.1 Total Temperature Measerements 67
  - 3.4.2 Pressure Measurements 67
    - 3.4.2.1 Total pressure 68
    - 3.4.2.2 Static pressure 68
    - 3.4.2.3 Impact pitot pressure 70
  - 3.4.3 Microphone for Acoustic Measurements 70
- 3.5 Test Procedure and Run Sequence 74
  - 3.5.1 Adjustment of Flow Conditions and General Test Procedures 74
  - 3.5.2 Pressure Traverse Runs 76
  - 3.5.3 Manometer Measurements Runs 77
  - 3.5.4 Acoustic Measurements Runs 79
  - 3.5.5 Mixed Measurements Runs 80
  - 3.5.6 Run-Control Code 80

4 EXPERIMENTAL RESULTS 84

- 4.1 Measured Flow Conditions 84
  - 4.1.1 Pitot-Pressure Traverse and Side Wall Pressure Test Series 85
  - 4.1.2 Acoustic Measurements and Schlieren Test Series 88
- 4.2 Schlieren Visualization 92
  - 4.2.1 Ideally Expanded Test Case 92
  - 4.2.2 Underexpanded Test Cases 100
  - 4.2.3 Measurements Obtained from Schlieren Visualization 102
- 4.3 Pitot-Pressure Traverses 105
  - 4.3.1 Pitot Pressure Total Pressure and Flow Speed 106
  - 4.3.2 Primary and Secondary Exit Flows 108
  - 4.3.3 General Observations from Pitot-Pressure Traverses 111
    - 4.3.3.1 Ideally expanded test case 123
    - 4.3.3.2 Underexpanded test cases 126
  - 4.3.4 Repeatability of the Pitot-Pressure Traverses 129
- 4.4 Side-Wall Static Pressure Measurements 129
  - 4.4.1 Centerline Side-Wall Pressure 131
  - 4.4.2 Off-Center Side-Wall Pressure 139
- 4.5 Acoustic Measurements 140
  - 4.5.6 Streamwise Acoustic Measurements 140
  - 4.5.7 Comparison of Measurements from Opposite Walls 155
- 4.6 Effect of Pressure Probe on Test Measurements 155
  - 4.6.1 Flow Visualization with Probe Installed 158
  - 4.6.2 Side-Wall Pressures 158
  - 4.6.3 Acoustic Emissions 163

5 FLOW FIELD DEVELOPMENT AND EJECTOR PERFORMANCE 168

- 5.1 Mass Flow Rates and Ejector Entrainment 168
- 5.2 Streamwise Variation of Flow Speed 170
- 5.3 Shear-layer Growth Rate and Development 179
  - 5.3.1 Growth Rates for the Ideally Expanded Test Case 180
  - 5.3.2 Shear Layer Development for the Underexpanded Test Cases 190
  - 5.3.3 Sonic Lines of the Shear Layers 194
  - 5.3.4 Variation of Static Pressure Across the Flow Field 200
- 5.4 Ejector Performance 205
  - 5.4.1 Ideal Ejector Performance 206
  - 5.4.2 Exit Flow Model 206
  - 5.4.3 Calculation of Exit Properties and Actual Ejector Performance 210
  - 5.4.4 Ideal and Actual Exit Properties and Performance 213
- 5.5 Summary of Effects of Primary Underexpansion 222
  - 5.5.1 Effects of Primary Underexpansion on Flow Field Development 223
  - 5.5.2 Effects of Primary Underexpansion on Acoustic Emissions 224
  - 5.5.3 Effect of Primary Underexpansion on Mixing and Ejector Performance 226

6 CONCLUSIONS AND RECOMMENDATIONS 228

- 6.1 Conclusions 228
- 6.2 Recommendations 235

APPENDICES

A INSTRUMENTATION SPECIFICATIONS MEASUREMENT ERRORS 237

- A.1 Instrumentation Specifications 237
- A.2 Measurement Errors 239
  - A.2.1 Flow Conditions and Mass Flow Rates 240
  - A.2.2 Pitot Pressures 241
  - A.2.3 Side-Wall Pressures 241

B SUMMARY OF TEST MEASUREMENTS 243

C EQUATIONS AND CALCULATIONS 246

C.1 Manometer Side-Wall Pressure Calculations 246
C.2 Mass Flow Calculations 246
C.3 Mach Number Calculations 249
C.4 Predicted Exit Flow Properties 250
C.5 Average Exit Flow Properties 257

REFERENCES 262

BIOGRAPHICAL SKETCH 270

LIST OF TABLES

Table		page
3.1	Nominal test conditions for test matrix	42
3.2	Specifications of the flow-conditioning perforated plates (A – upstream, B – downstream)	50
4.1	Flow conditions for the pitot-pressure traverse test series	86
4.2	Flow conditions for the side-wall pressure test series	87
4.3	Flow conditions for the sound measurements test series	89
4.4	Flow conditions for the Schlieren test series	90
4.5	Comparison of predicted and measured flow conditions in regions of maximum expansion	104
5.1	Mass flow rates and entrainment ratios computed from orifice plate and plenum measurements	169
B.1	Pitot-pressure traverses made with long brass walls installed upstream	243
B.2	Pitot-pressure traverses made with long brass walls installed downstream	244
B.3	Streamwise positions used for acoustic measurements ($z = 0$ for all cases)	245

LIST OF FIGURES

Figure		page
1.1	Representation of a supersonic/subsonic ejector flow field	3
2.1	Feedback loop for acoustic self-excitation of a shear layer in a jet	21
3.1	Ejector test section	40
3.2	Schematic of the high pressure gas storage and delivery system	44
3.3	Primary and secondary plenums	47
3.4	Primary nozzle blocks	53
3.5	Ejector mixing tube and traversing impact-pressure probe	55
3.6	Side wall pressure plate	57
3.7	Disassembled impact-pressure probe	59
3.8	Schematic of the Schlieren system	62
3.9	Schematic of the vacuum exhaust system	65
3.10	Microphone used for sound measurements (a) microphone installation in brass plug (b) complete microphone assembly	71
3.11	Schematic of DC power supply for microphone	73
3.12	Photograph of the 30-column mercury manometer	78
4.1	Schlieren photographs for test case 1 (a) knife edges parallel to the main flow direction (b) knife edges perpendicular to the main flow direction (c) knife edges perpendicular to the main flow direction and probe installed	93

Figure page

4.2 Schlieren photographs for test case 3
(a) knife edges parallel to the main flow direction
(b) knife edges perpendicular to the main flow direction 94

4.3 Schlieren photographs for test case 5
(a) knife edges parallel to the main flow direction
(b) knife edges perpendicular to the main flow direction
(c) knife edges perpendicular to the main flow direction and probe installed 95

4.4 Schlieren photographs for test case 7
(a) knife edges parallel to the main flow direction
(b) knife edges perpendicular to the main flow direction 96

4.5 Schlieren photographs for test case 9
(a) knife edges parallel to the main flow direction
(b) knife edges perpendicular to the main flow direction 97

4.6 Schlieren photographs for test case 11
(a) knife edges parallel to the main flow direction
(b) knife edges perpendicular to the main flow direction 98

4.7 Structure of the supersonic core in an underexpanded ejector for inviscid flow 101

4.8 Representation of a typical pitot-pressure traverse in an ejector flow-field 107

4.9 Pitot-pressure traverses made at the exit plane (x = 0) 109

4.10 Pitot-pressure traverses for test case 1 112

4.11 Pitot-pressure traverses for test case 2 113

4.12 Pitot-pressure traverses for test case 3 114

4.13 Pitot-pressure traverses for test case 4 115

4.14 Pitot-pressure traverses for test case 5 116

4.15 Pitot-pressure traverses for test case 6 117

4.16 Pitot-pressure traverses for test case 7 118

4.17 Pitot-pressure traverses for test case 8 119

Figure	page
4.18 Pitot-pressure traverses for test case 9	120
4.19 Pitot-pressure traverses for test case 10	121
4.20 Pitot-pressure traverses for test case 11	122
4.21 Comparison of repeated pitot-pressure traverses made in the region $21.8 \le x / H_{e\,nozzle} \le 26.6$ for test case 1	125
4.22 Comparison of repeated pitot-pressure traverses made in the region $21.8 \le x / H_{e\,nozzle} \le 31.3$ for test case 5	128
4.23 Comparison of pitot-pressure traverses made in runs for which the flow conditions were independently adjusted	130
4.24 Streamwise side-wall pressure distribution for test case 1	132
4.25 Streamwise side-wall pressure distribution for test case 2	132
4.26 Streamwise side-wall pressure distribution for test case 3	133
4.27 Streamwise side-wall pressure distribution for test case 4	133
4.28 Streamwise side-wall pressure distribution for test case 5	134
4.29 Streamwise side-wall pressure distribution for test case 6	134
4.30 Streamwise side-wall pressure distribution for test case 7	135
4.31 Streamwise side-wall pressure distribution for test case 8	135
4.32 Streamwise side-wall pressure distribution for test case 9	136
4.33 Streamwise side-wall pressure distribution for test case 10	136
4.34 Streamwise side-wall pressure distribution for test case 11	137
4.35 Acoustic spectra for different microphone positions and a 20 kHz band pass for test case 1	141
4.36 Acoustic spectra for different microphone positions and a 20 kHz band pass for test case 2	142

Figure page

4.37 Acoustic spectra for different microphone positions and a 20 kHz band pass, for test case 3 143

4.38 Acoustic spectra for different microphone positions and a 20 kHz band pass for test case 4 144

4.39 Acoustic spectra for different microphone positions and a 20 kHz band pass for test case 5 145

4.40 Acoustic spectra for different microphone positions and a 20 kHz band pass, for test case 6 146

4.41 Acoustic spectra for different microphone positions and a 20 kHz band pass, for test case 7 147

4.42 Acoustic spectra for different microphone positions and a 20 kHz band pass, for test case 8 148

4.43 Acoustic spectra for different microphone positions and a 20 kHz band pass for test case 9 149

4.44 Acoustic spectra for different microphone positions and a 20 kHz band pass, for test case 10 150

4.45 Acoustic spectra for different microphone positions and a 20 kHz band pass, for test case 11 151

4.46 Comparison of acoustic emissions measured on opposite walls at two different streamwise positions for test case 1 156

4.47 Comparison of acoustic emissions measured on opposite walls at two different streamwise positions, for test case 3 156

4.48 Comparison of acoustic emissions measured on opposite walls at two different streamwise positions, for test case 5 156

4.49 Comparison of acoustic emissions measured on opposite walls at two different streamwise positions, for test case 7 157

4.50 Comparison of acoustic emissions measured on opposite walls at two different streamwise positions for test case 9 157

Figure page

4.51 Comparison of acoustic emissions measured on opposite walls at two different streamwise positions, for test case 11 157

4.52 Comparison of side-wall pressure measurements obtained with and without the probe installed, for test case 1 159

4.53 Comparison of side-wall pressure measurements obtained with and without the probe installed, for test case 5 160

4.54 Comparison of side-wall pressure measurements obtained with and without the probe installed, for test case 9 161

4.55 Comparison of acoustic emissions measured with and without the probe installed for test case 1 164

4.56 Comparison of acoustic emissions measured with and without the probe installed, for test case 5 165

4.57 Comparison of acoustic emissions measured with and without the probe installed for test case 9 166

5.1 Flow rates versus normalized exit primary pressure for the pressure traverse, side-wall pressure, and sound measurements test series 171

5.2 Entrainment ratio versus normalized total primary pressure for the exit-plane ($x / H_{e,nozzle} = 34.5$) traverse runs 172

5.3 Streamwise variation of Mach number for test case 1 173

5.4 Streamwise variation of Mach number for test case 2 173

5.5 Streamwise variation of Mach number for test case 3 173

5.6 Streamwise variation of Mach number for test case 4 174

5.7 Streamwise variation of Mach number for test case 5 174

5.8 Streamwise variation of Mach number for test case 6 174

5.9 Streamwise variation of Mach number for test case 7 175

5.10 Streamwise variation of Mach number for test case 8 175

Figure page

5.11 Streamwise variation of Mach number for test case 9 175

5.12 Streamwise variation of Mach number for test case 10 176

5.13 Streamwise variation of Mach number for test case 11 176

5.14 Pitot-pressure traverses for test case 1,
normalized using similarity parameters 182

5.15 Shear-layer boundaries and sonic lines for test case 1 186

5.16 Local shear-layer thickness and growth rates for test case 1 186

5.17 Normalized shear-layer growth rates for two-dimensional
ejector shear layers and constant-pressure mixing layers 188

5.18 *Near field* variation of *plume* width 193

5.19 Comparison of sonic lines in the *near field* 196

5.20 Sonic line for test case 1, normalized using similarity parameters 199

5.21 Sonic-line variation with core Mach number for test case 1 199

5.22 Grid used for computation of the average properties at the mixing-tube exit 211

5.23 Average exit static pressure versus normalized total primary pressure 214

5.24 Average exit velocity versus normalized total primary pressure 214

5.25 Average off-center side-wall pressure distribution for test cases
(a) 1 through 7, and (b) 5, and 8 through 11 216

5.26 Skewness factors for the flow at the mixing-tube exit 218

5.27 Average ejector pressure ratio versus
(a) normalized total primary pressure
(b) entrainment ratio 219

5.28 Thrust augmentation versus entrainment ratio 221

5.29 SMEE versus entrainment ratio 221

C 1 Spanwise velocity distributions assumed at the mixing tube exit 261

C 2 Approximate spanwise velocity distribution in the *near field* for test case 1 261

NOMENCLATURE

Symbol		Description
A	–	Area
A_{o2}	–	Area of orifice plate (Equation C.2a)
A_{wet}	–	Wetted area of mixing tube (in Equation C.26)
AR	–	Nozzle aspect ratio W_t / H_t
c	–	Speed of sound (or defined constants; see "Others" below)
c_p	–	Specific heat at constant pressure
C_f	–	Turbulent wall friction coefficient
C_d	–	Orifice-plate discharge coefficient (Equations C.2a and C.2c)
C_p	–	Pressure coefficient
d	–	Diameter
D_h	–	Hydraulic diameter of mixing tube
f_1	–	Flow function (Equation C.20)
f	–	Frequency
F_1	–	Constant (Equation C.2c)
F_2	–	$1 / d_1$ (Equation C 2c)
f_3	–	Impulse function (Equation C 42)
F_3	–	Impulse function at mixing-tube exit (Equations C 40 and C 41)
$\mathcal{F}(\beta)$	–	Function of β (Equation C 2d)
F_f	–	Friction force in the x direction (Equations C 26 and C.28)
F_x	–	Net force in the x direction (Equations C 11b C 21, C 25 and C 26)
h_0	–	Stagnation or total enthalpy (Equation C 14 C.22)
h	–	Amplitude of cosine-shaped wall (also enthalpy, Equations C.11c and C 14)
h_{ref}	–	Height of reference manometer column (Equation C 1)
h_x	–	Height of manometer column (Equation C 1)

H – Height

$H_{e\,nozzle}$ – Exit height of the primary nozzle investigated

$H_{t\,nozzle}$ – Throat height of the primary nozzle investigated

k – Constant in Prandtl's eddy viscosity (Equation 2.1)

ℓ – Wave length of cosine-shaped wall

ℓ_{cell} – Cell spacing in underexpanded jet

ℓ_v – Mean vortex spacing in shear layers

$L_{m.t.}$ – Length of mixing tube

$\dot{m}$ – Mass flow rate

M – Mach number

M_c – Convective Mach number

M_r – Relative Mach number

M_w – Molecular weight

n – Constant in power of spanwise velocity profile (Equations 5.10)

P – Pressure

P_0 – Stagnation or total pressure

P_{ref} – Reference pressure for manometer (Equation C.1)

P_s – Static pressure (also side-wall pressure measurement, Equation C.1)

Q – Input heat rate (Equation C.11c)

r – Velocity ratio, V_2 / V_1

R – Overall pressure ratio P_0 / P_{amb}

r_p – The plenum total-to-exit static pressure ratio, P_0 / P_s (Equations C.6 and C.8)

Re_{D_h} – Reynolds number based on the mixing-tube hydraulic diameter

Re_d – Reynolds number based on the pipe diameter d_1 (Equation C.2c)

R_u – Universal gas constant

s – Density ratio, ρ_2 / ρ_1

SMEE – Stagnation Momentum Exchange Effectiveness

T – Temperature

T_0 – Stagnation or total temperature

u – Velocity component in the x direction

V – Velocity
V_c – Convective velocity
V_{wall} – Average velocity at the edge of boundary layer at station 3 (Equation C 27)
w_λ – Uncertainty of any property λ
W – Width (e g width of nozzle, secondary stream mixing-tube etc)
W_{sh} – Shaft work (Equation C 11e)
x – Streamwise coordinate of flow field (see Figure 3 1)
y – Transverse coordinate of flow field (see Figure 3 1)
Y – Orifice plate expansion factor (Equations C.2a and C 2b)
z – Spanwise coordinate of flow field (see Figure 3 1)

Greeks Description

α – Mach angle
α_1 – Skewness of mass flux or first moment (Equation C 23c)
α_2 – Skewness of momentum flux or second moment (Equation C 23d)
α_3 – Skewness of energy flux or third moment (Equation C.23e)
β – Diameter ratio of orifice plate d_2 / d_1 (Equations C.2a, C.2b, C.2c, and C 2d)
δ – Local thickness of compressible shear layer
δ' – Compressible shear layer growth rate
δ_0 – Local thickness of incompressible shear layer
δ_0' – Incompressible shear-layer growth rate
δ_ω – Local vorticity thickness of shear layer
δ_ω' – Shear-layer growth rate based on vorticity thickness of shear layer
Δ – Change in quantity, or finite quantity
ϵ – Empirical constant in incompressible growth rate (Equations 2 11 and 2 12)
ε – Skewness of temperature at mixing-tube exit (Equation C 23f)
Φ – Thrust augmentation
γ – Specific heat ratio
η – Transverse similarity coordinate or similarity variable
θ_i – Initial momentum thickness of the boundary layer

κ_1 – Defined constant (Equation C.38)

λ – Velocity parameter (Equations 2.2c) or sound wavelength

μ – Ejector entrainment ratio, $\dot{m}_2 / \dot{m}_1$

ν_t – Turbulent eddy viscosity

ξ_1 – Defined constant in friction term (Equation C.29)

π – Normalized pitot-pressure

ρ – Density

σ – Constant in similarity coordinate η (or spreading parameter, Equation 2.2b)

σ_0 – σ for $V_2 / V_1 = 0$

ω – Width of *plume*

ω_0' – Growth rate of *plume*

ψ – Stream function

Subscripts Description

1 – Pertaining to primary (or faster) stream or at primary exit plane

2 – Pertaining to secondary (or slower) stream, or at secondary exit plane

3 – Pertaining to flow at mixing-tube exit, or at mixing-tube exit plane

5% – At outer edge of shear layer (traditional definition)

15% – At outer edge of shear layer and plume (new definition)

95% – At inner edge of shear layer (traditional definition)

I, II, III – Regions in an ideal underexpanded primary core (Figure 4.7)

a – Upper secondary (on positive y side of primary)

amb – Pertaining to ambient conditions

ave – Average of upper and lower secondary streams

b – Lower secondary (on negative y side of primary)

cr – Critical value at M = 1

d – Design

e – Exit

f.e. – Fully expanded condition

F1 – Fundamental or first harmonic

hi – Harmonic i ($i = 2, \ldots 5$; $i = 2$ second harmonic or first overtone, etc.)

j – Area-element counter in the transverse direction (Figure 5.22)

k – Area-element counter in the spanwise direction (Figure 5.22)

max – Maximum quantity

min – Minimum quantity

o1 – Pertaining to a condition upstream of the orifice plate (Equation C.2a)

o2 – Pertaining to a condition at the orifice plate (Equation C.2a)

pit – Based on pitot-pressure measurements

vis – Based on visual observations

∞ – Denoting free-stream conditions outside the shear layer

Others Description

c_1 – Conversion factor, Equation C.1 (also speed of sound of stream 1)

c_2 – $\sqrt{2M_w\gamma/\left(R_uT_0(\gamma-1)\right)}\,A_e$, Equation C.6 (also speed of sound of stream 2)

c_3 – $(\gamma - 1)/\gamma$ (Equation C.6)

c_4 – $(\gamma+1)/(2\gamma)$ (Equation C.6)

c_5 – $(\gamma - 1)/2$ (Equation C.8)

$\bar{}$ – Barred quantities denote area-average at mixing tube exit

Abstract of Dissertation Presented to the Graduate School
of the University of Florida in Partial Fulfillment of the
Requirements for the Degree of Doctor of Philosophy

FLOW FIELD AND PERFORMANCE CHARACTERIZATION OF A TWO-DIMENSIONAL, CONSTANT-AREA, AIR/AIR EJECTOR, OPERATED AT DIFFERENT LEVELS OF PRIMARY UNDEREXPANSION

By

Maximino F. Dufflocq

August 1996

Chairman: Vernon P. Roan
Major Department: Mechanical Engineering

An experimental investigation was conducted to study the effect of primary jet underexpansion on the flow-field development and performance of a low-entrainment ratio, constant-area, two-dimensional ejector. In the flows investigated, both the primary and secondary streams were unheated air and had nominal Mach numbers $M_1 = 1.80$ and $M_2 = 0.35$, respectively. The primary supply pressure was varied among the test cases, resulting in primary-to-secondary exit static-pressure ratios between 1.0 (ideally expanded) and 1.7. The secondary exit static pressure was approximately 34.5 kPa in all test cases.

Pitot-pressure, side-wall static pressure, and acoustic emissions were measured at several axial locations along the mixing tube. These measurements were complemented with Schlieren visualization. The test results were used to characterize shear-layer development in the region before the free-streams are completely entrained--the *near field*. The ejector

performance based on flow measurements was compared to a reference based on complete mixing of the two streams

In the ideally expanded flow case the shear layers closely resemble those in planar, constant-pressure two-stream flows, they have uniform boundaries and similar growth rates The shear layers in the underexpanded cases have a zigzag shape, as they adapt to the expansion and contraction of the core At high underexpansion, the shear layers are pushed far into the secondary free-stream However, despite the substantial differences in local flow structure, the spatial shear-layer growth at the end of the *near field* is similar in all cases

High-intensity, narrow-band screech was detected in the *near field* of most underexpanded flow cases. Peak screech intensities occurred at an exit static pressure ratio of 1 27, reaching sound pressure levels of 153 db and exhibiting a fundamental frequency (f_{F1} = 3 0 kHz) and up to four higher harmonics

Performance was always lower than the ideal no-loss prediction, and in general decreased with increasing underexpansion due to lower entrainment ratios and more incomplete mixing However mixing was enhanced in the case with peak screech intensities, resulting in mixing-tube average exit properties that were closer to the fully mixed predictions and relatively better ejector performance

The *near-field* supersonic-core boundaries were found for all cases, and the results fit well within the flow field characterization

CHAPTER 1
INTRODUCTION

Ejectors have been of interest to the engineering community since the turn of the century. The interest in these devices is due to their potential to perform fluid work in a wide array of applications, and to do so in a simple, maintenance-free, and cost effective fashion. The ability of an ejector to do work stems from the fact that when a fluid jet--the primary--is discharged in to a duct, it entrains or draws with it fluid--the secondary--from the immediate surrounding. There are several consequences to this process which include (a) the removal of fluid from the surroundings, (b) an increase in pressure (momentum) of the entrained fluid, and (c) an increase in the rate of linear momentum flux over that of the primary jet alone.

Ejectors have been of recent interest in the aircraft industry where they have been considered for thrust augmentation in vertical and short take-off landing (V/STOL) aircraft (Bevilaqua, 1974; Quinn, 1973; Nagaraja, 1973), and for cooling (Federspiel and Kuchar, 1988; Lotfy and Hamed, 1992) and noise reduction (Long, 1992) in jet-engine exhaust systems. Other applications have included fluid extraction such as for removal of gas vapor from storage tanks (Dutton and Carroll, 1983) and pumping of the fuel and oxidant in chemical lasers (Dutton et al., 1982).

Even though ejectors rank among the simplest fluid-flow devices, their flow fields are rather complex and offer significant challenges insofar as analysis is concerned. A representation of a typical constant-area supersonic/subsonic ejector flow is shown in

Figure 1.1. These mixing flows are characterized by several regions of viscous interaction all of which play a major role on the ejector performance. Among these regions, the shear layers between the primary and the secondary streams are of much interest, for it is in here where the initial transport and exchange processes between the two streams takes place. The shear layers develop in the initial region where portions of both the primary and secondary streams continue to coexist. This region is defined here as the *near field* and is the subject of much of this investigation. In Figure 1.1 the *near field* thus corresponds to the flow region between x_0 and x_1.

The mixing process continues in the mixed flow region, which begins where the primary and secondary have been completely entrained by the shear layers (x_2 in Figure 1.1). The extent of mixing at the end of the shroud or mixing tube has a direct impact on the overall performance of the ejector, as does the length of tube necessary to achieve the mixing. The main effect of the boundary layers is to degrade performance through friction losses. The geometry of the mixing tube, the primary and secondary inlets, and any diffuser included at the exit are also known to play important roles in the performance of an ejector.

Traditionally, ejector flows have been analyzed using the conservation equations and a control volume approach. Frequently, the analysis has been simplified by treating the flow as inviscid and one-dimensional. These formulations are attractive from a mathematical simplicity standpoint, but usually predict performance far superior to that measured in the laboratory. In some cases more sophisticated analyses have been employed, in which nonideal effect such as viscous dissipation and incomplete mixing are taken into account by utilizing various semi-empirical models and have resulted in considerably better agreement with experimental data. However, their value as design tools is limited because the models

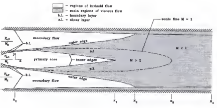

Figure 1.1 Representation of a supersonic/subsonic ejector flow field

often fail to accurately represent the flow over wide range of flow conditions and ejector geometries.

One of the main challenges encountered in the analysis and design of ejectors is that of finding a suitable mixing length or, more specifically, determining the geometry of the mixing tube. The inability of most (if not all) existing ejector analyses to accurately provide this information represents one of the primary voids in ejector theory.

The growth rate of the turbulent shear layers between coflowing streams, whether in ejectors or other types of shear flows, is a useful indicator of how fast the streams mix. For this reason, shear layers have received much attention during the last three decades. Recent interest in ramjet technology sparked numerous efforts to investigate shear layers of very high Reynolds number flows (Dimotakis, 1989; Goebel and Dutton, 1990; Papamoschou, 1986, for example). These investigations were motivated by earlier studies which had shown that compressibility appeared to inhibit shear layer development, and a primary objective was to isolate the effect of compressibility on growth rates and turbulence.

Most studies have involved two-stream planar mixing layers where the pressure is purposely kept constant and pressure waves are minimized or eliminated through careful design of the experimental apparatus. In ejectors, on the other hand, the pressure typically varies and pressure waves are practically unavoidable when the primary flow is supersonic. Therefore, the ejector shear layers are subject to different boundary conditions. Further, in most practical ejector flows one stream is completely entrained before the other (usually the primary) and, therefore, ejector shear layers are less likely to be characterized by a single growth rate. Only a few studies can be found which consider in detail ejector shear layers (Roan, 1993 and 1992; Benjamin, 1994, for example).

Perhaps an even bigger challenge than finding the length required for mixing is finding a length which also minimizes friction and results in a compact design. The tradeoff between better mixing and increased friction is well known to ejector designers. To optimize a design, one must identify the length beyond which gains obtained from better mixing are curtailed by the friction losses associated with the additional wetted surface (Quinn, 1973).

A few ejector studies have shown that mixing can be accelerated by operating the primary above the critical pressure (Hsia, 1984; Quinn, 1976). In short ejectors the faster mixing thus obtained has led to an increase in performance (Quinn 1976). The test results suggest that the faster mixing in ejectors is provoked by aeroacoustic interactions similar to those responsible for increasing the spreading rate of underexpanded jets. The powerful discrete-like acoustic emissions or screech generated by underexpanded jets have been directly linked to the faster dissipation of these jets. Powell (1953a, b)--the first one to study this phenomenon--identified a self-sustaining acoustic feedback loop as the mechanism responsible for the increase in spreading rate of these jets. The available data shows that in ejectors the acoustic feedback loop may be strongly influenced by the resonant modes of the mixing-tube.

There have been numerous experimental investigations, at least matched in number by analytical studies, to characterize the flow field and the flow generated noise in supersonic jets (Seiner and Yu, 1984; Pao and Seiner, 1983; Tam and Tanna, 1982; Norum and Seiner, 1982; Harper-Bourne and Fisher, 1973, for example). These efforts have been motivated primarily by the need to understand and reduce the broadband shock-associated noise from jet engine exhausts and, as a result, their scope has been limited to the study of axisymmetric free jets (i.e. constant boundary-pressure flows).

Progress in ejector technology largely depends on being able to accurately analyze these flows. Even the most sophisticated shear- and jet-flow analyses available today, most or all of which are zero-pressure gradient, fail to provide accurate representations of the viscous regions. This type of representation can only be achieved through a full understanding of the physical processes that govern these flow fields, and in particular the mixing processes.

In most efforts to investigate the effects of primary underexpansion and acoustic interactions in ejectors, the primary objective has been to characterize the nature of these emissions and/or to measure the overall effect of these interactions on mixing and performance. However, no attempts have been made to characterize in detail the shear layers and the flow field, with the exception of measurements normally obtained at the mixing-tube exit. Further, to the author's knowledge, no detailed measurements have been obtained for two-dimensional ejectors with supersonic nozzles.

As a result of this apparent deficiency, an experimental investigation was conducted to characterize in detail the mean flow field in a two-dimensional ejector. For this investigation, the primary was supplied by a Mach 1.8 contoured nozzle, and supply pressures were selected to provide for cases with different levels of primary underexpansion. The main objectives of this effort were to:

(1) develop and implement a suitable experimental test facility,

(2) obtain a detailed database for a limited number of flow cases,

(3) characterize the shear layer development for cases with different primary pressures, particularly in the *near field*,

(4) compare shear layer development among the different flow cases,

(5) measure the flow-generated acoustic emissions,

(6) compare the measured and predicted ejector performance, and

(7) correlate the results to determine what conditions can lead to improved ejector performance.

To accomplish these objectives a large number of measurements were made along the entire length of the ejector mixing tube These included measurements of pitot pressure traverses, side wall pressures, and acoustic emissions Continuous light-source Schlieren visualization was also implemented to provide an unambiguous description of the mean flow fields.

In addition, an extensive number of tests were conducted to validate the data base These included experiments to (a) determine the repeatability of the measurements, and (b) characterize and quantify the intrusiveness of the impact pitot probe

CHAPTER 2
LITERATURE SURVEY

The are many processes which can individually or collectively shape the flow field and affect the performance of any ejector. Among those which have greatest impact on the flow is the nature of the mixing of the primary and secondary streams. The mixing process is initiated in the turbulent shear layers which develop between the two streams. The development of these viscous layers depends on a large array of variables including the free-streams flow conditions and their initial turbulence levels. Shear-layer development can also be influenced by pressure gradients such as those which occur in ducted flows or in flows where pressure waves are present. Similarly compressibility effects which arise from differences in density or temperature, or from high flow Mach number can also have a significant effect. Shear layers have been studied extensively and are well understood, although most studies are for conditions of zero pressure gradient.

Flow generated acoustic emissions can also play an important role in the development of the shear layers. These emissions originate from turbulent eddies and therefore, their occurrence in the flow field is directly related to the nature of the shear layers. In ejectors where the primary flow is supersonic the appearance of pressure waves in the flow field is practically unavoidable. Further in the presence of strong compression waves (shocks), strong acoustic emissions can also result from the interaction of turbulent eddies with these shocks. The majority of such studies of acoustic interactions provides little detail on the shear-layer development.

A survey of these and other relevant aspects of ejector flows is presented in this chapter

2 1 Shear Layer Development

Shear layers represent one of the most extensively treated subjects in fluid mechanics Birch and Eggers (1973) provide an extensive review of the early experimental studies on subsonic and supersonic shear layers, and also summarized some of the first analytical solutions obtained A survey of several analytical and experimental studies on incompressible and compressible shear layers is presented in the sections below

2 1 1 Incompressible Shear Layers

Several solutions have been obtained for the mean velocity profile across an incompressible shear layer One such solution was derived by Görtler in 1942, and is discussed by Schlichting (1979) In obtaining this solution Görtler applied the usual boundary-layer continuity and momentum equations to a free shear layer and introduced Prandtl s kinematic eddy viscosity (exchange coefficient hypothesis)

$$\nu_t = \delta_0 k \left(V_1 - V_2 \right) \qquad \text{where} \quad \delta_0 = \delta_0' \left(x \quad x_0 \right) \tag{2 1}$$

to model the Reynolds stress He then transformed the equations using the similarity variable $\eta = \sigma y / x$ and the incompressible stream function

$$\psi = x \frac{V_1 + V_2}{2} F(\eta) \tag{2 2a}$$

where the constants σ and λ are given by

$$\sigma = \frac{1}{2\sqrt{k \delta_0' \lambda}} \tag{2 2b}$$

and

$$\lambda = \frac{V_1 - V_2}{V_1 + V_2} \tag{2.2c}$$

After combining the transformed equations he obtained the differential equation

$$F'''(\eta) + 2\sigma^2 F(\eta) F''(\eta) = 0 \tag{2.3a}$$

which he then solved subject to the boundary conditions

$$\begin{aligned}
&(1)\; y \to +\infty \;(\eta \to +\infty) && \to \quad V = V_1 && (F' = 1 + \lambda) \\
&(2)\; y = -\infty \;(\eta \to -\infty) && \to \quad V = V_2 && (F' = 1 - \lambda) \\
&(3)\; y = 0 \quad (\eta \to 0) && \to \quad V = \frac{V_1 + V_2}{2} && (F' = 1)
\end{aligned} \tag{2.3b}$$

where the subscripts 1 and 2 refer to the high and low velocity streams, respectively. Görtler obtained the following series solution

$$V(x,y) = \frac{V_1 + V_2}{2}\left(1 + \lambda\left(\sigma\frac{y - y_0}{x - x_0}\right) + \ldots\right) \tag{2.3c}$$

In this result, y_0 is the transverse distance satisfying the third boundary condition, and x_0 is the virtual origin of the shear layer. The constants σ and λ (Equations 2.2b and 2.2c) are known as the spreading and the velocity parameters, respectively.

Implied in Görtler's solution (Equation 2.3c) is that the shape of the velocity profile across the incompressible shear layer is self-preserving and similar, irrespective of streamwise position, as long as the shear layer is fully developed and similar. The incompressible shear layer growth rate obtained from this solution is

$$\delta_0' = \frac{1}{\sigma} \tag{2.4}$$

Abramovich (1963) and Sabin (1965) obtained independently the same expression for the constant σ. Their result is

$$\frac{\sigma_0}{\sigma} = \frac{V_1 - V_2}{V_1 + V_2} = \lambda \tag{2.5}$$

where σ_0 is the value of σ for $V_2 / V_1 = 0$ (i.e. for $\lambda = 1$). Several different expressions were obtained by others for the expression relating σ to λ (Miles and Shih, 1968, and Yule, 1972, for example). However, the experimental data for fully developed, homogeneous, subsonic shear layers is best represented by Equation 2.5. The constant σ_0 was determined experimentally by several investigators, and a value of 11 seems to result in good agreement with the data. Equations 2.4 and 2.5 lead to the well-known result

$$\delta_0' = \lambda \quad \text{or} \quad \delta_0' = \text{const}\,\frac{V_1 - V_2}{V_1 + V_2} \tag{2.6}$$

2.1.2 Compressible Shear Layers

Although Görtler's solution provided a building block for shear-layer theory and helped explain the early experimental measurements, it failed to account for the effect of density changes encountered in heterogeneous shear layers. Several experimental studies have shown that homogeneous and heterogeneous shear layers having similar flow velocities can exhibit different free-stream entrainment rates. Among these studies are those of Konrad (1976), Brown (1974), and the well-known investigation by Brown and Roshko (1974).

Dimotakis (1986) derived approximate expressions for the entrainment and growth rate in heterogeneous, subsonic, planar mixing layers, from considerations regarding the coherent structures or eddies which are convected in the shear layer. These structures have been observed experimentally in turbulent shear layers (Dimotakis and Brown, 1976, Brown and Roshko, 1974, Winant and Browand, 1974) and their mean local vortex spacing appears to be a constant of the flow.

In his formulation, Dimotakis noted that a stagnation point exists between each vortex pair in relation to a Galilean frame of reference moving with the vortices (as proposed by Coles 1985), and that the flow is approximately steady along a line through this point Based on these considerations, he applied Bernoulli's equation (in the Galilean frame) to both sides of the shear layer and, after noting that pressure is approximately constant across the shear layer he obtained the following expression

$$\sqrt{s} = \frac{1-r_c}{r_c-r} \tag{2.7}$$

In this expression, s, r, and r_c are the density ratio ρ_2 / ρ_1, the velocity ratio V_2 / V_1 and the normalized convective velocity V_c / V_1, respectively

Dimotakis argued that the volumetric *induction* into the shear layer between two contiguous vortices is proportional to the product of the local *induction* velocity and vortex spacing. He also argued that the shear-layer growth should be linear in time and equal to the growth between vortex pairs Based on these considerations he a developed model for the entrainment between vortices and introduced Equation 2.5 as well as correlations for the mean vortex spacing ℓ_v (Koochesfahani et al., 1979)

$$\frac{\ell_v}{x} = 3.9\frac{\delta_\omega}{x} \tag{2.8}$$

and the vorticity thickness δ_ω (Brown and Roshko 1974)

$$\frac{\delta_\omega}{x} = 0.17\frac{1-r}{1+r} \tag{2.9}$$

Dimotakis obtained the following approximate expressions for the mass entrainment ratio and the growth rate of a heterogeneous shear layer

$$E_m = \frac{1}{\sqrt{s}}\left(1+0.68\frac{1-r}{1+r}\right) \tag{2.10}$$

$$\frac{\delta_0}{x} = \epsilon\left(\frac{1-r}{1+\sqrt{s}\,r}\right)\left(1+\sqrt{s}-\frac{1-\sqrt{s}}{1+2.9(1-r)/(1+r)}\right) \tag{2 11}$$

In Equation 2 11, ϵ is a proportionality constant introduced to match the predicted results with the experimental measurements For homogeneous shear layers (i e s = 1) Equation 2 11 reduces to Görtler's solution (Equation 2.6.)

Similar expressions have been developed by others for the incompressible growth rate Papamoschou (1986) assumed that the growth rate is proportional to $(V_1 - V_2) / V_c$ After introducing the convective velocity as given by Equation 2.7, Papamoschou arrived at the expression

$$\frac{\delta_0}{x} = \epsilon\,\frac{(1-r)(1+\sqrt{s})}{1+\sqrt{s}\,r} \tag{2.12}$$

Goebel and Dutton (1990) defined the velocity parameter as $\lambda = (V_1 - V_2) / (2V_c)$ and then introduced the convective velocity given by Equation 2.7 The resulting expression has the same form of Equation 2.12 and differs only by a factor of 0.5

The practical value of all these expressions depends on the availability of a suitable proportionality constant A survey of the literature quickly reveals that there are almost as many different reported values for this constant as there are studies To this extent it has been argued (Birch and Eggers, 1973) that the discrepancies which can be quite large in some instances are largely due to the lack of a standard criteria for obtaining growth rate data. In many instances the growth rate measurements have been obtained in regions where the shear layer has clearly not reached fully developed conditions Bradshaw (1966) found that for a free-jet shear layer the distance to a fully developed condition is somewhere in the region $500\,\theta_i \le x \le 1000\,\theta_i$, where θ_i is the initial momentum thickness of the boundary layer at the trailing edge of the splitter plate. This criterion has been widely accepted to date.

Birch and Eggers state that the problem is compounded by the almost unavoidable differences in the initial conditions of the boundary layer, and also by the use of different definitions of shear layer thickness. For example, Brown and Roshko (1974) estimated the growth rates from visual measurements of the spreading rate, δ'_{vis}, of the homogeneous shear layers (i.e $s = 1$) and found that $\epsilon = 0.38$ for a free jet (i.e. $\lambda = 1$), or

$$\delta'_{vis} = 0.38\,\frac{1-r}{1+r} \tag{2.13}$$

This is more than twice the result they found using vorticity thickness (Equation 2.7), and partly explains the commonly adopted criteria that $\delta'_{\omega} = 0.5\delta'_{vis}$.

Similarly, in an effort to consolidate his results with others, Papamoschou (1986) estimated that $\delta'_{pit} = 0.8\delta'_{\omega}$ (based on his definition of pitot thickness δ_{pit}). He combined this approximation with Brown and Roshko's results and obtained $\epsilon = 0.14$ for the constant in Equation 2.11, for measurements based on pitot pressure (this result is adopted in the present study for growth-rate calculations presented in Chapter 5).

A different type of density effect which has been of much interest for its implications on gas-turbine design is that of compressibility due to high Mach numbers. It has been known for some time that the growth rate of a high-Mach number shear layer is somewhat reduced relative to a low-speed shear layer having similar density and velocity ratios. This behavior has also surfaced stability analyses of shear layers (Blumen, 1970 and Blumen et al., 1975). Although there have been several theoretical and experimental studies on this subject, there is little agreement on how to best predict this effect. One of the main reasons for the limited understanding of these high-speed flows is the lack of experimental data needed to confirm the proposed models. To experimentally isolate Mach number effects, a test facility must be capable of supporting the use of dissimilar gases and also the use of heated flows. Such facilities present considerable design challenges based on complexity, cost, and safety considerations.

Many of the early analytical studies on the effect of compressibility used Howarth-Dorodnitsyn-type transformations to convert the compressible domain into the incompressible one for which the solution was already known. Roan (1966) used this approach to predict the velocity profile across a two-stream shear layer for zero and small positive and negative flow angles of the subsonic stream. He obtained good agreement with his experimental measurements. While this approach is convenient from a mathematical standpoint and leads to reasonable results, it does not separate the different density effects--that is, effects due to different composition, different temperature, and Mach number.

Despite the lack of a single universally accepted theory, most agree that the Mach-number compressibility effect on growth rate is a function of the relative convective velocity or convective Mach number of the structures in the shear layer. Brown and Roshko (1974) estimated that the growth rate for a free-jet shear layer depends on Mach number according to

$$\delta' \sim \sqrt{\frac{\Delta V}{V}\frac{1}{M}} \tag{2.14}$$

where V, ΔV, and M are the mean streamwise velocity, the fluctuation of the streamwise velocity, and the mean Mach number of the shear layer, respectively. Bogdanoff (1983) was perhaps the first one to propose the convective Mach number as a correlation parameter for growth rates Papamoschou (1986) measured the growth rates of heterogeneous, high Mach shear layers and correlated his measurements with the convective Mach number Using arguments similar to those used by Dimotakis (1986) he found the convective Mach number of the structures in the shear layer by equating total pressures at the assumed stagnation point between vortices He obtained

$$\left(1+\frac{\gamma_1-1}{2}M_{c_1}^2\right)^{\frac{\gamma_1}{\gamma_1-1}} = \left(1+\frac{\gamma_2-1}{2}M_{c_2}^2\right)^{\frac{\gamma}{\gamma_2-1}} \tag{2 15}$$

where the convective Mach numbers are defined by

$$M_{c_1} = \frac{V_1-V_c}{c_1} \qquad M_{c_2} = \frac{V_c-V_2}{c_2} \tag{2.16}$$

When the convective Mach numbers are not very large and the specific heat ratios are not substantially different, and the pressure across the shear layer is approximately constant, Equation 2.15 reduces to

$$V_c = \frac{1+r\sqrt{s}}{1+\sqrt{s}}V_1 \tag{2 17}$$

which is another form of Equation 2.7 In the special case where $\gamma_1 = \gamma_2$, Equation 2 15 leads to

$$V_c = \frac{c_1V_1+c_2V_2}{c_1+c_2} \tag{2.18}$$

In addition, Papamoschou hypothesized that the growth rate of compressible shear layers can be expressed as

$$\delta' = F\left\{r\ s\ \gamma_2/\gamma_1\ M_c\right\} \tag{2 19}$$

In correlating his measurements with M_{c_1} he normalized the measured growth rates by the those predicted by Equation 2.12 for the corresponding density and velocity ratios, thus he calculated

$$\frac{\delta'}{\delta'_0} = \frac{F\left\{r, s, M_{c_1}\right\}}{F\left\{r, s, M_{c_1} = 0\right\}} \tag{2.20}$$

The dependence on specific heat ratios has been dropped from this expression because it is relatively small. He found that the data collapsed approximately onto one curve despite the significant variation in density ratios, and concluded that the *normalized growth rate* is only a function of convective Mach number, namely

$$\frac{\delta'}{\delta'_0} = F\left\{M_{c_1}\right\} \tag{2.21}$$

Dimotakis (1989) suggests that the *normalized growth rate* is represented well by the function

$$F\left\{M_c\right\} = 0.2 + 0.8\,e^{-2M_c^2} \tag{2.22}$$

A curve fit obtained by Benjamin (1990) shows that a value of 3 for the multiplier of the convective Mach number represents more closely the available data.

Goebel and Dutton (1990) measured mean velocity distributions and turbulence levels in planar two-stream mixing layers using Laser Doppler Velocimetry (LDV). They used the relative Mach number

$$M_r = 2\frac{V_1 - V_2}{c_1 + c_2} \tag{2.23}$$

to correlate *normalized growth rates*. Their results exhibit the same trend observed by Papamoschou (1986). The main difference results from using a different constant to predict the incompressible growth rate ($\epsilon = 0.0825$ instead of $\epsilon = 0.14$ in Equation 2.12).

There are considerably fewer experimental studies of shear layers in ejector flow fields. Among the few that can be found are those of Roan et al. (1993 and 1992). Roan and his coworkers measured the growth rates of shear layers in the initial region of axisymmetric and two-dimensional ejector flows. They considered flows with similar and dissimilar primary and secondary gases The reducing effect of compressibility is also evident from their measurements (Dufflocq et al., 1993), and the growth rates in their two-dimensional ejector flows are similar to those generally reported for planar constant pressure mixing layers Their results seem to indicate that the axisymmetric ejector shear layers grow considerably faster perhaps twice as fast, as their two-dimensional counterparts However, it is difficult to make an absolute comparison from their measurements The primary flow in the two-dimensional ejector was approximately parallel to the secondary flow, while in the axisymmetric ejector the primary flow was supplied by a conical nozzle and thus the flow near the trailing edge was inclined relative to the secondary

Benjamin (1994) conducted a detailed experimental investigation of a perfectly expanded ejector flow and measured turbulent and static side-wall pressures as well as pitot pressures. He measured growth rates in the initial region of the flow which are comparable to those in constant-pressure mixing layers

2.2 Underexpanded Flows, Free Jets and Ejectors

The acoustic emissions generated by supersonic jets and their interaction with the flow field have been the subject of analytical and experimental investigations since the 1940's. Traditionally most investigations have been motivated by the desire to minimize or reduce unwanted high intensity emissions from jet engine exhausts (Dosanjh et al., 1969 Bishop et al., 1971 Norum 1983 for example) This continues to be an area of main concern for engine designers, who today face increasingly more demanding noise regulations

On the other hand it has also been found that the screech generated in underexpanded jets can have a positive effect on ejectors in terms of mixing enhancement and overall performance. Naturally, screech emissions may be undesirable in applications where the ejector discharges directly into unconfined surroundings, such as in V/STOL aircraft. However, in situations where the device is an internal component, it would not only be feasible but also desirable to exploit any acoustic interaction that results in increased performance. In the following sections some of the most prominent studies on the subject are reviewed.

2.2.1 Acoustic Emissions in Underexpanded Free Jets

That sound impinging on a laminar jet can induce a more rapid transition to turbulence was observed as early as 1935 by Brown, although his observations involved only external sound sources. Powell (1953a, b) was perhaps the first one to study the nature of flow-generated screech and explain the aeroacoustic interactions. In his study of underexpanded free jets from two-dimensional and axisymmetric convergent nozzles, he observed that the sound from these jets changed considerably as the nozzle pressure was raised above its critical value. For high pressures he measured strong sound waves (perhaps of up to 165 db) emanating from the jet, and found that these emissions have dominant near-discrete frequencies, unlike the aerodynamic noise normally associated with turbulent jets which has a more continuous spectrum.

Powell was able to capture the sound waves in still Schlieren images and observed that they originate in anti-phase from both sides of the jet and propagate primarily in the upstream direction. He also found that turbulent disturbances appear in an alternating anti-symmetric pattern on either side of the jet, at the end of the initial laminar region, and observed that there was a noticeable increase in the angle of spread of the jet.

Powell determined that the wavelength of the dominant frequencies, λ_f, are closely related to the pressure of the jet, and follows the empirical relation

$$\frac{\lambda_f}{d} = \begin{cases} 5\sqrt{R-R_{cr}} & \text{(two-dimensional)} \\ 3\sqrt{R-R_{cr}} & \text{(axisymmetric)} \end{cases} \tag{2.24}$$

where d is either the diameter or the smaller dimension of the nozzle, R is the overall pressure ratio and R_{cr} is the critical pressure ratio. Further, he found that the spacing (ℓ_{cell}) of the shock-cells in the underexpanded jet follows the empirical relation

$$\frac{\ell_{cell}}{d} = 1.89\sqrt{R-R_{cr}} \tag{2.25}$$

and that therefore the wavelength is proportional to the shock-cell spacing.

Using geometrical considerations Powell (1953a) suggested a mechanism whereby the alternating turbulent disturbances produce sound upon their interaction with the shock waves of the cellular pattern. Thus several sources interact to form a highly directional sound field, in which the strongest emissions propagate upstream and have a fundamental frequency identical to the turbulent disturbances in the shear layers (the fundamental frequency is given by $f_F = c / \lambda_F$ and Equation 2.24). The upstream traveling sound waves in turn impinge upon the edge of the initial laminar jet boundary and introduce new disturbances. The model closely explained his measurements and is in agreement with theoretical expressions for the directionality of the fundamental frequency and the first harmonic in a three-source model. Powell's feedback loop is represented schematically in Figure 2.1.

In the case of the axisymmetric jet Powell (1953b) also observed that at some pressures, the dominant frequencies change in a discrete-like fashion, suddenly increasing

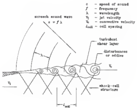

Figure 2.1 Feedback loop for acoustic self excitation of a shear layer in a jet

and then decreasing once again with increasing pressure Powell suggested that this anomaly was caused by the changes in the cellular pattern

Similar observations were made by Hammitt (1961) in a jet from a two-dimensional convergent nozzle Using shadowgraph visualization he observed that the jet oscillates when it is underexpanded, generating semicircular sound waves from either side The jet also appeared to spread more rapidly Like Powell, he found that the frequency of the sound waves decreased as pressure was increased, with the exception of small jumps in frequency which he suggested result due to a switch between modes of oscillation Hammitt observed that by covering the nozzle exit with sound-absorbing material the frequency jumps were almost eliminated and the peak intensities occurred at different pressures He concluded that the jet oscillations are sensitive to the external sound waves Hammitt also correlated the wavelength of the sound waves with the cell spacing

Davies and Oldfield (1962a, b) used spark Schlieren visualization to measure in detail the structure of the cellular pattern and the wavelength of the screech emissions in a jet emanating from an axisymmetric convergent nozzle From their measurements they concluded that several sources may be responsible for generating screech, and that these sources appear to be located between the 4th and 7th cells, at the end of the cells They also observed sudden jumps in screech frequency (in agreement with Powell and Hammitt) and found that these jumps indeed coincide with small but unmistakable shifts in the cell pattern (as first suggested by Powell) In addition, their measurements indicate that at low pressures the turbulent disturbances develop into toroidal vortices and the resulting radiation is symmetric on both sides of the jet In contrast, at higher pressures long helical vortices develop around the jet and are convected downstream, and the radiation is anti-symmetric.

Westley and Wooley (1968) conducted a similar detailed study, and also correlated the screech emissions with the shock-cell pattern in an underexpanded axisymmetric jet. They found that different modes of screech (i.e. different frequencies) are linked to different cells in the core, and all modes peak between the third and sixth cell. Using a spark Schlieren visualization system capable of spark synchronization and phase delay, they obtained still images and motion pictures of the jet and were able to characterize the evolution of the disturbances and the development of the shocks in each mode. Westley and Wooley observed a symmetric screech mode of low frequencies generated by axisymmetric eddies at low nozzle pressures, and an asymmetric mode of high frequencies generated by spiraling eddies at high pressures (in direct support of the results obtained by Davies and Oldfield 1962a).

Poldervaart et al. (1968) observed a jet from a choked converging nozzle using Shlieren visualization and high-speed motion pictures. They observed clearly the jet oscillating and screech being generated near the third cell, thus providing conclusive evidence about the origin of screech. Further, by placing reflective surfaces at the nozzle exit they were able to increase the oscillation through *forced* screech. Poldervaart et al. proposed a feedback loop model which explains their measurements for different reflector positions, and supports further Powell's screech mechanism.

Glass (1968) considered the effect of flow-generated screech on the spreading rate of jets from axisymmetric convergent nozzles. He tested a nozzle with an exit diameter of 12.7 mm at pressures ratios between R = 2 and R = 5, and measured intense screech with a frequency of approximately 10 kHz near R = 4. Glass observed that by placing a shield around the jet at different positions, thus preventing the screech from reaching the initial region of the jet he could change considerably the rate of velocity decay in the streamwise direction (again in support of Powell's model). In the absence of the shield, he measured a decrease of up to 50% in centerline velocity at a distance of 20 nozzle diameters as well as an increase of almost 100% in jet diameter.

Rosfjord and Toms (1975) studied the effect of temperature on free-jet screech and found that in general the screech frequency increased with temperature except near the frequency discontinuities previously observed at ambient temperatures. This result is in agreement with Powell's model (1953a) insofar as higher jet temperatures lead to higher convective velocities in the shear layers (since $V_c \approx M_j$) which in turn lead to more frequent interactions between the turbulent disturbances and the shocks in the cellular pattern. They also observed that screech intensity decreased at higher temperatures. Rosfjord and Toms present a semi-empirical expression to predict the effect of temperature.

Considerably fewer studies can be found which have considered the acoustic characteristics of underexpanded two-dimensional jets. Viets et al. (1981) studied jets from two-dimensional convergent nozzles with aspect ratios of 2.0, 5.0 and 16. They measured screech consisting of a fundamental frequency (in the 2 kHz – 16 kHz range) and higher-order harmonics and found that for some nozzle pressures the first harmonic becomes the dominant frequency. Viets et al. observed shifts in screech frequency for the nozzle with small aspect ratio similar to the shift previously observed for axisymmetric nozzles (Powell 1953b; Davies and Oldfield, 1962a, etc). Their frequency data fits Powell's correlation (Equation 2.24) reasonably well, and their results provide evidence of faster mixing (similar to that reported by Glass, 1968) at pressure ratios between R = 3.1 and R = 3.45 for all three nozzles.

A more detailed experimental study of two-dimensional jets from convergent nozzles was conducted by Krothapalli et al. (1983 and 1982). They found that screech tones occur at all pressure ratios between R = 2.7 to R = 5.4. At pressure ratios in the range R = 3 to R = 4 they observed several distinct features, including an increase in the spread angle of the jet, higher intensities for the fundamental screech frequency, and large-amplitude oscillations of the shock-cells. It was observed that cylindrical sound waves originate alternately near the end of the third cell, where the latter breaks up as a result of the jet oscillations.

Krothapalli et al. also found that the Strouhal number corresponding to the peak screech amplitude was 0.12. After examining the available data for two-dimensional underexpanded jets they determined that the Strouhal number for the maximum screech radiation always falls between 0.11 and 0.14 (and between 0.24 to 0.28 for axisymmetric jets), which is close to the most anti-symmetric and unstable modes in incompressible jets. Based on their visualization experiments, they suggested that for these conditions, vortices enter the shock cell and interact with the normal shocks at the end of the cells.

More recently Gutmark et al. (1990) also investigated a convergent nozzle (aspect ratio AR = 3) for pressure ratios corresponding to fully expanded Mach numbers between $M_{f.e.} = 1$ and $M_{f.e.} = 2.4$. They observed an asymmetric flapping motion of the jet on the minor axis plane as the nozzle is underexpanded, while the major axis remained approximately symmetric. The flapping motion resulted in higher spread rates of the jet in this plane, with the maximum spread rate occurring near pressure ratios for $M_{f.e.} = 1.5$ (i.e. R = 3.67). The pressure fluctuations were also found to be much higher at the minor plane, and the strongest fluctuations corresponded to the screech emissions propagated upstream (as predicted by Powell's directionality analysis, 1953a). Gutmark et al. found that as the pressure is increased further ($4.94 \leq R \leq 6.70$ or $1.7 \leq M_{f.e.} \leq 1.9$) the flapping motion no longer occurred and the spread rate was reduced, although the jet still spread at higher rates than a jet with $M_{f.e.} = 1$.

There are very few studies pertaining to jets from supersonic nozzles. Most of these studies involved axisymmetric jets and were motivated by an increasing need to understand broadband shock noise from aircraft exhausts (Tam et al., 1985, Dash et al., 1985 and Seiner et al., 1985, Norum and Seiner 1982, Tam, 1972, Harper-Bourne and Fisher, 1973, Tanna, 1977, for example). In most experimental investigations there was a conscious effort to eliminate the strong screech component from the sound spectrum in order to isolate the broadband emission. The broadband shock-noise has been attributed to a weaker interaction between the large-scale structures and the shock-cell system (Tam and Tanna, 1982).

Yu and Dosanjh (1972) investigated the directionality of screech emissions in a jet from a contoured, axisymmetric, Mach 1.5 nozzle. From their measurements they found that the shock structure in the underexpanded jet significantly increases the high frequency noise, and that discrete emissions (i.e. screech) are found normal to and/or upstream of the jet direction. The similarity with Powell's results suggests that the screech phenomenon is the same (at least qualitatively) in supersonic nozzles as it is in convergent nozzles. Yu and Dosanjh also found that the apparent source of the strongest emissions is located near the middle of the shock-cell region of the core ($1 \leq x / d \leq 9$).

A few very sophisticated numerical solutions which account for turbulence have been developed to predict the shock structure and broadband shock noise in underexpanded free jets (Dash et al., 1985, Seiner et al., 1985, Tam et al., 1985, for example). These solutions provide reasonable agreement with the available data, particularly in the initial region of the jet and near the center The accuracy deteriorates with distance from the jet axis particularly in the viscous shear layers

Tam (1986) developed a linear shock-cell model to predict the structure and the screech tone frequencies of underexpanded jets from two-dimensional and elliptical supersonic nozzles He modeled a slightly underexpanded jet as being surrounded by vortex-sheets (i e the shear layers), and solved the boundary value problem using the method of eigenfunction expansion. From the solution, Tam obtained the following first-order approximations for the shock-cell spacing (ℓ_{cell}) and the screech frequency (f) in a two-dimensional jet

$$\frac{\ell_{cell}}{H} = 2\sqrt{M_{fe}^2-1}\left\{\left[\frac{M_d}{M_{fe}}\left(\frac{1+\frac{\gamma-1}{2}M_{fe}^2}{1+\frac{\gamma-1}{2}M_d^2}\right)^{\frac{\gamma+1}{2(\gamma-1)}}-1\right]\frac{W}{H+W}+1\right\} \tag{2.26a}$$

$$\frac{fH}{V_{fe}} = \frac{1}{2}\frac{V_c}{V_d}\frac{H}{\left(1+V_c/c_\infty\right)\ell_{cell}} \tag{2 26b}$$

In the above expressions the subscripts d and f e denote the design and fully expanded conditions of the jet and H and W are the small and large dimensions of the nozzle, respectively The approximations are valid for $W/H \geq 4$, and provide favorable agreement with measured screech frequencies for choked rectangular jets (i.e $M_d = 1$) by assuming that the convective velocity is $V_c \approx 0.7V_{fe}$ Tam (1986) noted that experimental measurements for nozzles with small aspect ratios are not available and are to needed to confirm any theoretical predictions (which partly explains the motivation behind the present investigation)

2.2.2 Aeroacoustic Interactions in Underexpanded Ejectors

The work of Quinn (1975 1976, and 1977) ranks among the first on acoustic interaction in ejectors He considered an ejector with a convergent primary nozzle 6 75 mm in diameter, and an area ratio $A_2 / A_1 = 25 8$ While studying the effect of mixing tube length in an axisymmetric constant-area ejector over a range of primary pressures and temperatures, he observed unusually high performances for relatively short mixing tubes at pressure ratios ($P_{0,1} / P_{amb}$) near 2 7 and 3 7 Quinn observed that high performance coincided with occurrence of screech tones similar to those detected by Powell (1953b)

By comparing the free-jet (Rosfjord and Toms, 1975) and bounded jet acoustic emissions Quinn found that the screech frequency is substantially different between these cases, with those for the ejector flow in general being higher He also found that over some pressure ratios including those which resulted in improved performance, the ejector screech had a tendency to assume frequencies close to symmetric (16 kHz, 30 kHz) and asymmetric (25 kHz 40 kHz) resonant modes of the circular mixing-tube Quinn observed that at some pressures the screech frequency suddenly shifted to these "preferred" frequencies Succi et al (1978) confirmed that it is possible to excite the transverse acoustic modes in a duct with the noise generated by a turbulent jet.

Quinn observed that flows with improved performance were characterized by an early increase in side-wall pressure and by considerably more uniform velocity and temperature profiles at the mixing-tube exit He determined that the improved performance was a result of faster mixing, and attributed the latter to acoustic interactions similar to those found in free jets Quinn suggests that the effect of this interaction is to inhibit the turbulent energy cascade and intensify the large vortices which entrain fluid into the shear layer This explanation seems reasonable since the first phase of the entrainment process in shear layers (as discussed by Dimotakis 1986) is the *induction* of fluid between large scale vortices.

Quinn explained that the acoustic interaction had a negative effect when long mixing tubes were used. The faster mixing not only leads to higher velocities near the wall, thus resulting in relatively larger friction loses, but effectively extends the length along which these losses occur.

Viets et al. (1981) considered a two-dimensional ejector (area ratio of $A_2 / A_1 = 26$, nearly the same as Quinn's, 1976) with a convergent nozzle (AR = 133) and variable mixing-tube length (L / W = 2 – 11). Viets and coworkers observed acoustic interactions similar to those reported by Quinn. They found that for $L / W \geq 3.8$ screech had a tendency to become tuned to some frequencies, and for some pressures this interaction resulted in peaks of sound pressure levels (SPL). The strongest interactions occured at pressure ratios between 3.2 and 3.5 and always corresponded to a dominant frequency of 15 kHz to 16 kHz. Their measurements showed small improvements in thrust augmentation, which they attributed to more complete mixing.

Hsia (1984) also investigated the effect of screech on the flow field and performance of a two-dimensional ejector. Hsia considered an ejector with a convergent nozzle (AR = 10) and a constant area mixing tube with adjustable height (resulting in $7.4 \leq A_2 / A_1 \leq 35.4$ and $16.7 \geq L_{m.t.} / H \geq 3.84$). Upon increasing the mixing-tube height at a fixed pressure, he observed that the dominant screech frequency decreased gradually until a critical height was reached. Beyond that critical height the frequency suddenly jumped to a new higher level and then decreased, and the process was repeated. Hsia adapted the feedback loop developed by Poldervaart et al. (1968) to the geometry of his ejector, and found that the new model predicts well the trend observed for the variation of frequency with geometry. He concluded that the nature of the acoustic interaction is the same in bounded jets as it is in free jets.

Hsia also found that the ejector screech decreased in stages as the pressure was increased, while the screech frequency for a free jet from the same nozzle decreased continuously (in agreement with results obtained by Quinn, 1976, and Viets et al., 1981). However, in contrast to Quinn's results for the axisymmetric ejector geometry, he found that the frequency stages occurred only near asymmetric resonant mixing-tube modes. Hsia reports improved mixing and performance for pressure ratios between 3.7 and 4.4, which correspond to the lowest and most powerful frequency stage.

With the aid of a self-synchronizing Shlieren system, Hsia was able to observe flow structures previously undetected in ejector flows. By taking multiple-exposure Shlieren photographs with the light source triggered at the dominant screech frequency, he was able to visualize standing waves which closely match the excited modes of the mixing-tube. Further, by selectively choosing lower synchronization frequencies, he observed large-scale groups of structures in which the individual structures travel at different velocities but as a group the structures are convacted at the same velocity.

More recently, Tam (1993) used linear stability theory to predict the most unstable disturbance waves in free and ducted turbulent jets, motivated by knowledge that these waves represent an essential element of Powell's feedback loop. His analysis showed that the most unstable waves occur over a limited frequency band, and based on this result he suggests that screech frequencies must lie within this frequency range for the feedback loop to produce high screech intensity. He explains that the screech frequency is largely dictated by the feedback loop in free jets and by the resonant duct modes in bounded jets. According to

Tam the jumps in screech frequency often reported can be explained by a switch in the most unstable waves in the jet—a switch from axisymmetric to helical instability mode.

Tam's analytical predictions also seem to explain the measurements obtained by Rosfjord and Toms (1975) As the temperature of the jet is increased, the frequency of the most unstable waves decreases while the opposite is true for screech frequencies. Thus the waves and screech move towards a mismatch in frequencies and the intensity of the screech decreases

A search of the literature reveals that there is a void of experimental data on the screech interaction in supersonic ejectors Barna (1971) considered an axisymmetric ejector configuration with conical convergent-divergent primary nozzles The results reported include pumping performance and overall sound power level as a function of primary Mach number and primary pressure. However, Barna provides no details about effects on mixing, the spectral nature of the sound emissions or the probable location of the screech sources

Mamin et al (1971) also conducted a limited investigation on axisymmetric free and ducted jets from supersonic nozzles. The results reported include empirical expressions for the cell spacing and screech frequency, estimates of the convective velocity of disturbances and screech directionality predictions They also found a resonant condition in the ejector Their results are in general agreement with those reported for convergent nozzles

2 3 Ejector Background

Ejectors have been the subject of experimental and analytical studies for many years and, as a result, there is a wealth of literature with a near endless list of entries The general fundamental behavior of these devices is well understood and numerous analytical solutions with different levels of sophistication have been developed which provide reasonable predictions of performance trends. Porter and Squyers (1978, 1979) give a comprehensive review of ejector theory which includes in excess of 1600 references. The background provided next is only a brief review of selected studies and various aspects of high-speed ejector flows in which the primary and secondary streams are gases.

Due to the complexity of ejector flow fields, a number of simplifications are usually adopted to model the real flows, thus making the analysis manageable. Therefore the solutions in general are only valid for a given range of flow conditions, geometry or operating regime. A control-volume approach is often used where the governing equations are solved by introducing assumptions such as adiabatic and/or frictionless flow, constant-pressure or constant-area mixing, uniform inlet flows, fully mixed exit flows, ideal gas, etc. Because most formulations are based on the one-dimensional and/or frictionless assumptions, they fail to predict the length required to achieve a given extent of mixing between the primary and secondary. This obviously represents a major shortcoming from a design standpoint, for among a designer's main objectives could be to build the hardware as compact as possible.

Keenan and Neumann (1950, 1942) are among the first who investigated ejectors analytically and experimentally. As in most ejector studies, they considered an axisymmetric configuration to examine the effect of geometry on performance and used a one-dimensional analysis to predict performance. They considered convergent and convergent-divergent nozzles, constant-area and constant-pressure mixing, and mixing tubes of variable length. Their measurements follow the predicted trends, but as is the case with most analysis of this type, the actual performance falls below the ideal output. Their measurements showed that a mixing-tube length of about seven to eight diameters resulted in the best performance when the mixed flow is subsonic and that the length increases somewhat with primary-to-secondary pressure ratio

Fabri and Siestrunck (1958) investigated experimentally supersonic primary ejectors with cylindrical mixing tubes and proposed analytical solutions to predict their performance. Their analyses are based on the requirement of aerodynamic compatibility between the primary and secondary in the mixing region (i.e. the supersonic jet adjusts to the surrounding pressure, in turn adjusting the secondary flow area) and neglect viscosity and diffusion effects

In developing their models Fabri and Siestrunck identified three distinct flow regimes for high pressure ejectors, which can be described as follows. The *supersonic flow regime* exists when the primary flow remains supersonic through the entire mixing tube. In this regime the primary jet expands as it enters the mixing tube, effectively reducing the secondary flow area and forcing the secondary to become choked at the point of maximum expansion. This condition of aerodynamic choking is commonly known as *Fabri choking*. In the *supersonic flow regime* the conditions in the mixing tube are independent of the those beyond the mixing-tube exit. As the primary pressure is increased further, the choking point of the secondary moves closer to the secondary exit, until eventually the secondary becomes choked at the exit. This condition represents the *saturated supersonic regime*, and corresponds to the maximum entrainment in a supersonic ejector. When the primary pressure is lowered, a point is reached beyond which the secondary never reaches a choked condition, and the supersonic primary eventually breaks down. This scenario corresponds to the *mixed flow regime*. For this type of ejector flow the secondary is entrained by a subsonic primary flow. This characterization of ejector flows represents the basis for many analytical models that are used today.

Chow and Addy (1964) also studied constant-area supersonic ejectors and extended the concepts introduced by Fabri and Siestrunck. Their analysis incorporates the computation of the expansion of the primary jet using the method of characteristics (unlike Fabri and Siestrunck, who used one-dimensional isentropic relations to determine the conditions at the minimum secondary flow area). Their analysis also accounts for the viscous interactions between the two streams in terms of the amount of entrained secondary fluid. This was done by approximating the thin viscous layer as behaving like a constant-pressure incompressible shear layer (Section 2.1.1). Beyond the point of minimum maximum primary expansion their analysis reduces to a one-dimensional solution independent of any viscous interaction between the primary and secondary. Their model can be used to generate performance surfaces which are characteristic of a given ejector design (i.e. M_1 and A_2 / A_1). Chow and Yeh (1965) used the same approach to predict performance in ejectors with variable-area mixing tubes. The analytical approach used by Chow and his coworkers is discused at length by Addy (1972).

Anderson (1974) developed a computer code which calculates the flow in supersonic nozzle ejectors. The code takes into account the finite thickness of the shear layer between the primary and the secondary and also the initial boundary layer thickness of each stream.

A different type of analysis was presented by Hickman et al. (1972) for axisymmetric large area ratio ejectors. In this case the ejector flow field was dividad into regions which include the primary-core, the self-preserving jet, and the developing duct-flow regions. Each region was modeled to obtain the mean flow field in the mixing tube Their analysis allows for different primary and secondary stagnation pressures, either supersonic or subsonic primary and accounts for boundary layer effects (wall friction, reduction of flow area, etc) While their analysis yields reasonable agreement with their measurements for a heated-primary ejector the assumptions and models used greatly limit its range of applicability

Quinn (1976) used a quasi one-dimensional control volume analysis to compute the performance in an axisymmetric ejector Quinn included an empirical friction term in the momentum equation, and also introduced the skewness factors or moments of the exit flow to account for incomplete mixing Quinn also investigated experimentally the effect of primary underexpansion and acoustic interactions on performance (as explained in the previous section), and used the predicted results to evaluate the experimental data.

Addy et al (1981) developed a computer-based one-dimensional model to predict the performance of supersonic ejectors for specified operating conditions Their analysis includes a secondary control volume to determine the limiting secondary flow rate which results in *Fabri choking* The model can provide solutions for cases of constant-area or constant-pressure mixing and for flows with similar or dissimilar gases The code also allows for the inclusion of an exit diffuser Because the model is based on the assumption of inviscid flow its value is limited primarily to parametric studies of ejector performance

Dutton et al (1982) investigated experimentally a supersonic/supersonic ejector in connection with its application to chemical lasers Dutton and his coworkers used the same analysis developed by Addy et al (1981) to predict the performance of their test ejector and found that the predicted performance was 15% to 22% higher than the measured values

The analysis and model developed by Addy et al (1981) was used by Dutton and Carroll (1986) to develop an ejector-optimization computer program. The output of their optimization code can be use to generate three-dimensional performance surfaces similar to those first proposed by Chow and Addy (1964). The surfaces represent the upper limit performance of the ejector and give an estimate the near-ideal ejector design and operating points for a given application requirement.

In measuring ejector performance the choice of parameters depends largely on the application being considered. When the function of the ejector is to entrain or extract fluid from a given space (i.e the secondary), the entrainment ratio, m_2/m_1, is a suitable measure of performance In propulsion applications such as V/STOL aircraft, where the ejector acts as a thrust augmentor, performance can be measured in terms of the thrust augmentation ratio The thrust augmentation ratio Φ is given by

$$\Phi = \frac{\text{ejector thrust}}{\text{primary thrust}} \tag{2.27}$$

If the ejector is used as a fluid pump then ejector pressure ratio $P_{0,3} / P_{0,2}$, is a useful measure of the effectiveness of the ejector

Another ejector performance parameter recently introduced by Roan (1991) is the Stagnation Momentum Exchange Effectiveness (SMEE) Roan postulates that an ejector can be viewed as a compressor Therefore the ejector "goodness" can be measured in terms of the useful compression work performed on the secondary by the primary, relative to the latter's full potential for expansion work Roan explains that a momentum-based performance parameter is a better indicator than one based on energy Based on these observations Roan developed the SMEE parameter, which is given by

$$\mathrm{SMEE} = \frac{c_{p,2}}{c_{p,2}} \sqrt{\frac{T_{0,2}\,\gamma_1\,M_{w,2}}{T_{0,1}\,\gamma_2\,M_{w,1}}} \left(\left(\frac{P_{0,3}}{P_{0,2}} \right)^{\frac{\gamma_2 - 1}{\gamma_2}} - 1 \right) \left(1 - \left(\frac{P_{0,3}}{P_{0,1}} \right)^{\frac{\gamma_1 - 1}{\gamma_1}} \right)^{-1} \frac{\dot{m}_2}{\dot{m}_1} \qquad (2.28)$$

The subscripts 1, 2, and 3 refer to the primary, secondary, and fully mixed exit planes of the ejector (the remaining variables can be found in the nomenclature). Roan explains that SMEE varies roughly between 0.1 and 0.3 and that experimental data shows that for a given ejector design SMEE is usually constant irrespective of design point parameters (i.e. primary and secondary velocities, etc.).

The usefulness of the SMEE parameter was demonstrated by Petersen et al. (1992) and Roan (1991) using data collected by Petersen (1990) for a supersonic-primary ejector with dissimilar primary and secondary gases. It was found that flows with smaller primary-to-secondary molecular weight ratios indeed result in higher performance (i.e. higher SMEE) for a given ejector geometry, as predicted by the SMEE parameter.

In the present investigation the ideal ejector performance was computed using properties obtained with a one-dimensional control volume analysis like the one used by Quinn (1976) and Addy et al. (1981). The formulation is explained in detail in Appendix C Section C.5, and is also discussed in Chapter 5.

CHAPTER 3
EXPERIMENTAL INVESTIGATION

3.1 Scope of Investigation

In the preceding chapter a number of studies were cited which have shown that gains in ejector performance can sometimes occur from increased mixing when the primary stream is operated at above-critical pressure. Some results suggest that flow-generated screech in these flows can influence the early development of the shear layers, hence affecting the overall mixing process. Most of the studies found, however, pertain to ejectors of axisymmetric configuration and/or flows in which the primary has a nominal Mach number near unity. Further, very few report data with the level of detail necessary to more thoroughly understand these flow fields.

Ongoing efforts to include ejector devices in propulsion cycles have prompted interest in the effect of underexpansion in ejectors where the primary flow is supersonic. Of particular interest is the effect of underexpansion on the early development of ejector shear layers (i.e. on mixing) and on overall ejector performance. These effects are the chief motivation behind this work. As a result, the primary objectives of this investigation were (a) to design, build, and instrument an ejector test facility, and (b) to provide detailed experimental data to help further understand how performance is changed when the primary is underexpanded in a supersonic primary/subsonic secondary ejector.

A single two-dimensional ejector geometry was utilized in this study. Here a supersonic rectangular jet (25.4 mm wide by 12.7 mm high) is sandwiched between two identical subsonic jets of similar cross section, and the three co-flowing streams discharge into a constant-area mixing tube of rectangular cross section. Figure 3.1 shows the geometry and scale of the test section, and the reference coordinate system. The study was also limited to cases in which air was the primary and secondary gas, and the primary pressure was the only controlled independent variable. The measurements collected included (1) total (stagnation) pressures and temperatures, (2) mass flow rates, (3) sidewall static pressures, (4) pitot pressure traverses, (5) acoustic spectra and (6) flow visualization.

It is readily recognized that the scope of this investigation was inherently limited considering the endless number of variables which can directly or indirectly govern an ejector flow field. However, narrowing the scope in this fashion was necessary in order to provide enough detailed measurements while still keeping the resulting database manageable.

3.2 Test Matrix

The test matrix consisted of eleven cases which differ in primary stagnation pressure, $P_{0,1}$. In all cases the nominal (design) exit Mach number was $M_1 = 1.5$ for the primary and $M_2 = 0.35$ for the secondary, approximately. The mixing-tube inlet static pressure was kept at 34.5 kPa, within 2.5 percent. This also corresponds to the secondary exit pressure, $P_{s,2}$. Hence, the nominal required total pressure for the secondary, $P_{0,2}$, was 37.5 kPa.

Using sub-atmospheric test-section pressures has two advantages. First, it increases allowable run time by decreasing the flow rates. Secondly, lowering the Reynolds number delays turbulent transition of the shear layer, hence allowing for more detailed observation of early flow development.

The *baseline* test case corresponds to the ideally expanded primary flow, and required a total primary pressure of approximately 200 kPa. For the remaining ten cases the primary

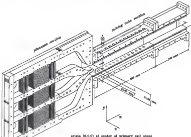

Figure 3.1 Ejector test section

stagnation pressure was increased using a 13.8 kPa increment thus resulting in increasingly higher levels of primary underexpansion. These flow conditions result in primary flow rates between $\dot{m}_1 = 0.10$ kg/s and $\dot{m}_1 = 0.18$ kg/s and a secondary flow rate of $\dot{m}_2 = 0.048$ kg/s. Table 3.1 summarizes the design test conditions for all test cases. The range of primary pressures was chosen based on (a) available data for conditions which result in changes in performance and/or flow generated screech, and (b) the results of earlier exploratory tests.

3.3 Test Facilities

The experimental apparatus used in this investigation incorporated new as well as existing test facilities. Most important in this study was the two-dimensional ejector test section. This test section was designed and built at the University of Florida, Gas Dynamics Laboratory to study shear layer growth in ideally expanded, supersonic/subsonic ejectors with similar and dissimilar primary and secondary gases (Dufflocq et al., 1993). A few modifications were made later to accommodate the needs of this investigation. Among the design criteria were to

(a) provide near uniform two-dimensional primary and secondary exit flows

(b) minimize the flow rates while maintaining a flow scale sufficiently large to allow the flow to remain near two-dimensional in the region immediately following the exit plane--the *near field*, and allow implementation of the desired measurements

(c) facilitate implementation of the different types of instrumentation and number of measurements required, and

(d) provide flexibility for future changes or additions to the hardware while keeping manufacturing difficulty and cost to a minimum

Table 3.1 Nominal test conditions for test matrix

Test Case	$P_{0,1}$ (kPa)	$P_{s,1}$ (kPa)	$P_{s,1} / P_{s,2}$	$\dot{m}_1$(kg/s)	$\dot{m}_2 / \dot{m}_1$
1	198	34.5	1.00	0.104	0.469
2	212	36.9	1.07	0.111	0.439
3	226	39.3	1.14	0.118	0.412
4	240	41.7	1.21	0.126	0.388
5	253	44.1	1.28	0.133	0.367
6	267	46.5	1.35	0.140	0.348
7	281	48.9	1.42	0.147	0.331
8	294	51.3	1.49	0.155	0.315
9	308	53.7	1.56	0.162	0.301
10	322	56.1	1.63	0.169	0.288
11	336	58.5	1.70	0.176	0.277

The air required for the experiments was supplied by a high-pressure gas storage and delivery system. A vacuum exhaust system was installed which provides the low test-section pressures necessary for the investigation and allows relatively short pump-down times. Fine adjustment of the flow rates as well as the exhaust back pressure were necessary to ensure precise and repeatable test conditions.

Air flow through the rig was controlled by the laboratory PC computer, as was the data acquisition. Computer automation allowed for short run times, consistency, and precise instrument readings while minimizing operator error. The remainder of this chapter provides a detailed account of all relevant components of the experimental apparatus and test procedures.

3.3.1 Gas Storage and Delivery System

A schematic of the high-pressure air supply facility is shown in Figure 3.2. The pressurized air used for the primary and secondary flows was supplied by a Worthington two-stage positive-displacement 340-cfm 150 hp (0.160 m^3/s, 112 kW) compressor, which delivers a maximum working pressure of 2070 kPa. The compressed air is passed through several oil and water traps, and through a two-column desiccant air dryer to remove most of the excess moisture. The dry air is then stored in four cylindrical tanks manifolded together and totaling a volume of approximately 6.23 m^3, from where it is used in blowdown mode.

In order to maintain a near constant supply pressure, the compressor was run continuously during tests. Further, to increase consistency of the test conditions, flow rates were adjusted using a preselected supply pressure and runs were initiated at this same level throughout a series of tests. The start-up supply pressure was monitored with a transducer mounted on the supply line and was preselected after a warmup period, once the

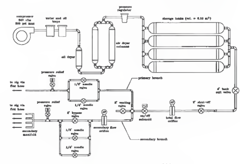

Figure 3 2 Schematic of the high pressure gas storage and delivery system compressor s second stage automatically disengaged upon reaching the maximum pressure A solenoid valve provided for emptying the tanks was used to lower the pressure and force the compressor to refill the tanks whenever the supply pressure dropped below the desired level

Air is delivered to the test rig through a supply line built from schedule-80 steel piping The first section of this supply line is a 2 in pipe sized to keep the Mach number below 0 4 for flow rates up to 27 times higher than those investigated here (for the highest flows considered here M = 0 015) A manual gate valve is used to isolate the pressurized tanks from the test rig when the rig is not used Automatic on/off control of the air flow is accomplished with a solenoid valve placed downstream of the gate valve. The solenoid valve can be controlled manually or electronically using a digital output channel from the computer The total air flow to the rig is measured with a 25 4 mm sharp-edge concentric orifice plate located between the gate valve and the solenoid valve

The primary and secondary air flows are then delivered to the respective plenums by two separate lines, each equipped with flow-control valves The secondary line is a 2 in pipe capped at the downstream end, where four sections of 1 in pipe are welded perpendicular to the line and at 90 degree intervals These smaller pipe sections form a manifold for distribution of the secondary air Four steel reinforced PVC hoses with a 1 in inside diameter connect this manifold to the secondary plenums The secondary flow rate was adjusted with two needle valves installed in parallel a 3/4 in valve used for coarse adjustment and a 1/4 in valve used for fine adjustment A 25 4 mm sharp-edge concentric orifice plate mounted upstream from these valves is used to measured the secondary flow rate

The primary line consists of a 3/4 in pipe connected to the primary plenum with a flexible metal hose of 3/4 in inside diameter The primary air flow was also adjusted with a 3/4 in. needle valve and a 1/4 in needle connected in parallel and was computed based on total and secondary flow measurements.

A pressure relief valve was installed in each line to protect the test section and the instrumentation in case of system malfunction The metal hose and the four PVC hoses connecting the supply lines to the respective plenums help isolate the test section from blowdown-induced vibrations

3.3.2 Ejector Test Section

The ejector test section consists of the primary and secondary plenums, the primary nozzles and secondary exit passages, and the ejector mixing tube or shroud. All hardware components were fabricated using a modular design to facilitate manufacturing and assembly, and to allow for future modifications All parts were machined at the University of Florida using small tolerances to ensure a proper fit and a tight seal among all mating surfaces A detailed description of the various hardware is presented next.

3.3.2.1 Primary and secondary plenums

The primary and secondary plenums consist of flow-conditioning sections followed by settling chambers (Figures 3 1 and 3 3) The primary plenum is in the center, sandwiched between two identical secondary plenums. The plenum walls are machined from aluminum stock and form continuous flow passages of rectangular cross section All flow passages are 25 4 mm wide The primary plenum is 59 7 mm high while the secondary plenums are 71 9 mm high These dimensions ensure that plenum flow velocities are kept between 3 m/s

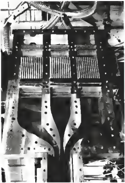

Figure 3.3 Primary and secondary plenums

and 27 m/s (as recommended by Pope and Goin, 1978) for the range of primary flow rates for which the rig was designed.

Two rectangular plates 12.7 mm thick serve as side walls for the flow passages. The remaining walls were machined from 25.4 mm thick aluminum plate. These are internal walls and include (a) the walls separating the primary and secondary plenum cavities, (b) the outer walls of the secondary plenums, and (c) the rear wall for all plenums. Two stainless steel dowel pins inserted through the walls in (a) and (b) and into positioning holes drilled in both side walls accurately position each part of the assembly. All plenum walls are bolted together.

Originally, Dow Corning High-Vacuum grease was used to seal the mating surfaces. However, early experiments showed that this method did not provide an adequate seal and resulted in unacceptable air leaks from the primary plenum and the laboratory space into the secondary plenums. The plenum was reassembled by placing a thin film of Dow Corning Gasket Sealant on the critical surfaces prior to tightening the fasteners. This approach eliminated all significant leaks.

Air enters the plenums through inlet orifices machined on the side walls, one for the primary plenum and one on either side of each secondary plenum. Thick-walled aluminum nipples having a 1.0 in. inside diameter are inserted in these orifices and welded to the side walls, and provide means to connect the hoses to the respective plenums. The PVC hoses are clamped to the secondary nipples, while the metal hose threads into the primary nipple.

Inside each plenum the air first passes through a series of flow management devices including (1) two perforated plates machined from aluminum, (2) a section of aluminum honeycomb, and (3) two stainless steel wire meshes. The perforated plates are 3.9 mm thick and are 12.7 mm apart (16.6 mm from center to center). The upstream plates are 27.4 mm from the centers of the inlet orifices. On the primary side this plate has a 12x5 array of 4.42 mm diameter holes and provides 39% flow-area reduction. On the secondary side the first plates have a 14x5 array of 4.45 mm diameter holes providing 40% blockage.

The second perforated plate on the primary side has a 14x6 array of 3.68 mm diameter holes. On the secondary plenums the downstream plate has a 17x6 array of 3.66 mm diameter holes. The downstream plates result in 41% flow obstruction. All plates fit in slots machined in the plenum walls. Table 3.2 gives the specifications of each plate in detail.

The honeycomb section in all plenums is located 34.9 mm downstream from the second perforated plate, and is 82.6 mm long and has 3.18 mm cells of hexagonal cross section. A recess machined in the walls of each plenum keeps the honeycomb in place.

The first screen in the primary and secondary flow passages is about 25.4 mm downstream from the honeycomb. This screen has a mesh of 30x30 wires/in. and a wire diameter of 0.165 mm, resulting in 35% obstruction. The second screen is 12.7 mm downstream from the first one; it has a mesh of 40x40 wires/in. and a wire diameter of 0.165 mm, resulting in a 45% obstruction. All screens are soldered to brass frames which fit in slots machined in the plenum walls.

The modular design of the flow conditioning sections allows for easy inspection, cleaning, and replacement of any component.

The settling chambers begin immediately following the downstream screens. These sections are 44.8 mm long and 97.5 mm long for the primary and the secondary plenums, respectively. On each settling chamber, a 0.79 mm diameter hole was drilled through one

Table 3.2 Specifications of the flow-conditioning perforated plates (A – upstream, B – downstream)

Plate	Hole size (mm)	Hole Array	Center to-center spacing (mm)		Percent Blockage
			vertical	horizontal	
Primary A	4.42	12x5	4.98	5.08	39
Primary B	3.68	14x6	4.27	4.23	41
Secondary A	4.45	14x5	5.18	5.13	40
Secondary B	3.66	17x6	3.66	4.24	41

side wall and tapped outside to provide a pressure tap These pressure taps are 25 4 mm downstream from the second screen, approximately A 1 59 mm diameter hole was also provided in the primary and secondary plenums for mounting thermocouples These holes were drilled through one side wall, between the two screens.

Each secondary settling chamber is followed by a converging channel of rectangular cross section which serves as a transition from the plenum flow area to the secondary exit area (Figure 3 1 and 3.3) Here, the secondary air is accelerated and then discharged into the mixing tube The channel is formed by the plenum side walls and two contoured walls The 'inner' contoured wall corresponds to the outer surface of the primary nozzle block (described in the following section) The shape of the contoured surfaces is defined by fifth-order polynomials with zero-valued first and second derivatives at the beginning and end of the contraction. The height of this contraction varies from 71 9 mm to 19 0 mm, and it has a width of 25 4 mm and a length-to-height ratio of approximately 2

Machining of the contoured walls was done at the Machine Tool Research Center of the Mechanical Engineering Department, using the laboratory's CNC machining facilities The resolution of the resulting contoured surfaces is of the order of ±0 05 mm All flow-passage surfaces were polished using 220 320 400 and 600 grain size abrasive paper and were buffed to a mirror-like surface using jeweler s rouge and wax This polishing method produced a surface finish of 0 2 μm or better

3 3.2 2 Primary nozzle

The primary air exits the settling chamber and discharges into the mixing tube through a two-dimensional contoured nozzle with an aspect ratio $W / H_{e,\,nozzle} = 2$ The nozzle used was machined from aluminum and was designed to provide an exit Mach number of 1.8 for the isentropic flow of gases with $\gamma = 1.4$.

The nozzle consists of two identical blocks bolted to the internal walls separating the primary and secondary plenums, and clamped between the plenums side walls (Figure 3.4). The blocks are mounted on opposite sides of the primary plenum center plane, and provide the desired change in flow area. Two stainless steel dowel pins inserted through each block and into holes drilled in the plenum side walls position the blocks accurately. One of the plenum side walls is split into two sections; the downstream section can be removed providing easy access to the nozzle blocks.

Each nozzle block has two contoured surfaces. The "outer" surface was described in the previous section and is part of the contraction for the adjacent secondary flow passage. The "inner" surface corresponds to the contoured wall of the nozzle. The initial part of the nozzle is straight and serves as an extension of the settling chamber. After this constant-area section the blocks provide a contraction where the flow begins to accelerate. The shape of the walls in this converging region is defined by fifth-order polynomial with zero-valued first and second derivatives at the points of maximum and minimum flow areas. The contraction has a length-to-height ratio of 2.5. These proportions provide near uniform flow and help prevent flow separation (Papamoschou 1986).

Following the contraction is the diverging region of the supersonic nozzle. This region is 16.2 mm long and its shape was derived using the two-dimensional method of characteristics. Boundary layer corrections were not incorporated in the final shape. Such corrections are dependent on the flow Reynolds number, and the nozzles were intended for

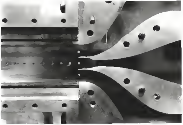

Figure 3.4 Primary nozzle blocks

use at a range of Reynolds numbers. The intersection of the surfaces of converging and diverging regions provides a near sharp edge at the nozzle throat.

The design throat and exit heights for this nozzle are $H_{t,\ nozzle} = 8.83$ mm and $H_{e,\ nozzle} = 12.70$ mm respectively. The actual dimensions when the nozzle is installed are $H_{t,\ nozzle} = 8.79 \pm 0.04$ mm and $H_{e,\ nozzle} = 12.65 \pm 0.04$ mm respectively. The theoretical Mach number computed from the actual dimensions is $M_1 = 1.80$ (using isentropic one-dimensional relations). The trailing edge thickness of the nozzle blocks is 0.4 mm approximately.

The nozzle's contoured surfaces were also machined at the Machine Tool Research Center with resolution of the order of ±0.05 mm. These surfaces were polished using the same method described in Section 3.3.2.1.

3.3.2.3 Mixing tube

The primary and secondary streams come into contact at the exit plane of the primary nozzle and secondary exit passages. At this point they begin to mix in a constant area mixing tube of rectangular cross section (Figure 3.1 and 3.5). The mixing tube is 25.4 mm wide and 51.6 mm high, and is formed by two side walls, a top wall and a bottom wall which bolt together providing the desired flow passage. All internal surfaces were polished using the method described in Section 3.3.2.1. Linear O-rings provide a face seal between the mating surfaces of the four walls.

The side walls were machined from aluminum, while the top and bottom walls were machined from brass. Each wall consists of a long section (323 mm) and a short section (177 mm) which are bolted together. This design provides two different mixing tube lengths

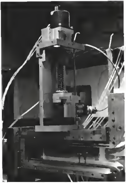

Figure 3.5 Ejector mixing tube and traversing impact-pressure probe.

although only the maximum-length configuration was used in this investigation. The mixing tube is bolted to the plenum, and it extends 500 mm beyond the exit plane ($x = 0$, Figure 3.1).

The long section of one side wall was used for static pressure measurements and has 55 holes 1.59 mm in diameter drilled along three parallel rows. This pressure plate can be installed upstream or downstream thus allowing measurements of side-wall pressure along the entire length of the mixing tube. Each hole is counterbored on the outer surface, where it is fitted with a nipple consisting of a short section of surgical stainless steel tubing. A section of plastic tubing 60 cm long with inside diameter of 0.8 mm connects each nipple to the instrumentation. Self-closing quick-connect couplings fitted at the end of the tubing provide a fast and reliable connection to the instrumentation.

Twenty-seven of the 55 pressure taps are spaced every 10 mm along the center of the wall ($y = 0$, Figure 3.1). The remaining 28 taps are off center, 14 on either side and spaced every 20 mm. The first off-center tap is at $y = 13.20$ mm, and the remaining 13 are at $y = 19.69$ mm. The first tap in each row lies at $x = 0$ when the plate is mounted upstream. These are used to measure the exit pressures of the primary and secondary. Three taps provided on a short side-wall are used to obtain these pressures in runs for which the long section is installed downstream. Figure 3.6 shows the side wall pressure plate.

The long sections of the top and bottom walls have 14 equally spaced ports machined along their center ($z = 0$, Figure 3.1). These ports provide access for the probe used for pressure traverses and the microphone used for acoustic measurements (as described in Sections 3.3.3 and 3.4.3, respectively). In both walls the ports are spaced every 20 mm, with the first one located 25.4 mm from the upstream end. A threaded brass plug fitted with an O-ring provides a leak-free seal for each port. When the plugs are installed in their

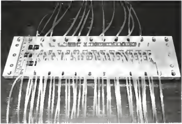

Figure 3 6 Side wall pressure plate

respective ports, their ends are within ±0.03 mm from the inside wall surface. The long and short sections of the top and bottom walls can also be installed upstream or downstream interchangeably, thus allowing for pitot traverses and acoustic measurements along the entire length of the mixing tube.

3.3.3 Traversing Impact-Pressure Probe

The traversing total-pressure impact probe fabricated for this experimental study is shown in Figure 3.5. As a result of the variable probe-interference effect observed in an earlier study (Roan et al., 1992), a probe was built which resulted in near-constant flow obstruction. This was accomplished by attaching an extension to the probe stem (i.e. a dummy stem) to maintain a constant flow area during traverses. Two brass plugs with a hole drilled in through their center serve as sleeves through which the stem and its extension slide during a traverse, and can be installed in any of the 14 port locations (Section 3.3.2.3).

The probe used was equipped with a removable sting to simplify the procedure and reduce the time required to change the axial position of the probe. This was accomplished with a special miniature coupling machined from stainless steel. The stem and its extension are soldered to the female part of the coupling, while the sting is soldered to the male part. When the probe is assembled, the coupling provides a pressure passage between the sting and the stem and secures the two perpendicular to each other. A Buna-N O-ring with a 0.79 mm inside diameter is used to seal the mating surfaces of the coupling. All the parts of the probe assembly are shown in Figure 3.7.

Two stings, 25.4 mm and 35.4 mm in length, were constructed from hard tempered stainless steel hypodermic tubing. The tubing used has outside and inside diameters of 0.812 mm and 0.508 mm, respectively. The nose of these stings has a screwdriver

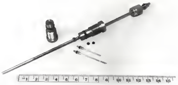

Figure 3.7 Disassembled impact pressure probe

wedge-like shape, and has a rectangular opening of 0 89 mm by 0 13 mm, approximately To obtain this geometry, a narrow strip of shim stock 0 127 mm thick was inserted about 4 mm into the end of the tube The end of the tube was then clamped together, making sure that the tube collapsed evenly with the shim stock still inserted in the center The flattened end was then shaped to a wedge using a sharpening stone, and was polished to a mirror-like surface with 600 grain size abrasive paper and 348 rouge

The stem of the probe and its extension are each about 10 cm long, and were also made from hard-tempered, stainless steel tubing having outside and inside diameters of 2.41 mm and 1 60 mm respectively A Swagelok coupling was used to connect the open end of the stem directly to a pressure transducer

The probe is moved across the mixing tube (y direction in Figure 3 1) with a computer-controlled motorized leadscrew The leadscrew assembly is mounted on top of the long brass wall of the mixing tube The assembly slides in a rail machined in this wall and can be locked at any desired position The leadscrew has a pitch of 10 16 mm The stepper motor that drives the leadscrew provides 200 steps per revolution, while the motor driver allows for half step motion This combination translates into a traverse resolution of 0 0254 mm The dimensions of the probe allowed for a maximum displacement of 46 99 mm, which represents 91% of the mixing tube height. The motor was operated at near full capacity, resulting in a traverse time of approximately two seconds The time response of the pitot-pressure transducer is 1 ms. Further numerous experiments confirmed that the effective time response of transducer/probe assembly Is sufficiently small to insure correct pressure readings for the traverse speed used

By using both stings and the 14 ports available traverses can be made between $x = 0$ and $x = 26$ cm when the long walls are installed upstream, and between $x = 17\ 6$ cm and $x = 43\ 6$ cm with the walls installed downstream (with $\Delta x = 1$ cm in either case) The pressure transducer used in conjunction with the probe is mounted on a bracket bolted to the traversing nut of the leadscrew Further details regarding the transducer and the pressure traverse procedure can be found in Sections 3 4.2 3 and 3 5 2, respectively

3.3.4 Schlieren Visualization System

Visualization of the mean flow field in the mixing tube was obtained using a continuous-light source Schlieren optical system This method was implemented to help characterize the flow structure, particularly near the supersonic primary core and the surrounding mixing layers, and to provide a qualitative check of the flow measurements A schematic of this system is shown in Figure 3 8

The light source in this system is a 150 watt Xenon arc lamp (Osram XBO150) mounted in a fan-cooled housing (Oriel C-60-30) and powered by a Universal Lamp Power Supply and Ignitor (Oriel C-20) The light from the lamp is focused by a condensing lens built into the lamp housing. A knife edge placed at the focal plane of the lens blocks part of the focused light beam. The light not blocked by the knife edge is then reflected towards the mixing tube by a parabolic mirror 400 mm in diameter and having a focal length of 2 5 m approximately

The parallel light beam enters and leaves the mixing tube through glass windows mounted in custom-built aluminum side walls. The windows are made of precision BK7-P crown glass, and have a surface flatness of 6 wavelengths over the full length (305 mm) and parallelism within 16 arc seconds Each side wall consists of a retaining frame and a

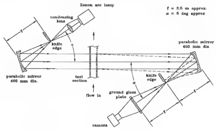

Figure 3.8 Schematic of the Schlieren System

mounting plate which hold the glass in place when bolted together A two-part urethane rubber (Devcon, Flexane 80m Liquid) was injected in the gap between the glass and the retaining frame to seal the assembly and provide a smooth metal-to-glass transition on the surface adjacent to the flow Sheet gasket material was used to provide a face seal along the perimeter of the window, between the glass and the bolting plate When mounted, the window assemblies provide a rectangular viewing area of 293 mm by 38 1 mm which allows observation of the flow field beginning roughly at the throat of the nozzle

After passing through the test section, the light beam is reflected by another parabolic mirror (identical to the one mentioned above) A second knife edge is placed at the focal point of the second mirror, opposite to the image of the first knife edge, effectively forming a slit of the order of 2 mm. A ground glass plate serves as projection screen for the resulting Schlieren image This plate is positioned two focal distances from the second mirror, producing an image of the mixing-tube viewing area of approximately the same dimensions. A 120 mm camera was used to obtain photographs of the Schlieren image, and a VHS video recorder was used to obtain a motion picture of the flow field image

All the components of the Schlieren system were installed roughly at the same height as the mixing tube to keep the light beam near the $y = 0$ plane of the mixing tube (see Figure 3 1) Photographs were taken with the knife edges oriented parallel and perpendicular to the flow direction The included angle of beam reflection on the mirrors was approximately five degrees Using small reflection angles helps minimize the optical aberrations introduced by the mirrors

3.3.5 Vacuum Exhaust System

The test-section pressure required for the investigation was obtained with a vacuum exhaust system. This system consists of a transition diffuser, a back-pressure control valve, the exhaust line, four vacuum-storage tanks, and a high-capacity vacuum pump. A schematic of this system is shown in Figure 3.9.

The transition diffuser is located immediately downstream from the mixing tube. The diffuser is 760 mm long, and it has a rectangular inlet 50.8 mm high by 25.4 mm wide and a circular exit 102.3 mm in diameter. The body of the diffuser is made of 4.76 mm thick, 304 stainless steel sheet, and consists of two identical sections bent to the desired shape using about 20 bends and welded together. The resulting geometry has a 4.82° average included divergence angle and an exit-to-inlet area ratio of 6.4. Stainless steel flanges are welded at each end of the body and connect the diffuser to the mixing tube and the exhaust line.

The flow is then exhausted from the test section and into vacuum-storage tanks through a 4 in. diameter PVC pipe. A 4 in. vacuum butterfly valve is mounted in this pipe downstream from the diffuser, and is used to control the test-section pressure. This valve was originally mounted immediately after the diffuser. However, early tests showed that in this proximity the valve induces flow separation inside the diffuser, forcing the flow inside the mixing tube to be skewed. As a result, the valve was moved farther downstream, roughly 30 pipe diameters from the diffuser exit. The flow field in the mixing tube was significantly more centered with the valve in this new position.

The PVC pipe leads to four cylindrical tanks manifolded together, identical to those used in the high pressure air supply. These tanks are evacuated before and during runs with a 165 cfm (0.078 m^3/s) Kynney vacuum pump. The pump is capable of blank-off pressures

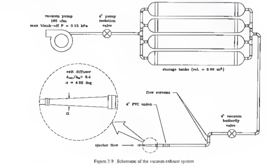

Figure 3.9 Schematic of the vacuum exhaust system

of 0 13 kPa with the gas ballast fully opened. Although every effort was made to seal the test section and the exhaust system completely, a totally leak-free system of this scale is nearly unattainable. The leaks that remained, however, were considered negligible for the purpose of this study. Because some leaks persisted, the lowest tank pressure prior to a run was between 2 4 kPa and 3 4 kPa, approximately. This pressure was sufficiently low to keep the butterfly valve choked at all times and, hence, maintain the test section pressure nearly constant. The vacuum level was monitored before and during runs in the same fashion as the air supply pressure to insure consistency between runs.

3.4 Instrumentation

Different types of instrumentation and measurement methods were used to gather the necessary data. Among the parameters of interest are total, static and impact pitot pressures, total temperatures, and sound pressure levels and acoustic spectra. The details regarding each type of measurement are provided in the following sections, and a summary of the instruments used and their specifications is provided in Appendix A.

With the exception of side-wall pressure measurements and the atmospheric pressure obtained with a mercury manometer and a barometer, respectively, most measurements were obtained electronically using a 12 MHz AT type personal computer (PC). This was done by collecting the analog signal from the various measurement devices with two 16-channel multiplexers (Acces AIM-16(P)). The output signal from each pressure transducer was transmitted to the multiplexer using shielded twisted-pair wires. The thermocouple extension wires were shielded using steel braid shielding and were assigned to multiplexer channels that have an electronic ice-point compensation

The multiplexers were connected to a moderate speed, analog and digital (A/D) computer board having 12-bit data resolution (Acces AD12-8). Digital output from the A/D board was also used to control two electronic relays which energize the flow shutoff solenoid valve and the solenoid valve used for venting the air supply tanks. The run control and data acquisition program was written in Quick Basic 4.5 (Section 3.5.6), resulting in a maximum A/D throughput of 9000 single-channel samples per second. The multiplexers and the A/D board were calibrated prior to the experiments using a precision voltage source, and were checked periodically for proper operation along with the rest of the instrumentation.

3.4.1 Total Temperature Measurements

The total temperature of the primary, $T_{0,1}$, and secondary, $T_{0,2}$, were approximated by measuring the air temperature with thermocouples mounted in the plenums, as described in Section 3.3.2.1. Two Omega type T (copper-constantan) thermocouples with an exposed junction and having a sheath diameter of 1.59 mm were mounted in the plenums, one was mounted in the primary plenum and one in the top secondary plenum. The thermocouples were installed ensuring their junctions protruded into the plenums 3 mm to 4 mm, approximately. Because the Mach number in all plenums is approximately 0.086 for all cases considered, the total temperatures are underestimated by less than 0.2%.

3.4.2 Pressure Measurements

Pressure measurements were obtained using several transducers and a 30-column mercury manometer. The total pressures for the primary and secondary, impact pitot pressure, air supply pressure, and orifice plate static pressures were all measured with transducers. Side-wall static pressures were measured with transducers and also with the mercury manometer. The output of all transducers was checked after a warm-up period, prior to a series of tests, to measure their zero shift. The zero shift was then used by the data acquisition code to correct the measurements.

3.4.2.1 Total pressure

The total pressure of the primary ($P_{0,1}$) and each secondary ($P_{0,2a}$ and $P_{0,2b}$) were approximated by measuring the wall static pressures inside the respective plenums. These pressures were measured with transducers connected to side-wall pressure taps described in Section 3.3.2.1. The primary planum pressure was measured with a 413 kPa gage pressure transducer (Omega PX181G-5V). The secondary plenum pressures were measured with two 207 kPa differential pressure transducers (Micro Switch 140PC). The low-pressure side of the differential transducers was connected to the plenums and the high-pressure side was left open to the atmosphere.

Absolute pressures were determined from these measurements and the atmospheric pressure reading. Because the flow velocities inside the plenums are low ($M = 0.08$), the use of static pressure as an approximation to total pressure resulted in errors smaller than ~ 0.5%.

3.4.2.2 Static pressures

Static pressures were measured at different locations throughout the rig using side wall pressure taps. These included (1) the pressures across the total-flow and secondary flow orifice plates, (2) the primary and secondary exit static pressures, and (3) the side-wall pressures along the mixing tube.

The upstream pressure and the pressure drop across each flow orifice (P_{o1} and $\Delta P_o = P_{o1} - P_{o2}$) were measured using two transducers. A 2070 kPa gage transducer (Omega PX241-5V) and a 69 0 kPa differential transducer (Valydine DB15, connected to a Valydine CD15 carrier demodulator) were used with the total-flow orifice for P_{o1} and ΔP_o, respectively The reading from the first transducer also corresponds to the air supply pressure. For the secondary flow orifice differential transducers (Valydine DB15 connected to Valydine CD15 carrier demodulators) with ranges of 103 kPa and 69 0 kPa were used for P_{s1} and ΔP_s, respectively Here, the upstream pressure transducer was connected to give the difference between ambient and line pressures

The primary and both secondary exit pressures ($P_{s,1}$, $P_{s,2a}$ and $P_{s,2b}$) were measured with differential pressure transducers having a range of 69 0 kPa (Micro Switch 140PC) These transducers were connected to measure the difference between ambient pressure and the test-section static pressure The same type of transducers and installation was used to measure static pressures at all axial locations where pitot traverses were made In doing this three transducers were connected at the same streamwise position of the probe one on each row of side-wall pressure taps (Section 3 3 2 3)

Side wall static pressures were also measured using a 30-column mercury manometer (Meriam Instrument Co., model 33M1335) The manometer has three banks of ten columns; each bank has a separate mercury reservoir. A 2-m section of plastic tubing with an inside diameter of 0 8 mm was connected to each column Couplings like those described in Section 3 3.2.3 connect these plastic tubes with those on the mixing tube side wall

3.4.2.3 Impact pitot pressure

Impact pitot pressure (P_{pit}) was measured using a differential pressure transducer with a range of 414 kPa (Valydine DB15 connected to Valydine CD12 carrier demodulator). This transducer was connected to measure the difference between pitot pressure and the side-wall pressure at y = +19.69 mm, at the streamwise position of the probe (i.e. the transducer measurement corresponds to $\Delta P = P_{pit}(x,y) - P_s(x,y = +19.69 \text{ mm})$). The static pressure $P_s(x,y = +19.69 \text{ mm})$ was independently measured with a transducer as explained in 3.4.2.2 and was used to determine P_{pit}.

3.4.3 Microphone for Acoustic Measurements

Sound pressure measurements of the flow acoustic emissions were obtained using a Kulite temperature-compensated, high-intensity miniature microphone (model MIC-062-LT). The sensing element of the microphone consists of a four-arm Wheatstone Bridge mounted on a silicon diaphragm 1.57 mm in diameter. This element is housed in a cylindrical case 31.75 mm long and 1.63 mm in diameter. The microphone has a dynamic range of 100 to 190 db and nearly flat response to 50 kHz, and can be used in pressures of up to 172 kPa. The transducer has a sensitivity of −129.12 db at 1 μbar and a reference voltage of 1V (i.e. 3.50 μV/Pa), when the supply voltage is 15.00 VDC. The output is compensated over the temperature range of −55°C and 120°C, and has a thermal sensitivity of ±0.5 db/100°F. The dynamic range, small size and rugged construction of this transducer are ideal for measurements and installation purposes.

A brass plug like the ones described in Section 3.3.2.2 was specially adapted for mounting the microphone (Figure 3.10(a)). The cap and body of this plug can be separated

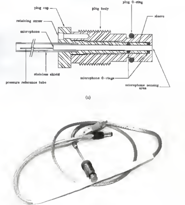

(a)

(b)

Figure 3 10 Microphone used for sound measurements
(a) microphone installation in brass plug (b) complete microphone assembly

for installation or removal of the microphone. A 1.7 mm diameter hole is drilled through the center of the plug assembly and is used for mounting the microphone. Two O-rings separated by a brass sleeve are slipped over the end of the microphone and provide a tight seal when the cap and body of the plug are fastened together. The end of a 2.5 in. section of stainless-steel tube is braced to the cap in a counterbore machined at the mounting hole opening. This tube serves as a rigid shield which protects the microphone's pressure reference tube from bending and possible clogging or damage. A small orifice drilled on the side ensures that the reference tube is at atmospheric pressure.

The No. 38 AWG input and output leads of the microphone and the temperature compensation module were encased in PVC flexible tubing for protection. The flexible tubing was in turn passed through a steel cable shield which prevented contamination of the signal and provided additional protection for the wiring. Gold plated connectors were soldered to the signal leads to ensure maximum signal transfer. Figure 3.10(b) shows the complete microphone installation.

A custom built DC power supply was used to provide the required input to the transducer. This unit derived power from four rechargeable, 9V lithium batteries, and included two filtering capacitors and a voltage regulator. The output of this power supply is 15.19 VDC resulting in an effective microphone sensitivity of 3.55 μV/Pa. A schematic of the power supply is shown in Figure 3.11.

The output of the microphone was fed to a pre-amplifier (Stanford Research Systems Model SR 520). The signal was AC coupled using the amplifier's 0.03 Hz high-pass filter and the 1 MHz low-pass filter (DC to 1 MHz). The signal was amplified using gains of 20 and 50 for most of the measurements made.

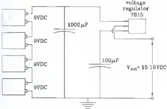

Figure 3 11 Schematic of DC power supply for microphone.

A two-channel, Tektronix Fourier Signal Analyzer (Tektronix 2642) was then used to obtain the autospectrum and acoustic sound pressure level (SPL) from the signal. The analyzer has an input amplifier with maximum full-scale settings ranging from ±14 mV to ±10 V, and an A/D converter with 12 bits of precision. The analyzer has several input-frequency bandwidths ranging from DC to 200 MHz, a maximum frame size of 4096 data samples, and a maximum of 1600 spectral lines (i.e. sampling factor of 2.56). The signal was AC coupled in all tests using bandwidths of 10, 20, 50 and 100 kHz, and 1600 spectral lines, the resulting bandwidth resolutions are 6.25, 12.50, 31.25 and 62.50 Hz, respectively. The frequency accuracy specified by the manufacturer is ±0.01%.

3.5 Test Procedure and Run Sequence

The test procedures used were adopted after evaluating the behavior and fine tunning the response of the rig. Many of these procedures were changed during the initial stages of the experiments and, in some cases, modifications were made to the rig and/or the instrumentation to ensure satisfactory performance of the apparatus. Below is a description of the experimental procedures that were critical to the experiments. The test-run and data-acquisition sequence is also outlined.

3.5.1 Adjustment of Flow Conditions and General Test Procedures

Among the most essential steps of the experiments was to establish the desired flow conditions for a given test run. In this discussion, the flow conditions are the total and exit pressures of the primary and secondary streams. The primary flow was adjusted first because the pressure ratio of the supersonic nozzle is fixed and, hence, the total and exit pressures are nearly independent of the back pressure (i.e. mixing-tube pressure). The primary flow valves were opened until the primary exit pressure reached the desired level Once the primary flow was set, the secondary flow valves and the back-pressure valve were adjusted simultaneously until the desired pressures settings were reached This required many trials as the secondary flow and test-section pressure are not independent (for the secondary flow is subsonic and unchoked). To obtain consistent results, the same start-up air supply and vacuum pressures were used during flow adjustment and during data collection.

For Schlieren runs, the flow conditions were first adjusted with the side-wall pressure plate in place of one of the two windows, as the glass windows do not allow measurement of the exit pressures Once the flow rates were adjusted, the second window was installed and only the test-section back pressure was adjusted (if necessary) by opening or closing the 4 in butterfly valve.

After the flow conditions were set, the test run was made and data were collected. A preselected settling time was allowed once the air flow started before taking any measurements In most instances, a 2-second settling time was sufficient to allow the flow field and the instruments to reach near steady state conditions (results presented in Chapter 4, Section 4.6 1, justify using short settling times) In runs made for manometer readings this time was increased to 6 seconds The time required for actual data acquisition was roughly between two and three seconds, depending on the type of measurement The vacuum pump allowed for pump-down times between runs of one to four minutes, depending on the test case and the type of measurement that was made.

Separate test series (i e sets of test runs) were made to obtain pitot-pressure traverses, side wall static-pressure measurements, Schlieren visualization, and acoustic measurements Some runs were made for data validation and included pitot pressure traverses and one of the other three types of measurements. A combined total of 706 test runs were made to obtain the desired database.

The flow conditions were always recorded at the beginning and at the end of each run by taking an average of ten samples for each pressure transducer and thermocouple reading. With the exception of Schlieren runs, a test was considered successful if the exit pressures at the beginning of the run were within ±0.34 kPa (i.e. 1% or less) of the desired values. Stagnation pressures were used to check the flow conditions in Schlieren runs.

3.5.2 Pressure Traverse Runs

In a typical traverse an impact pressure reading was taken at the starting position of the probe ($y = +23.495$ mm), and after each incremental motion ($\Delta y = 0.0254$ mm) through the 46.99 mm traverse (i.e. 1851 pressure readings). The electronic step counter in the motor controller is read by the computer and provides a record of the probe position corresponding to each pressure reading. Traverses were obtained at a number of streamwise positions between the inlet and exit planes of the mixing tube. Tables B.1 and B.2 in Appendix B show the positions where traverses were made for each test case. A total of 282 test runs were required to complete these measurements, not including those made to obtain the redundant measurements. To minimize time consuming hardware changes, all the traverses needed at a given streamwise position were obtained prior to moving the probe to a different port (with a few exceptions which are discussed in Chapter 4, Section 4.3.3). After each run the data was visually checked by plotting it on the computer screen.

Several traverses were repeated for validation, including those at $x = 0$ and $x = 43.62$ cm (inlet and exit planes) for all test cases. For test cases with relatively high primary flow rates (8–11), a few probe positions resulted in choking of the flow inside the mixing tube. When this happened, the lowest attainable secondary exit pressure was higher than the desired exit pressure ($P_{s,2} \geq 34.5$ kPa). However, a traverse was still made provided this condition was not too severe ($P_{s,2} \leq 35.3$ kPa).

3.5.3 Manometer Measurements Runs

Manometer readings were obtained from black-and-white photographs of the manometer taken after the settling period. Figure 3.12 shows a typical photograph taken during a static-pressure run. The manometer has fluorescent back lights which allow exposures of 1/500th second. Each photograph was identified by a label attached to the manometer indicating the test run and the column/pressure-tap configuration used. Because the manometer cannot accommodate all 55 pressure taps at once, the centerline taps and the off-center taps were connected to the manometer in separate runs. The connectors on the plastic tubing (Section 3.3.2.3) helped reduce the time required to make this switch, thus resulting in no significant delays between runs.

Two photographs were taken in separate runs for each test case and manometer/pressure-tap configuration to establish repeatability. It was found that measurements obtained from the two photographs were nearly always within 12.7 mm Hg (1.7 kPa) and in most cases within 5.08 mm Hg (0.68 kPa). As a result, the two readings were used to compute average side-wall pressures. This procedure was followed with the side-wall pressure plate installed in the upstream and downstream positions. The two mounting positions provide an overlap of measurements in the region between x = 18.0 cm and x = 26.6 cm. All measurements needed at one position were completed before moving the pressure plate. The side-wall pressure measurements required a total of 88 runs (i.e. eight photographs per test case).

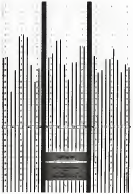

Figure 3 12 Photograph of the 30-column manometer

The first column in each bank was always connected to the top secondary exit-pressure tap, and was used as a reference for the other nine columns in the bank. This method ensured that every column in the manometer was referenced to the same pressure. The secondary pressure was chosen as reference instead of the ambient pressure because it resulted in shorter stabilization periods. Atmospheric pressure and ambient temperature readings were recorded periodically and were used with the secondary pressure to convert the manometer readings to absolute pressures (see Appendix C for details).

3.5.4 Acoustic Measurements Runs

Acoustic emissions were measured for all test cases at selected axial microphone positions (Table B.3, Appendix B). Measurements were made in the first two-thirds of the mixing tube between $x = 2.54$ cm and $x = 28.54$ cm. Preliminary tests showed that all significant flow-generated screech occurred in the first half of this region. Most measurements were obtained with the microphone installed in the top wall. A few runs were made with the microphone mounted on the lower wall for comparison of the measurements. A total of 234 runs were made for these series of tests, although only selected results are presented here in Chapter 4. Because the microphone can be moved between ports rapidly, all the runs needed for a given test case were completed before changing the flow conditions.

For most microphone positions the autospectrum of the acoustic emissions was obtained using additive averaging of 10 frames and sampling bandwidths of 0 – 20 kHz, 0 – 50 kHz and 0 – 100 kHz (i.e. three runs for each position). Doubling the number of frames resulted in no significant gains in repeatability. Collecting the additional data, however, increased the run time and the amount of air used, thus making more evident the transient effects inherent to blowdown experiments Data was collected using the smallest possible input gain to minimize analog-to-digital quantization errors

3.5.5 Mixed Measurements Runs

A number of runs were made to investigate whether the probe has a significant effect on the character of the flow field and hence, on the other parameters that were measured. These validation experiments were limited to two or three test cases. In these runs, side-wall static pressures or acoustic emissions were measured with the probe installed in the mixing tube.

Static-pressure measurements were repeated for test cases 1, 5 and 9, with the probe installed at x = 12 cm and x = 26 cm For these measurements, only the upstream pressure-plate position ($0 \le x \le 26$ cm) was considered and three photographs were used to compute average pressures For the acoustic measurements the probe was mounted at x = 12 cm and x = 26 cm, and data was collected for input bandwidths of 20 kHz 50 kHz and 100 kHz for the same test cases A total of 72 static pressure runs and 30 acoustic measurement runs were required for these sets of tests. Schlieren photographs were also obtained for the test cases 1 (*baseline* case) and 5 with the probe installed at x = 7 cm

3.5.6 Run-Control Code

Control of the test runs and data acquisition was accomplished with a computer code written in Quick Basic 4.5 specially tailored to this investigation to ensure proper data acquisition and data validity In addition several safety checks are implemented by the code to reduce the possibility of damage to the rig as a result of equipment malfunction or operator error Following is a brief outline of the test-run sequence

Run-control and data-acquisition code

1 The test-case flow conditions (i.e. test case number and $P_{s,1}$ and $P_{s,2}$ or $P_{0,1}$ and $P_{0,2}$), the type of run desired (traverse, side-wall pressures, acoustic or Schlieren), and the instrument positions (streamwise position for the probe or microphone, etc.) are read from a pre-established data file. Output data files are opened as necessary.

2a. For pitot pressure traverses the motor controller is initialized for the desired traverse motion and the probe is positioned for a traverse.

2b For acoustic measurement runs the Fourier analyzer is initialized for transient data capture (input amplifier gain, bandwidth, and number of frames).

3 The operator is prompted to check for proper instrument settings, hardware configuration, etc., as required for the given test run.

4 Operator enters (a) current ambient temperature and pressure, (b) tolerance bounds for test-run flow conditions, and (c) settling time and minimum vacuum level at the start of the flow. Checking for vacuum level served as a safety feature to prevent accidental overpressurization of the system (e.g. closed back-pressure valve, etc.)

5 The A/D board is initialized and the instrumentation is assigned to the corresponding multiplexer channels.

6 The apparatus is ready for a run and the operator is prompted to initiate the run from the keyboard. Here, the operator can monitor the air supply pressure and vent the air tanks to adjust the start-up pressure before the run. The

operator can also reenter any of the parameters in (4) or abort the run at this point

7 The solenoid valve is opened to start the air flow provided the vacuum pressure is equal or below the input value

8 After the required settling time ten samples are read for each transducer and thermocouple at a rate of 1864 samples per second. All signals are converted to temperatures and pressures using the corresponding instrument calibrations, and the average and standard deviation of each measurement are computed At this point the readings are checked for (a) system overpressurization and (b) incorrect flow conditions If either condition exists the test run is aborted and the operator is provided with a report on the condition

9a. For pitot pressure runs a traverse is made, taking pressure readings immediately after each change in position-counter reading (Section 3.3 3) It was found that three to eight readings could be obtained for each counter reading.

9b For acoustic-measurement runs the Fourier analyzer is triggered for transient data acquisition

9c For side-wall static pressure runs the operator is prompted to take a photograph of the mercury manometer

9d For Schlieren runs the operator is prompted to take a photograph of the projection screen

10 Ten samples are read for each transducer and thermocouple at a rate of 1864 samples per second. All signals are converted to temperatures and pressures using the corresponding instrument calibrations, and the average and standard deviation of each measurement are computed. These end-of-run averages are used with those obtained in (8) above to obtain the average measurements for the test run

11 The air-supply solenoid valve is closed

12 For traverse runs, the probe is returned to its initial position.

13 Primary and secondary flow rates and Mach numbers are computed

14 A summary of the test run flow conditions is printed to the screen

15 The data collected as well as some test run parameters and instrument settings (e g settling time initial air supply pressure, tolerance bounds for test conditions, amplifier gains, etc) are stored in the output file.

16 The test is terminated. In pitot-pressure runs, the operator is given the option of displaying the pressure profile on the screen or terminating the test

CHAPTER 4
EXPERIMENTAL RESULTS

4.1 Measured Flow Conditions

The flow conditions for the experimental test matrix are summarized in Chapter 3. Among these, the controlled test conditions were the total and exit static pressures for the primary and secondary streams. The primary nozzle was never overexpanded in these experiments and therefore, the primary pressures are related by the nozzle pressure ratio and cannot be adjusted independently. Because (1) primary underexpansion is the main the focus of this study, and (2) the extent of underexpansion is more directly given by the difference between exit pressures, the exit pressure was chosen as the controlled parameter for the primary.

Among the objectives of this investigation are to provide a detailed and precise database and to compare the ejector flow fields and performance for the eleven test cases. Therefore, maintaining the test conditions close to the desired values was a high priority throughout the experiments, particularly in pitot-pressure traverse and side-wall pressure runs as these measurements are used for quantification of the different flow fields. Ensuring consistent flow conditions was not an easy task, given that the test procedure in many instances required resetting these conditions many times for each test case. For example, for pitot-pressure runs the flow for each test case was adjusted at each probe position, as all the data needed at a given position was collected before moving the probe to a different port. Nevertheless, in this section it is shown that the flow conditions were maintained within close bounds of the nominal values In the remainder of this chapter, the fundamental measurements are presented and discussed in detail The analysis and interpretation of these results in relation to the development of the flow field and ejector performance are given in Chapter 5

4 1.1 Pitot-Pressure Traverse and Side Wall Pressure Test Series

The primary and secondary flow conditions measured for the pitot-pressure traverse and side-wall pressure test series are given in Tables 4 1 and 4.2 respectively The standard deviations are given for the pressures in terms of percentage of the corresponding average values The values listed are the test-case averages for all runs made in the test series and are based on single-run mean measurements The single-run mean pressures were computed using measurements made at the beginning and at the end of each run as explained in Section 3 5 6 The initial and final Mach numbers for each run were calculated (details in Appendix C) using the corresponding pressures and the isentropic relation

$$M = \sqrt{\left\{\left(\frac{P_0}{P_s}\right)^{\frac{\gamma-1}{\gamma}} - 1\right\}\frac{2}{\gamma-1}} \qquad (4\ 1)$$

As seen from Tables 4 1 and 4 2, in both test-series the average total and exit pressures for the primary are within 1.2% and 0 5% respectively, of the intended values (Table 3 1) The test-series average pressures for the secondary are within 1 0% and 0 8 % respectively The differences observed are comparable to the accuracy of the measurements and can be considered acceptable for the purpose of this investigation Further, the relatively small standard deviations indicate that the single-run mean flow conditions are also close to the nominal test conditions The standard deviation of the total primary pressure is no more

Table 4.1 Flow conditions for the pitot pressure traverse test series.

Test Case	$P_{0,1}$ (kPa) ± [% std. dev.]	$P_{s,1}$ (kPa) ± [% std. dev.]	M_1	$P_{0,2a}$ (kPa) ± [% std. dev.]	$P_{s,2a}$ (kPa) ± [% std. dev.]	M_{2a}	$P_{0,2b}$ (kPa) ± [% std. dev.]	$P_{s,2b}$ (kPa) ± [% std. dev.]	M_{2b}
1	199.4 [1.9]	34.5 [0.4]	1.80	37.6 [0.3]	34.6 [0.3]	0.34	37.6 [0.2]	34.4 [0.3]	0.36
2	211.9 [2.1]	36.9 [0.4]	1.80	37.6 [0.3]	34.6 [0.5]	0.34	37.6 [0.2]	34.4 [0.2]	0.36
3	226.2 [2.0]	39.2 [0.5]	1.80	37.5 [0.4]	34.6 [0.4]	0.34	37.6 [0.4]	34.4 [0.5]	0.36
4	239.9 [2.2]	41.7 [0.2]	1.80	37.6 [0.4]	34.6 [0.4]	0.34	37.6 [0.4]	34.4 [0.4]	0.36
5	253.5 [1.7]	44.1 [0.3]	1.80	37.6 [0.4]	34.6 [0.5]	0.34	37.6 [0.4]	34.4 [0.4]	0.36
6	267.2 [2.1]	46.5 [0.2]	1.80	37.6 [0.3]	34.6 [0.4]	0.34	37.5 [0.3]	34.3 [0.3]	0.36
7	280.2 [1.7]	48.8 [0.3]	1.80	37.6 [0.3]	34.7 [0.4]	0.34	37.6 [0.3]	34.3 [0.3]	0.36
8	294.6 [2.2]	51.2 [0.3]	1.80	37.6 [0.6]	34.8 [0.7]	0.34	37.6 [0.5]	34.4 [0.6]	0.36
9	307.5 [1.8]	53.6 [0.4]	1.80	37.7 [0.5]	34.7 [0.7]	0.34	37.6 [0.5]	34.4 [0.6]	0.36
10	321.3 [2.0]	56.0 [0.3]	1.80	37.6 [0.5]	34.7 [0.8]	0.34	37.6 [0.5]	34.4 [0.6]	0.36
11	333.8 [1.4]	58.4 [0.3]	1.80	37.7 [0.6]	34.8 [0.8]	0.34	37.7 [0.6]	34.5 [0.7]	0.36

Table 4.2 Flow conditions for side wall pressure test series.

Test Case	$P_{0,1}$ (kPa) ± [% std. dev.]	$P_{s,1}$ (kPa) ± [% std. dev.]	M_1	$P_{0,2a}$ (kPa) ± [% std. dev.]	$P_{s,2a}$ (kPa) ± [% std. dev.]	M_{2a}	$P_{0,2b}$ (kPa) ± [% std. dev.]	$P_{s,2b}$ (kPa) ± [% std. dev.]	M_{2b}
1	197.4 [2.0]	34.6 [0.1]	1.80	37.8 [0.4]	34.6 [0.4]	0.35	37.8 [0.4]	34.6 [0.3]	0.36
2	210.7 [2.2]	37.0 [0.2]	1.79	37.8 [0.3]	34.7 [0.2]	0.35	37.8 [0.2]	34.6 [0.2]	0.36
3	223.8 [2.3]	39.3 [0.2]	1.79	37.8 [0.3]	34.6 [0.3]	0.35	37.7 [0.3]	34.5 [0.3]	0.36
4	237.5 [2.6]	41.7 [0.2]	1.79	37.8 [0.3]	34.7 [0.3]	0.36	37.8 [0.3]	34.5 [0.3]	0.36
5	251.0 [2.5]	44.1 [0.2]	1.79	37.9 [0.3]	34.7 [0.3]	0.36	37.8 [0.4]	34.6 [0.4]	0.36
6	263.9 [2.7]	46.4 [0.1]	1.79	37.9 [0.2]	34.8 [0.2]	0.35	37.8 [0.1]	34.7 [0.3]	0.36
7	277.7 [2.6]	48.8 [0.3]	1.79	37.8 [0.2]	34.6 [0.4]	0.36	37.7 [0.2]	34.5 [0.2]	0.36
8	292.7 [3.0]	51.4 [0.2]	1.79	37.9 [0.3]	34.7 [0.4]	0.36	37.8 [0.3]	34.7 [0.4]	0.36
9	305.5 [3.1]	53.6 [0.2]	1.80	37.8 [0.2]	34.7 [0.2]	0.36	37.7 [0.4]	34.6 [0.4]	0.36
10	319.4 [2.9]	56.0 [0.1]	1.80	37.7 [0.1]	34.5 [0.2]	0.36	37.6 [0.1]	34.4 [0.2]	0.36
11	333.8 [2.9]	58.4 [0.1]	1.80	37.8 [0.5]	34.6 [0.5]	0.35	37.7 [0.6]	34.5 [0.6]	0.35

than 3.1% of the test-series average. The standard deviations of the remaining pressures are all less 0.75% of the corresponding averages. These results show that the experimental flow conditions follow the intended test plan closely.

Similarly in both test series the Mach numbers are maintained within 0.4% and 3.4% of the intended values for the primary and secondary, respectively. The secondary Mach numbers deviate slightly more from the nominal value ($M_2 = 0.35$). This can be attributed to two factors. First, the secondary pressures were roughly about 1/6 of the full range of the bidirectional differential transducers used. As a result, the accuracy of instrument readings was more critical for these measurements (see Appendix C.1). Secondly, Mach number varies rapidly at pressure ratios near unity ($P_{0,2} / P_{e,2} = 1.088$ for $M_2 = 0.35$) and any fluctuation in the secondary pressure readings are reflected in the Mach number accordingly (see Equation 3.1).

More important than the precision of the value of the "average" flow conditions are the magnitudes of variation of the flow conditions during each test run. Inspection of the data shows that the total and exit pressures for the primary dropped during runs by an average of less than 0.7%. The average pressure change for the secondary was less than 0.3% and 1.4% for the pitot-pressure traverse and side-wall pressure test series, respectively. This confirms that the pressurized air supply was sufficient to provide the necessary flow rates at near constant pressures, and that a steady state assumption is well justified in all test cases.

4.1.2 Acoustic Measurements and Schlieren Test Series

The flow conditions for the acoustic measurements and Schlieren test series are given in Tables 4.3 and 4.4, respectively. Mach numbers are not given for the Schlieren tests as

Table 4.3 Flow conditions for the acoustic measurements test series

Test Case	$P_{0,1}$ (kPa) ± [% std. dev.]	$P_{s,1}$ (kPa) ± [% std. dev.]	M_1	$P_{0,2a}$ (kPa) ± [% std. dev.]	$P_{s,2a}$ (kPa) ± [% std. dev.]	M_{2a}	$P_{0,2b}$ (kPa) ± [% std. dev.]	$P_{s,2b}$ (kPa) ± [% std. dev.]	M_{2b}
1	194.8 [0.2]	34.6 [0.2]	1.79	37.8 [0.3]	34.8 [0.3]	0.35	37.7 [0.3]	34.5 [0.3]	0.36
2	204.7 [0.3]	36.9 [0.1]	1.78	37.9 [0.3]	34.8 [0.3]	0.35	37.8 [0.3]	34.5 [0.3]	0.36
3	221.0 [0.2]	39.0 [0.3]	1.79	37.7 [0.3]	34.7 [0.1]	0.34	37.7 [0.2]	34.6 [0.2]	0.35
4	231.2 [0.3]	41.6 [0.1]	1.88	37.9 [0.1]	34.7 [0.2]	0.35	37.8 [0.1]	34.6 [0.2]	0.36
5	248.8 [0.1]	44.0 [0.2]	1.79	37.8 [0.3]	34.6 [0.3]	0.36	37.7 [0.2]	34.5 [0.3]	0.36
6	259.8 [0.1]	46.4 [0.2]	1.78	37.8 [0.1]	34.7 [0.1]	0.35	37.7 [0.2]	34.5 [0.1]	0.36
7	275.0 [0.1]	48.8 [0.1]	1.79	37.6 [0.1]	34.5 [0.1]	0.35	37.5 [0.1]	34.4 [0.2]	0.36
8	287.7 [0.2]	51.3 [0.2]	1.78	37.7 [0.2]	34.6 [0.3]	0.35	37.7 [0.2]	34.4 [0.2]	0.36
9	302.8 [0.3]	53.4 [0.2]	1.79	37.7 [0.2]	34.6 [0.4]	0.35	37.5 [0.3]	34.4 [0.2]	0.36
10	314.3 [0.2]	55.9 [0.2]	1.79	37.7 [0.1]	34.7 [0.3]	0.35	37.7 [0.1]	34.4 [0.1]	0.36
11	328.7 [0.1]	58.3 [0.2]	1.79	37.6 [0.2]	34.5 [0.2]	0.35	37.5 [0.1]	34.3 [0.2]	0.36

Table 4.3 Flow conditions for the Schlieren test series.

Test Case	$P_{0,1}$ (kPa) ± [% std. dev.]	$P_{0,2a}$ (kPa) ± [% std. dev.]	$P_{0,2b}$ (kPa) ± [% std. dev.]
1	190.2 [0.9]	37.7 [0.1]	37.6 [0.1]
2	203.7 [0.0]	37.5 [0.1]	37.7 [0.1]
3	217.0 [0.1]	37.6 [0.2]	37.7 [0.1]
4	230.0 [0.1]	37.6 [0.2]	37.7 [0.1]
5	244.1 [0.1]	37.5 [0.3]	37.5 [0.2]
6	255.5 [0.2]	37.6 [0.3]	37.6 [0.2]
7	269.7 [0.2]	37.7 [0.1]	37.7 [0.1]
8	283.1 [0.1]	37.7 [0.2]	37.7 [0.2]
9	296.1 [0.1]	37.7 [0.2]	37.6 [0.2]
10	308.9 [0.1]	37.2 [0.2]	37.2 [0.2]
11	322.4 [0.1]	37.7 [0.1]	37.7 [0.1]

exit pressure measurements are not available for these runs. Table 4.3 shows that the experimental test conditions for the acoustic-measurements test series are within limits comparable to those for the pitot-pressure and side-wall pressure runs. For the primary, the total pressure is always within 1.6% – 3.4% of the nominal setting, and the exit pressure differs by less than 0.7% from the nominal value. All secondary pressures are within 1.2% of the nominal values. The primary Mach number is within 1.3% of the nominal $M_1 = 1.8$ and the secondary Mach numbers are within 3.9% of the desired $M_2 = 0.35$.

In the case of the Schlieren runs, it was not always possible to duplicate the nominal flow conditions as precisely as it was done for the other test series. As explained in Section 3.5.1, for these runs the test conditions were adjusted with the pressure plate mounted in lieu of one of the glass windows to allow measurement of the exit static pressures. Upon replacing the pressure plate with the second window, it was always necessary to adjust further the test-section pressure with the back-pressure butterfly valve (Section 3.3.5). In addition, the total primary pressure was always between 3.6% and 4.3% lower than the nominal values when both glass windows were installed, despite the fact that the primary flow was unchanged. The average total pressures for the secondary were within 0.9% of the desired values.

The surfaces of the aluminum side-walls and the glass windows are different and must result in different skin-friction losses. The cross section of the mixing tube can also vary slightly when the side-walls are changed, affecting the local flow speed and pressure accordingly. These surface effects can lead to small differences in the pressure fields within the mixing tube. Because the windows also serve as the side walls along the expansion region of the nozzle, the different surfaces can affect the flow in the primary nozzle as well

Nevertheless, the flow conditions are considered sufficiently close to the nominal settings specially since flow visualization was used primarily as a qualitative tool.

4.2 Schlieren Visualization

Schlieren visualization of the flow field was implemented for each test case with the knife edges oriented at 0° and 90° to the flow direction. The photographs obtained provide an unambiguous image of the mean flow field. Figures 4.1 through 4.6 show the Schlieren photographs for the odd-numbered test cases. For comparison, the reader is referred to Shapiro, 1953 (pg. 143).

Although the Schlieren images are used primarily as a qualitative tool, they also provide specific information about local flow conditions which helps to establish the validity of the other measurements. The results of the visualization experiments are discussed next.

4.2.1 Ideally Expanded Test Case

The photographs corresponding to the *baseline* test case (ideally expanded primary) are shown in Figure 4.1. The images clearly show the primary core surrounded by two shear layers which merge downstream in the mixing tube. The shear layers are shown best in the 0° knife edge position, where the layer on the negative side of the flow field (i.e. $y \leq 0$, Figure 3.1) appears dark in the photographs. The layers seem to grow at rate which is approximately constant, as is typical of plane, constant-pressure shear flows.

Ideally, in a well-designed correctly-expanded nozzle, all waves are completely canceled in the expansion section and the exit flow is uniform. In Figure 4.1, however, waves of finite strength are clearly visible inside the nozzle and also within the supersonic core. This result is not surprising and can be explained as follows.

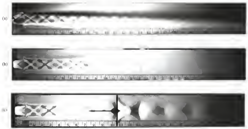

Figure 4.1 Schlieren photographs for test case 1
(a) knife edges parallel to the main flow direction
(b) knife edges perpendicular to the main flow direction
(c) knife edges perpendicular to the main flow direction and probe installed

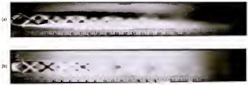

Figure 4 2 Schlieren photographs for test case 3
(a) knife edges parallel to the main flow direction
(b) knife edges perpendicular to the main flow direction

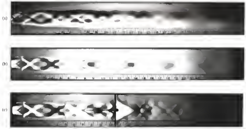

Figure 4 3 Schlieren photographs for test case 5
(a) knife edges parallel to the main flow direction
(b) knife edges perpendicular to the main flow direction
(c) knife edges perpendicular to the main flow direction and probe installed

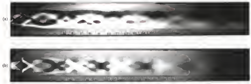

Figure 4 4 Schlieren photographs for test case 7
(a) knife edges parallel to the main flow direction
(b) knife edges perpendicular to the main flow direction

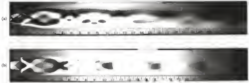

Figure 4.5 Schlieren photographs for test case 9
(a) knife edges parallel to the main flow direction
(b) knife edges perpendicular to the main flow direction

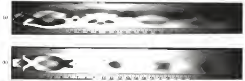

Figure 4.6 Schlieren photographs for test case 11
(a) knife edges parallel to the main flow direction
(b) knife edges perpendicular to the main flow direction

incomplete cancellation of waves can be the result of (a) small inaccuracies in the shape of the diverging section of the nozzle and/or (b) boundary layer effects The actual dimensions of the nozzle depend not only on the accuracy of the nozzle blocks (Section 3 3 2.2) but also on how accurately these fit in the plenum assembly to form the flow passage Also, the shape of the diverging section was determined assuming the nozzle has a sharp-corner throat Because of the relatively small scale of the nozzle, even small errors in either the wall contour or the shape of the throat are likely to affect the flow Boundary layers effectively change the flow area and the shape of the expansion section, and can lead to similar effects Nonetheless it will be shown in Section 4 4 that the waves observed in the *baseline* test are very weak and result only in small property changes across the flow Therefore, these waves are not expected to affect the flow significantly

Based on nozzle-design considerations and side-wall pressure measurements presented later it is possible to infer that the waves in Figure 4 1 originate at the throat as expansion waves and are reflected at the trailing edge of the nozzle as compression waves Outside the nozzle these residual waves experience multiple reflections from the shear layer forming a very regular pattern of diamond-shaped cells which extends several nozzle exit heights along the supersonic core Early in the flow the waves are narrow and appear very sharp With increasing distance and number of reflections, the waves begin to dissipate; they appear wider and their boundaries are less defined The loss of sharpness can also be attributed to the flow field becoming three-dimensional as a result of wall friction

The attenuation of the waves is caused primarily by the viscous mixing of the primary and secondary streams along the shear layer (Shapiro 1953) As the two streams are entrained into the shear layer, the near-inviscid primary core is gradually consumed and the velocity of the center flow decreases with increasing distance from the nozzle exit Eventually the flow becomes subsonic and waves can no longer be sustained In addition with each reflection the waves interact with the shear layer This interaction is evident from Figure 4.1(a), which shows that the incident waves penetrate the viscous layer before being reflected back towards the supersonic core

4.2.2 Underexpanded Test Cases

When the primary pressure is increased above the critical pressure the primary flow undergoes further expansion outside the nozzle to adjust to the surrounding pressure ($P_{s,2}$) Figures 4.2 through 4 6 show that the primary core changes considerably as the primary is underexpanded, and that the shear layers adjust to these changes accordingly

A representation of an underexpanded ejector flow field for the ideal inviscid case is given in Figure 4 7 The core structure seen in Figures 4 2 through 4 6 clearly resembles the ideal flow shown in Figure 4 7 The photographs show that Prandtl-Meyer expansions develop at the exit of the nozzle These expansion fans (wave fans a – b and c – d, Figure 4 7) become increasingly wider as the primary pressure is increased. As the flow passes through the expansion waves, the flow accelerates and the streamlines are bent outwards Across the expansion fans and near the core boundary (in regions II Figure 4 7) the flow speed is higher than at the nozzle exit and the streamlines are inclined with respect to the main flow direction The primary core widens forcing the shear layers to bend towards the secondary This change in local flow direction is either absent or very small in the core flow of the *baseline* test case (Figure 4 1) supporting further the claim that the residual waves are relatively weak As expected, the waves observed inside the nozzle for the *baseline* test case

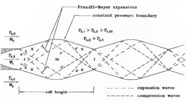

Figure 4.7 Structure of the supersonic core in an underexpanded ejector for inviscid flow

are also present in all underexpanded test cases as they are essentially independent of the primary pressure.

The Prandtl-Meyer expansions are reflected from the shear layer as compression waves (waves a', b', c', and d', Figure 4.7) to adjust the core to the local boundary conditions. The flow speed decreases across these waves and the streamlines are turned back towards the center of the core, causing the shear layer to bend accordingly. This pattern is repeated as the waves are reflected from the shear layer (constant pressure boundary) in unlike sense. In this manner, the waves give rise to the shock-cell structure common in underexpanded jets, and cause the shear layers to have a wavy or lobed appearance. The shock-cell structure eventually dissipates due to viscous effects.

4.2.3 Measurements obtained from Schlieren Visualization

Useful quantitative information about the local flow conditions can be inferred from the Schlieren images with the aid of supersonic flow theory. As explained in Section 4.2.1, finite waves are present in the primary core of the *baseline* test. Inspection of Figure 4.1 reveals that the waves at the nozzle exit (incident and reflected) make an average angle of approximately 34° (±1°) with the flow direction. This angle corresponds to the flow Mach angle, α, and is related to the flow Mach number, M, by the expression

$$\sin \alpha = \frac{1}{M} \tag{4.2}$$

Substitution of the measured value of α gives M = 1.79 (±0.05), which is in close agreement with the nominal (i.e. design) Mach number of the nozzle and the measured values presented earlier. Similar results can be obtained for the remaining test cases by considering the Mach angles inside the nozzle.

Mach angles can also be used to estimate the flow velocity in other regions of the supersonic core. As discussed earlier, expansion of the jet continues outside the nozzle for cases where the primary is underexpanded, and the primary core structure resembles that shown in Figure 4.7. It is known that the flow in region III (Figure 4.7) has crossed two families of Prandtl Meyer expansions and the pressure in this region is actually lower than the pressure of the secondary stream. Further, the pressure in region III is the lowest in the entire flow field and the velocity is the highest. It can be shown that the pressure in region III ($P_{s,III}$) for the ideal inviscid case is given by

$$\frac{P_{0,1}}{P_{s,III}} = \frac{P_{0,1}}{P_{s,1}} \frac{P_{s,1}}{P_{s,2}} \frac{1}{2 - P_{s,1}/P_{s,2}} \qquad (4.3)$$

Hence, the Mach number in this region can be predicted using the pressure ratio given by this expression and Equation 4.1.

The Mach number in region III can also be determined from the Mach angle of the waves immediately upstream (waves b and d) measured downstream of their intersection. Table 4.5 shows the predicted results and the values obtained from the measurements. The Mach angles were obtained from the most downstream waves of the first Prandtl-Meyer expansions seen in the Schlieren photographs and correspond to half the included angles between the two families of waves. The table also gives the maximum centerline ($y = 0$) Mach numbers based on measurements of (a) total primary pressure and minimum side wall pressure (Equations 4.1 and 4.3) and (b) minimum side wall pressure and corresponding pitot pressure (Equation 4.4 as discussed in Section 4.3.2).

In computing Mach number using method (a) it is assumed that the total pressure of the flow in region III is equal to the total pressure of the primary. Further, in both methods

Table 4.5 Comparison of predicted and measured flow conditions in regions of maximum expansion

Test Case	Predicted		Schlieren		Total, Pitot and Side Wall Pressures				
	P_0/P_x Equation 4.3	Mach number Equation 4.1	Mach angle (degrees)	Mach number Equation 4.2	x (cm)	maximum $P_{0,1}/P_x$ (x, y = 0)	Mach number Equation 4.1	maximum P_{pit}/P_x (x, y = 0)	Mach number Equation 4.4
1	5.75	1.80	34.0 ± 1.0	1.79 ± 0.05	1.0	5.77 ± 0.20	1.80 ± 0.04	4.80 ± 0.17	1.83 ± 0.04
2	6.61	1.89	31.0 ± 1.0	1.94 ± 0.06	2.0	6.38 ± 0.22	1.87 ± 0.04	4.96 ± 0.18	1.86 ± 0.04
3	7.60	1.98	30.0 ± 1.0	2.00 ± 0.06	2.0	7.29 ± 0.27	1.95 ± 0.04	5.48 ± 0.21	1.97 ± 0.04
4	8.78	2.07	28.0 ± 1.0	2.13 ± 0.07	3.0	8.60 ± 0.35	2.06 ± 0.05	5.70 ± 0.24	2.01 ± 0.05
5	10.2	2.17	27.0 ± 1.0	2.20 ± 0.08	3.0	10.2 ± 0.5	2.17 ± 0.05	6.35 ± 0.30	2.13 ± 0.05
6	11.9	2.27	26.0 ± 1.0	2.28 ± 0.08	3.0	11.2 ± 0.5	2.23 ± 0.06	6.78 ± 0.33	2.21 ± 0.06
7	14.0	2.37	25.5 ± 1.0	2.32 ± 0.08	3.0	12.3 ± 0.6	2.29 ± 0.06	7.17 ± 0.37	2.28 ± 0.06
8	16.7	2.48	24.5 ± 1.0	2.41 ± 0.09	3.0	13.7 ± 0.7	2.36 ± 0.07	7.69 ± 0.41	2.37 ± 0.07
9	20.2	2.61	23.5 ± 1.0	2.51 ± 0.10	4.0	15.2 ± 0.8	2.42 ± 0.07	N/A	N/A
10	25.0	2.75	23.0 ± 1.0	2.56 ± 0.11	4.0	18.2 ± 1.2	2.54 ± 0.09	N/A	N/A
11	32.1	2.91	22.5 ± 1.0	2.61 ± 0.11	4.0	20.2 ± 1.4	2.61 ± 0.09	N/A	N/A

it is assumed that the side wall pressure is a good approximation of the static pressure in the flow As explained later in Sections 4.4 and 5 3 4 the results substantiate the latter assumption

The predicted Mach numbers are remarkably close to the results obtained from the Mach angles, with the exception of the two most underexpanded test cases As the exit pressure difference ($\Delta P_s = P_{s,1} - P_{s,2}$) increases, the inviscid-flow isentropic predictions are expected to be less accurate, which is precisely the trend observed in Table 4 5 However the Mach numbers calculated from Mach angles are in close agreement with the values computed using pressure measurements Further, the minimum side wall pressure (Section 4 4 1) used for computations in (a) and (b) above always occur in the region immediately downstream of the first Prandtl-Meyer expansions

These results further demonstrate the consistency of the experimental conditions among the different test series, and also show that the flow fields investigated follow the basic fundamental trends predicted by theory

4.3 Pitot-Pressure Traverses

The data obtained from pitot-pressure traverses was used alone or in conjunction with the other measurements to accomplish several objectives. Among these, the most important are to

(1) establish the quality of the primary and secondary exit flows (i.e. the flow entering the mixing tube)

(2) characterize the mean flow-field structure for all test cases and identify any differences

(3) compute total pressures and Mach numbers along the mixing tube centerline

(4) characterize the development of the shear layers and mixing of the primary and secondary streams in the *near field*, and

(5) compute properties at the exit of the mixing tube and the overall ejector performance.

To help understand the results, the relationship between impact pitot-pressure, total pressure and flow speed is briefly discussed below. Item (1) and (2) above are then discussed, while the remaining are treated in the following chapter. Sample results are also presented to demonstrate the repeatability of the measurements.

4.3.1 Pitot Pressure, Total Pressure and Flow Speed

Due to the nature of the flow fields considered here, the impact probe encounters a wide range of flow regimes. Figure 4.8 shows a typical pressure traverse across an ejector flow field like the ones investigated here. Such a traverse can be expected in the *near field* somewhere between x_0 and x_1 as shown in Figure 1.1. Across the shear layers the probe is expected to encounter very steep velocity gradients. Further, during a traverse the probe is likely to cross from subsonic to supersonic regions (and vice-versa) through much of the mixing tube length. To interpret the data it is necessary to clearly distinguish the different flow regimes.

In regions where the flow is subsonic, the impact pressure seen by the probe, P_{pit}, is approximately equal to the local total pressure of the flow, provided the probe is oriented directly into the flow. If the flow is supersonic, a normal shock is formed in front of the probe and the impact pressure corresponds to the total pressure downstream from the shock. This pressure is always lower than the stagnation pressure upstream. Further, the fraction by which total pressure drops across a normal shock increases with Mach number.

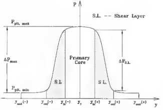

Figure 4.8 Representation of a typical pitot pressure traverse in an ejector flow field

In the case of supersonic flow, the impact pressure can be related to the flow Mach number (before the shock), M, through the Rayleigh expression

$$\frac{P_{pit}}{P_s} = \left(\frac{\gamma+1}{2}M^2\right)^{\frac{\gamma}{\gamma-1}}\left(\frac{2\gamma}{\gamma+1}M^2 - \frac{\gamma-1}{\gamma+1}\right)^{\frac{1}{1-\gamma}} \tag{4.4}$$

where P_{pit} and P_s are the total pressure after the shock and the static pressure of the flow respectively. Hence, wherever the flow is supersonic ($P_0 / P_s \geq 1.89$, Equation 4.1), either the flow static pressure or the Mach number must be known to obtain total pressure from Equations 4.1 and 4.3. In Chapter 5 it will be argued that the static pressure varies primarily in the streamwise and transverse directions (x and y in Figure 3.1) while is near constant in the spanwise direction (z in Figure 3.1). Thus Equation 4.4 can be solved for Mach number using pitot-pressure and side wall pressure measurements.

4.3.2 Primary and Secondary Exit Flows

Among the rig-design criteria explained in Section 3.3 was to provide a piece wise uniform, near parallel flow at the primary and secondary exit plane (x = 0). This implies that the primary and secondary flow properties must be near uniform at the exit plane. Figure 4.9 shows the pressure traverses made at x = 0 for each test case except No. 11 (two traverses for each test case). As explained in Section 3.5.2, at a few probe streamwise positions the flow in the mixing tube becomes choked for the high primary flow cases (including x = 0 for test case 11), and the desired flow conditions cannot be sustained. The pitot pressures are normalized by the average secondary exit pressure $(P_{s,2a} + P_{s,2b}) / 2$, for the corresponding run.

Figure 4.9 shows that pitot pressure is approximately uniform across the secondary exits in all cases (i.e. $y / H_{e\,nozzle} \leq -0.7$ and $y / H_{e\,nozzle} \geq 0.5$). Close inspection of all the

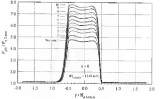

Figure 4.9 Pitot pressure traverses made at the exit plane (x = 0)

data in Figure 4.9 shows that, in these regions, pitot pressure deviates by less than 2.6% from the average and that the largest standard deviation for the ten cases shown is 0.65% of the average. In the region corresponding to the supersonic primary ($-0.65 \le y / H_{s,nozzle} \le 0.35$), pitot pressure is less uniform and exhibits a dip near the center of the jet. It was determined from the data that pitot pressure varies between 3.1% and 3.8% across the top of the traverse. Nevertheless, this variation is considered small for the purpose of this study. Further, a slight property variation is expected at the primary exit and can be explained as follows.

The exit properties of a well-designed converging-diverging nozzle are uniform only in the ideal case. In practice, however, these properties may vary because the velocity at the throat is not uniform (Shapiro, 1954, p. 826-840). Normally, the flow near the wall reaches sonic velocity upstream from the throat, in the converging section of the nozzle. Although the centerline Mach number is close to unity at the throat, the flow speed increases towards the wall becoming slightly supersonic. This effect is somewhat amplified in the diverging section of the nozzle and causes the exit flow to be faster near the wall.

By letting $M = 1.8$, Equation 4.3 gives $P_{pit} / P_s = 4.69$. The traverse measurements for the *baseline* test case result in $P_{pit} / P_s = 4.61$ at $y = 0$, which is within 2% of the predicted value. Conversely, the experimental value of P_{pit} / P_s at $y = 0$ for any traverse in Figure 4.9 gives $M = 1.8$. Near the wall the experimental value of P_{pit} / P_s is higher than at the centerline. Here, P_{pit} is higher and P_s is approximately equal or lower (as explained in Section 4.4.1) than at $y = 0$. Therefore, the flow must be faster near the wall ($P_{pit} / P_s \uparrow \rightarrow M \uparrow$). Small machining errors and boundary layers could also have resulted in slightly nonuniform exit properties, as explained earlier in Section 4.2.

Because all pressure traverses are for $z = 0$ (Figure 3.1), there is no direct measure of how much the flow properties vary in the spanwise direction. However, it is shown in Chapter 5 (Section 5.4.2) that near uniform spanwise velocity and pressure distributions satisfy continuity at $x = 0$.

Lastly, it would appear from Figure 4.9 that the primary jet is shifted in the negative y direction by approximately 1.2 mm ($y / H_{e\,nozzle} = 0.1$). In fact, an offset exists in most traverses between $x = 0$ and $x = 26$ cm in the same direction, although the offset amount varies somewhat most likely because the jet is not perfectly symmetric. It is believed that this was caused by a systematic error in the pre-traverse positioning of the probe. The error is, however, small and has no consequence in the results presented here.

4.3.3 General Observations from Pitot Pressure Traverses

The test results for the pitot pressure test-series are presented in Figures 4.10 through 4.20 for the eleven test cases. The traverses are normalized as described earlier and are grouped in order of increasingly larger streamwise distances. The vertical scale for all plots in a given test case is kept constant. Several observations can be made from these results which (a) help characterize the development of the different flow fields and (b) show agreement with the expected behavior of ejector flow fields. These observations are discussed next.

The measured profiles are typical of shear-layer flows (as discussed in Section 4.2.1). Each set of traverses shows how momentum is gradually transferred from the primary to the secondary along the mixing tube. Initially, the shear layers (or mixing layers) are thin and the velocity gradients are very steep. With increasing axial distance, primary and secondary fluid elements are progressively entrained into the layers where they mix and exchange

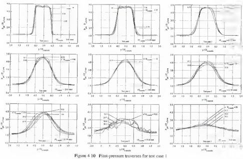

Figure 4.10 Pitot-pressure traverses for test case 1

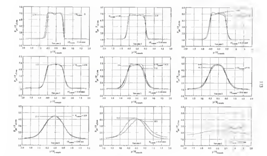

Figure 4.11 Pitot pressure traverses for test case 2

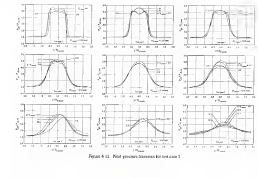

Figure 4.12 Pitot pressure traverses for test case 3

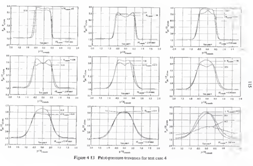

Figure 4.13 Pitot-pressure traverses for test case 4

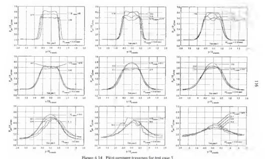

Figure 4.14 Pitot pressure traverses for test case 5

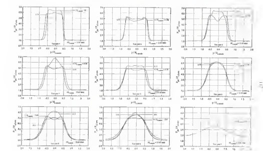

Figure 4.15 Pitot pressure traverses for test case 6

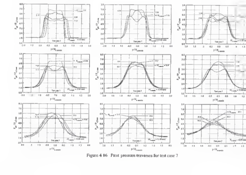

Figure 4.16 Pitot pressure traverses for test case 7

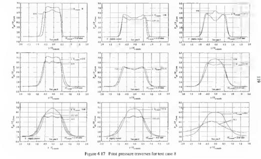

Figure 4 17 Pitot pressure traverses for test case 8

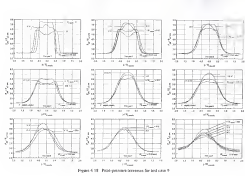

Figure 4.18 Pitot-pressure traverses for test case 9

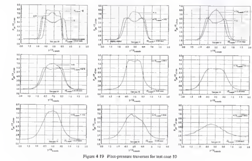

Figure 4.19 Pitot-pressure traverses for test case 10

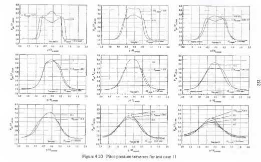

Figure 4.20 Pitot pressure traverses for test case 11

momentum. As a result, the shear layers grow and the secondary fluid is accelerated by the primary.

For all test cases the traverses made early in the mixing tube show that pitot pressure is approximately symmetric about the center of the traverse. With increasing axial distance, the profiles become slightly more uneven. Less than perfectly symmetric primary or secondary exit flows are likely to cause unevenness in the flow.

4.3.3.1 Ideally expanded test case

The traverses for the *baseline* test case are given in Figure 4.10. For this test case the high velocity region of the flow field (i.e. the region between the outer edges of both shear layers, Figure 1.1) grows monotonically in the streamwise direction. This region will be referred to here as the *plume* of the ejector flow field. The outer edges gradually move closer to the walls as the secondary fluid is entrained. These boundaries correspond to the location on either side of a traverse where pitot pressure begins to rise (y_{out} in Figure 4.8).

In the *near field* ($x / H_{e\ nozzle} \leq 11.9$, Figure 4.10) the primary core remains well defined. Here, the pressure near the center of the core remains approximately at the same level as the pressure at the nozzle exit ($4.4 \leq P_{pt} / P_{s,2\ exit} \leq 4.7$). The moderate fluctuation observed is due to the residual waves. Farther downstream, starting near $x / H_{e\ nozzle} = 11.9$, the *plume* continues to grow while the pressure at the center begins to decrease. This drop in pressure indicates that the two shear layers have merged near the center of the flow field and that all primary flow has been entrained (this point in the flow field is labeled x_1 in Figure 1.1). It will be shown in Chapter 5 that the velocity of the center flow gradually decreases in the streamwise direction beyond this point.

The pressure at the ends of the traverse ($y / H_{e\,nozzle} = \pm 1.56$) begins increasing at $x / H_{e\,nozzle} = 15$. As implied in Figure 4.10, this pressure rise indicates that the shear layers have reached the mixing-tube walls and that all secondary has been entrained (x_2 in Figure 1.1). Close inspection of Figure 4.10 shows that the pressure on the positive end of the traverse ($y / H_{e\,nozzle} = +1.56$) increases first, indicating that shear layer on the positive side reaches the wall first.

It is unclear what causes this small bias of the flow towards one side. One possible explanation is that the flow leans to one side as a result of subtle asymmetries in the flow at $x = 0$ or in the test section hardware. It is also possible that this is caused by instabilities inherent to the ejector flow field. Yet another explanation is that the probe introduces instabilities which affect the flow causing it to develop unevenly.

Once the layers reach the walls, the pitot pressure across the *plume* decreases rapidly, while the pressure towards the ends of the traverses continues to increase. Here, the pressure profiles lose the smooth-curve, bell-shape appearance exhibited earlier in the mixing tube and begin to break up. This is clearly seen from the traverses made in the region $24.8 \leq x / H_{e\,nozzle} \leq 28.2$, as evidenced by their jagged or irregular appearance. Further, this is the only region for the *baseline* test case where the pressure profiles are not repeatable. Figure 4.21 shows several traverses made in this region for test case 1. These results suggest the onset of large-scale turbulence which rapidly distributes momentum across the flow. Hill (1965) states that confined turbulent jets undergo considerable changes when they reach the wall, and can induce a recirculation region.

Towards the end of the mixing tube ($x / H_{e\,nozzle} \geq 29.7$), pitot-pressure becomes increasingly more uniform, as the flow field approaches an ideal fully-mixed condition.

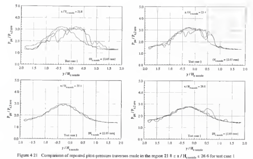

Figure 4.21 Comparison of repeated pitot-pressure traverses made in the region $21.8 \le x / H_{c,nozzle} \le 26.6$ for test case 1

Although the pressure is still higher near the center; the variation across the flow is significantly less. The large-scale flow instabilities observed earlier on longer exist and the pitot pressure traverses are very repeatable, once again

4.3.3.2 Underexpanded test cases

Similar observations can be made from the results for the underexpanded cases. However, some key differences between the *baseline* and the underexpanded flow fields are also evident. The shear layers for the latter flow fields develop under the influence of a different primary core. In Section 4.2.2 it is explained that the core continues to expand outside the nozzle when the primary is underexpanded.

The shear layers in the underexpanded ejector must adapt to the expansion and contraction of the core and, therefore, their boundaries are not as uniform as those for the ideally expanded ejector. This behavior is easily observed from the Schlieren images, and is confirmed by the traverses made in the *near field*, particularly in the highly underexpanded primary flows (e.g. Figures 4.17 through 4.20, in the region $0 \leq x / H_{e\,nozzle} \leq 10.3$). In the *near-field*, the width of the *plume* increases and then decreases in a relatively short distance. Results presented in Chapter 5 display this graphically.

Figures 4.13 through 4.20 show that at short distances the pitot pressure at the center of the primary core fluctuates, unlike the *baseline* flow where it remains approximately constant. This streamwise variation of pitot pressure is directly related to the local change in free-stream Mach number (calculations presented in Chapter 5 show this more explicitly). As explained in Section 4.3.1, the impact pitot pressure depends on Mach number when the flow is supersonic.

In some *near field* traverses, the pressure varies across the primary core in a nearly symmetric fashion (e.g. Figure 4.17 $x / H_{c\,nozzle}$ = 3.16 and 3.95). This is also in contrast to the *baseline* case for which pitot pressure shows little variation across the core. This pressure variation occurs whenever the probe crosses expansion or compression fans like those in Figure 4.7. This is easily verified by inspection of the Schlieren photographs at the positions where this behavior is observed.

In all underexpanded cases, the pressure at the end of the traverses also begins to rise at $x / H_{c\,nozzle}$ = 15 approximately. This suggests that primary underexpansion does not increase the net growth of the *plume* and the shear layers, at least in the *near field*. For test cases 2 through 5 (Figures 4.11 through 4.14), the shear layers on the positive side reach the wall first, while the opposite is true for remaining cases.

In test case 5 (Figure 4.14), large-scale turbulence is observed once the shear layers reach the walls (similar to that observed for the *baseline* case). This is evident from the break-up of the flow as shown by the traverses in Figure 4.22. Results presented in Chapter 5 suggest that this break-up maybe related to a supersonic/subsonic transition. It is likely that this type of flow break-up also occurs in test cases 2, 3 and 4. However, traverse data were not collected in that section of the mixing tube for the even-numbered cases, and there is inconclusive evidence of flow break up for case 3.

In general, momentum transfer is less complete as the primary flow is underexpanded further. The exit pitot pressure profiles are increasingly less uniform. However, results presented in Chapter 5 suggest that flow case 5 (Figure 4.14) departs somewhat from this trend.

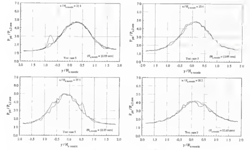

Figure 4.22 Comparison of repeated pitot pressure traverses made in the region $21.8 \le x / H_{e\ nozzle} \le 31.3$ for test case 5

4.3.4 Repeatability of the Pitot-Pressure Traverses

A few redundant traverses were made to establish the repeatability of the pitot-pressure measurements. Most redundant measurements were obtained by making two or three runs successively for a given test case and probe position, without making any flow adjustments or hardware changes. Some traverses, however, were repeated several days after the original measurements were made, and required complete readjustment of the flow conditions and repositioning of the probe.

The two exit-plane traverses shown for test cases 1 through 10 in Figure 4.9 are typical for consecutive runs. Figure 4.23 shows traverses made at x = 12 cm for the odd numbered test cases. Here, the runs were made 15 days apart, and the flow conditions were adjusted independently for each run. These results clearly demonstrate that pitot-pressure profiles are very repeatable when the flow conditions are duplicated. As seen in Figure 4.9, consecutive runs always resulted in nearly identical flow conditions, at least within the uncertainty of the measurements. Further, Figure 4.23 shows that the flow conditions can be duplicated with enough accuracy in completely independent runs to ensure consistency of the results. The repeatability of the pitot pressure profiles also suggests that the mean flow field is steady. The exceptions to these findings were discussed in the previous section.

4.4 Side-Wall Static Pressure Measurements

Side wall pressures were measured for all test cases as described in Section 3.5.3 along the entire length of the mixing tube (x = 0 to x = 43.62 cm). Measurements were made at y = 0 (Δx_{max} = 1 cm) and y = ±1.97 cm (Δx_{max} = 2 cm) to obtain the streamwise pressure

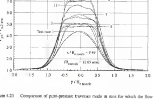

Figure 4.23 Comparison of pitot-pressure traverses made in runs for which the flow conditions were independently adjusted

distribution for each flow case. The two pressure-plate positions resulted in an overlap of the measurements between x = 18 cm and x = 27 cm.

The streamwise side wall pressure distributions are shown in Figures 4.24 through 4.34. The pressures in these plots are the average of the normalized measurements for two separate runs (Section 3.5.3). The single-run side-wall pressures were normalized by the average secondary exit pressure, $(P_{s,2a} + P_{s,2b}) / 2$. As explained in Section 3.5.3, several runs were required to collect all the measurements needed for each test case.

The transverse static pressure variation is discussed in Chapter 5, Section 5.3.4, using the test measurements and theoretical arguments.

4.4.1 Centerline Side-Wall Pressure

The variation in centerline (y = 0) side-wall pressure in all cases clearly shows the effect of the expansion and compression waves in the supersonic core. On the average, the centerline pressure follows the pressure of the surrounding flow, increasing slightly in the first half of the mixing tube and more rapidly in the downstream section. The cyclic variation of the centerline measurements appears superimposed to the surrounding pressure. This variation gradually decreases with distance, disappearing in most cases before the end of the mixing tube. At the mixing tube exit, the side-wall pressure is approximately uniform across the flow in all cases.

In the *baseline* test case (Figure 4.24) the waves result in peak-to-peak pressure variations of roughly 5%. Because the maximum variation observed occurs when the flow crosses two waves (or wave fans) of similar strength but different families, each wave (or fan) must lead to roughly half this change (i.e. ~2.5% in this case). Therefore, it can be concluded that the waves originating inside the nozzle are relatively weak. Further

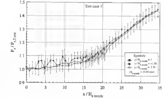

Figure 4 24 Streamwise side wall pressure distribution for test case 1

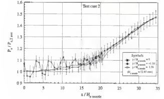

Figure 4 25 Streamwise side-wall pressure distribution for test case 2

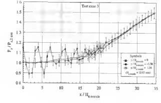

Figure 4.26 Streamwise side-wall pressure distribution for test case 3

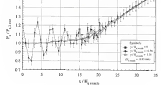

Figure 4.27 Streamwise side wall pressure distribution for test case 4

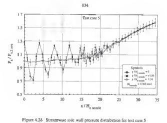

Figure 4.28 Streamwise side-wall pressure distribution for test case 5

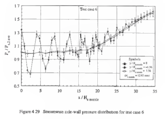

Figure 4.29 Streamwise side-wall pressure distribution for test case 6

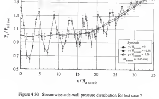

Figure 4.30 Streamwise side-wall pressure distribution for test case 7

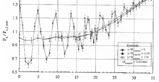

Figure 4.31 Streamwise side-wall pressure distribution for test case 8

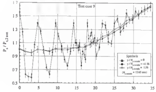

Figure 4.32 Streamwise side-wall pressure distribution for test case 9

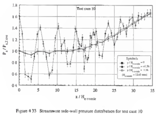

Figure 4.33 Streamwise side-wall pressure distribution for test case 10

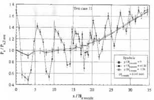

Figure 4.34 Streamwise side wall pressure distribution for test case 11

Figure 4.24 shows that the wall pressure decreases from $x = 0$ to $x / H_{c,nozzle} = 0.79$ and then increases from $x / H_{c,nozzle} = 0.79$ to $x / H_{c,nozzle} = 1.58$. Inspection of the Schlieren images in Figure 4.1 show that the pressure tap of the third measurement, $x = 2$ cm, lies downstream from the waves reflected at the nozzle exit. Hence these waves must be of the compression type and those inside the nozzle must be expansion waves, as claimed in Section 4.2.1.

As the primary is underexpanded, the centerline pressure reflects the cyclic expansion and recompression characteristic of the shock-cell structure. The drop in pressure immediately outside the nozzle is brought about by the Prandtl Meyer expansions that originate at the nozzle exit. In every underexpanded case, the lowest side-wall pressure measured always occurs downstream from these expansions which is in direct agreement with the discussion of Section 4.2.1.

The strength of the waves and number of shock cells in the core clearly increase with primary pressure. For example, based on the number of complete cycles for the centerline pressure in Figure 4.25, there are approximately five shock cells in test case 2. For test case 11, eight shock cells can be identified from Figure 4.34. This result is expected, and indicates that the supersonic core (Figure 1.1) reaches farther downstream for cases with higher primary pressure (i.e. higher flow rate) for these waves are sustained only where the flow is supersonic. Mach number calculations presented in Chapter 5 confirm that the core flow remains supersonic for a longer distance in these cases.

The results also show that the waves lose strength with increasing axial distance. This loss of strength was discussed in Section 4.2.1, and can be attributed to (a) the interaction of the waves with the shear layer, (b) the consumption of the near inviscid primary core, and (c) the losses associated with stronger compression waves.

Inspection of Figures 4.24 through 4.34 reveals that the pressure distributions have a jagged appearance where measurements for the two pressure plate positions overlap. This is believed to be a surface effect. The two plate positions result in slightly different surface conditions. In either configuration, two gaps (under 0.2 mm) are formed along the side wall of the mixing tube. One is formed between the plenum and the first sidewall section, and the other is formed between the two side walls sections (Section 3.5.3). These gaps are likely to disturb the boundary layer, hence changing its thickness and the local flow area. The position of the second gap changes when the long and short side walls are swapped (thus changing the location where the boundary layer is perturbed). In addition, the dimensions of these gaps can also change. Both effects are expected to change the pressure field slightly. It is also conceivable that small differences in the surface quality of the two side walls could have contributed to this result.

4.4.2 Off-Center Side Wall Pressure

Figures 4.24 through 4.34 show that the side-wall pressure at $y / H_{e,nozzle} = \pm 1.56$ does not vary considerably early in the mixing ($x / H_{e,nozzle} \leq 10$), increasing only by a few percent. Here, the pressure distribution is nearly identical on both sides of the primary core. At longer axial distances ($10 \leq x / H_{e,nozzle} \leq 18$) the off-center pressure increases at a slightly faster rate. In this region, the measurements on either side appear to differ more (2% to 3%) although they still remain within uncertainty from each other. Most of the pressure rise takes place further downstream ($x / H_{e,nozzle} \geq 20$). The off-center measurements differ by less than 3% in this region, and the agreement between the two sides becomes progressively better. Further, the centerline and off-center pressures seem to converge with increasing streamwise distance.

At small distances $(x / H_{e\ nozzle} \le 10)$, the off-center pressure for cases with higher underexpansion varies axially in a way that almost mirrors the periodic centerline pressure variation. This result is expected and can be explained as follows. Wherever the supersonic core expands, the surrounding secondary streams are forced through smaller effective flow areas, thus increasing their speed and reducing the local pressure The opposite is true where the supersonic core contracts This issue is treated in more detail in Section 5 3.4

4.5 Acoustic Measurements

As discussed in Chapter 2, the screech that has been reported in underexpanded ejectors has also been linked to changes in ejector performance In this investigation the acoustic emissions of each test case were measured to (a) identify any flow-generated screech and (b) to compare the magnitude and frequencies of these emissions between the various flow cases. These measurements were obtained as discussed in Section 3 5.4 and are presented below In the following chapter, these results are examined together with the performance calculations to establish any connection between screech and performance for the cases considered here

4.5.6 Streamwise Acoustic Measurements

The acoustic measurements for all test cases are presented in Figures 4 35 through 4 45 The figures correspond to the spectral sound-pressure level (SPL) obtained using the 0 – 20 kHz bandpath of the Fourier analyzer Although measurements were also obtained using bandpaths of 0 – 50 kHz and 0 – 100 kHz most of the screech emissions were detected in the 0 – 20 kHz range. This bandwidth also provides the highest frequency resolution of the three ranges used (12 5 Hz)

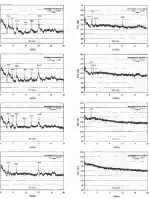

Figure 4.35 Acoustic spectra for different microphone positions and a 20 kHz band pass for test case 1

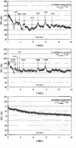

Figure 4.36 Acoustic spectra for different microphone positions and a 20 kHz band pass for test case 2

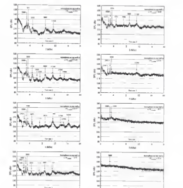

Figure 4 37 Acoustic spectra for different microphone positions and a 20 kHz band pass for test case 3

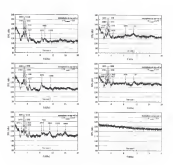

Figure 4 38 Acoustic spectra for different microphone positions and a 20 kHz band pass for test case 4

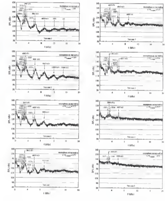

Figure 4 39   Acoustic spectra for different microphone positions and a 20 kHz band pass, for test case 5

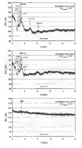

Figure 4 40 Acoustic spectra for different microphone positions and a 20 kHz band pass for test case 6

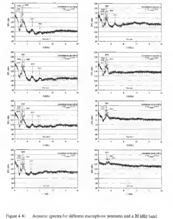

Figure 4 41 Acoustic spectra for different microphone positions and a 20 kHz band pass for test case 7

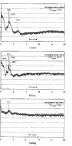

Figure 4.42 Acoustic spectra for different microphone positions and a 20 kHz band pass, for test case 8

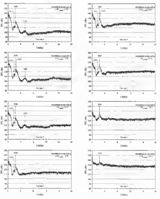

Figure 4 43 Acoustic spectra for different microphone positions and a 20 kHz band pass for test case 9

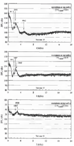

Figure 4 44 Acoustic spectra for different microphone positions and a 20 kHz band pass, for test case 10

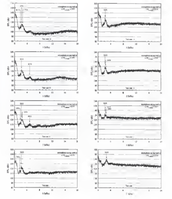

Figure 4 45 Acoustic spectra for different microphone positions and a 20 kHz band pass for test case 11

The screech expected in these type of flow fields should appear as well-defined peaks in the SPL spectra, resembling near-discrete tones. Further these acoustic peaks are characterized by relatively high acoustic power. The frequencies of the most distinct spectral features are indicated on each SPL spectrum. Several observations can be made from these measurements.

In all flow cases the acoustic emissions contain several peaks or spectral features. These acoustic features occur predominantly in the initial region of the mixing tube $2.01 \leq x / H_{e\ nozzle} \leq 8.33$ (in agreement with results presented by Yu and Dosanjh 1972, Section 2.2.1). In general these peaks are attenuated with increasing streamwise distance, which agrees with the directionality predicted and measured for flow-generated screech emissions (e.g. Powell 1953a). In some cases, they are completely absent from the spectra obtained at the most downstream measuring station. In contrast, there is a clear increase in the floor-level spectral intensity with increasing axial distance. The magnitude of this rise is approximately between 10 db and 20 db.

The measurements also show that the acoustic features differ considerably among the various flow cases. For the *baseline* test case (Figure 4.35) the spectra contain several peaks in the 0 – 20 kHz range. These peaks have a broadband appearance rather than the more narrow discrete like appearance reported for screech tones, and probably correspond to broadband shock noise (Norum and Seiner 1982). In addition to decreasing in intensity, some frequencies change slightly with position (e.g. the peaks near f = 5.0 kHz and f = 7 kHz).

The emissions for test case 2 (Figure 4.36) are very similar to those for the *baseline* case. All peaks appear to be broadband and their frequencies are very close to those observed for the ideally expanded flow, particularly those under 6 kHz. The peak frequencies above 7 kHz appear to differ slightly. For example, the spectral feature near 14 kHz found at $x / H_{e,\text{nozzle}} = 2.01$ in test case 2, is absent from the *baseline* case spectra. Also, the peak near 9.5 kHz in case 2 still persists at $x / H_{e,\text{nozzle}} = 6.75$, while the similar peak near 9.7 kHz in the *baseline* case is no longer detectable at the same location.

As the primary is underexpanded further, the occurrence of screech tones is evident from the spectra. For example, in test case 3 (Figure 4.37) the narrow emissions at $f = 2.9$ kHz and $f = 3.4$ kHz corresponds to flow-generated screech. The intensity of the screech lines is considerably higher than the intensity of their broadband counterparts. The number of screech frequencies and their intensities vary with test case. The intensity of the screech frequencies also varies with position. In general, screech intensity decreases at higher streamwise distances. However, unlike the broadband peak emissions, the screech emissions persist farther downstream.

All of these observations are in general agreement with behavior previously reported for underexpanded free jets and ejectors (Section 2.2).

Among the underexpanded flows, test case 5 (Figure 4.39) exhibits the most pronounced screech emissions. Most striking is that the screech for this case consists of a fundamental frequency or first harmonic ($f_{h1} = 3.0$ kHz) and up to four overtones or higher harmonics ($f_{h2} \approx 6.0$ kHz, $f_{h3} \approx 9.0$ kHz, $f_{h4} = 12.0$ kHz, and $f_{h5} = 15.0$ kHz). The fundamental and second harmonic are narrow peaks of high acoustic power and can be seen in the spectra for all measuring stations. The higher harmonics, on the other hand, are broadband peaks of lower power and are present only at short streamwise distances ($x / H_{e,\text{nozzle}} \leq 6.75$). Further, due to the broadband nature of these components, their peak frequencies do not always fall close to the harmonic frequencies. A few additional distinct screech frequencies occur in the neighborhoods of the fundamental and second harmonic. These also are narrow peaks which can be detected at most stations.

The screech emissions for test case 6 (Figure 4.40) also consists of a fundamental frequency (f_{F1} = 2.9 kHz) and an overtone (f_{h2} = 5.8 kHz). In this case the second harmonic is a broadband emission of relatively low acoustic power, and occurs only at short distances. A much weaker broadband peak located at f = 8.4 kHz most likely corresponds to a third harmonic. Like in test case 5, additional screech frequencies are found near the fundamental frequency. The intensities of all screech emissions for this case are considerably lower than those observed for test case 5.

The measurements for test cases 7 through 11 (Figures 4.41 through 4.45) are similar to those for case 6. In each case, a fundamental screech frequency can be detected at most measuring stations. One or two broadband harmonics are also found at small streamwise distances ($x / H_{s,\text{nozzle}} \leq 6.75$). The harmonics are attenuated and their peak frequencies decrease some (Δf = 100 Hz – 400 Hz) with increasing axial distance. Close inspection of the spectra also shows a slight decrease in the intensity of the fundamental frequency in the direction of higher primary underexpansion.

The above observations show that the nature of the acoustic emissions changes with test case 5. In cases 1 through 4 there is a gradual increase in screech, while the opposite trend is true for cases 6 through 11. Further, the intensity of the fundamental screech frequency for test case 5 reaches levels of up to 153 db, surpassing the highest screech intensities among all other test cases by more than 15 db. Calculations presented in

Chapter 5 show that ejector performance is slightly improved for this flow case (i.e. flow conditions $P_{s,1} / P_{s,2} = 1.28$, $P_{0,1} / P_{s,1} = 7.35$, and $\dot{m}_2 / \dot{m}_1 = 0.133$)

4.5.7 Comparison of Measurements from Opposite Walls

A limited number of measurements were obtained for the odd-numbered test cases to compare the acoustic emissions on both sides of the core flow. To collect these data the microphone was installed on the top and bottom mixing tube walls (Section 3.3.2.3), on separate runs but at the same streamwise ports. The microphone locations considered are $x / H_{e,nozzle} = 2.01, 6.75$

The 0 – 20 kHz SPL spectra obtained from these measurements are presented in Figures 4.46 through 4.51. In these figures the ordinate scale corresponding to the bottom wall data has been shifted by 10 db to allow comparison of the spectra.

The results indicate that the acoustic field is nearly symmetric about the $y = 0$ plane. The spectral features, in particular the screech tones are almost identical on both sides of the flow field for all cases. Along with other measurements presented earlier, these results show further that the flow field is approximately symmetric about the center plane $y = 0$. Because these are one-point measurements, however, it is not possible to determine whether the emissions are in phase or are shifted.

4.6 Effect of Pressure Probe on Test Measurements

Several tests were performed to quantify how much the probe affects the other measurements and to establish the extent of the probe intrusiveness in the flow field. These experiments involved flow visualization, and measurements of side wall pressures and

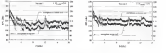

Figure 4 46 Comparison of acoustic emissions measured on opposite walls at two different streamwise positions for test case 1

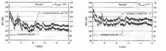

Figure 4 47 Comparison of acoustic emissions measured on opposite walls at two different streamwise positions, for test case 3

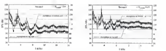

Figure 4 48 Comparison of acoustic emissions measured on opposite walls at two different streamwise positions, for test case 5

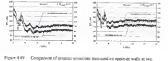

Figure 4 49 Comparison of acoustic emissions measured on opposite walls at two different streamwise positions for test case 7

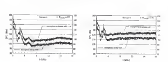

Figure 4 50 Comparison of acoustic emissions measured on opposite walls at two different streamwise positions, for test case 9

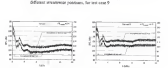

Figure 4.51 Comparison of acoustic emissions measured on opposite walls at two different streamwise positions, for test case 11

acoustic emissions The test procedure was described in Section 3 5 6 and the results are discussed next

4.6.1 Flow Visualization with Probe Installed

The Schlieren photographs obtained with the probe in the flow field for test cases 1 and 5 are shown in Figures 4 1(c) and 4.3(c), respectively To obtain these photographs the probe was positioned at the center of the flow ($y = 0$) In addition to these still photographs, motion picture video of the Schlieren image was obtained while traversing the probe across the flow

The still images show that the flow field upstream from the probe remains approximately unaffected The video showed that this is true irrespective of the probe's transverse position As expected, however there are significant changes in the flow structure immediately behind the probe stem. Because of the qualitative nature of the Schlieren images, it is difficult to establish how much these changes affect the early development of the flow field.

These tests also showed that there is no appreciable deflection or vibration of the probe during traverses as a result of aerodynamic loading This confirms the spatial resolution of the pressure traverses

4.6.2 Side Wall Pressures

The side-wall pressure measurements obtained with the probe installed at $x = 12$ cm and $x = 26$ cm, are shown in Figures 4 52, 4.53, and 4 54, for tests 1, 5, and 9 respectively The measurements made when the probe was not installed (Section 4 4) are also shown for

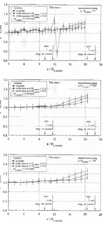

Figure 4.52 Comparison of side wall pressure measurements obtained with and without the probe installed for test case 1

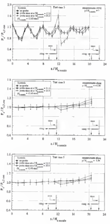

Figure 4.53 Comparison of side-wall pressure measurements obtained with and without the probe installed, for test case 5

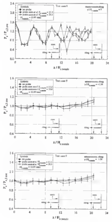

Figure 4.54 Comparison of side wall pressure measurements obtained with and without the probe installed, for test case 9

comparison. The pressure distributions for $y / H_{e\,nozzle} = -1.56$, 0 and +1.56 are shown in separate plots.

The results of these tests show several important trends. At short distances (for $x / H_{e\,nozzle} \leq 11$) the side-wall pressures are approximately unaffected by any disturbances caused by the probe. The measurements are nearly identical in this region, regardless of whether or not the probe is in the flow field. When the probe is installed at x = 12 cm (i.e. stem at $x / H_{e\,nozzle} = 11.5$), its presence is felt almost exclusively downstream from this position. This is in agreement with the flow visualization experiments. When the probe is installed at x = 26 cm (i.e. stem at $x / H_{e\,nozzle} = 22.6$), its presence is also felt upstream, yet its effect on side-wall pressure is smaller. One possible explanation for this is that at longer distances a larger percentage of the flow is subsonic. Hence, disturbances are more likely to propagate upstream and alter the flow accordingly.

As expected, the effect of probe intrusiveness is greatest at the upstream probe position. The effect is less important towards the end of the mixing tube. Side-wall pressures measured at $x / H_{e\,nozzle} = 34.5$, both in the absence of the probe and when the probe was installed at the same location (i.e. stem at $x / H_{e\,nozzle} = 22.6$), resulted in differences between 0.2% and 5%.

Pressure losses are inevitable when the probe is in the flow field and result primarily from (a) friction on the surface of probe stem, and (b) viscous interactions which occur behind the stem (e.g. interactions between the wake and the surrounding flow or the solid boundaries, slip lines in supersonic flow, etc.). Thus, these losses are greater upstream, where the mean flow velocity is higher. This is particularly true in an ejector, where the flow is constrained by the walls of the mixing tube.

It can be concluded based on these results that the probe disturbs the incoming flow primarily when it is installed where the flow is mostly subsonic. The disturbances are felt only relatively close to the probe, and the resulting changes in side-wall pressure are small for the test conditions studied.

4.6.3 Acoustic Emissions

The acoustic emissions measured with the probe installed at x = 12 cm and x = 26 cm, are shown in Figures 4.55, 4.56, and 4.57 for tests 1, 5, and 9, respectively. For each probe position (except x = 26 cm for case 1), measurements were obtained with the microphone installed at $x / H_{e\ \mathrm{nozzle}} = 6.75$ and 9.91. The corresponding acoustic spectra obtained without the probe are also shown for comparison.

The acoustic spectra for test case 1 show emissions which clearly are not present when the probe is not in the flow field. These emissions are similar to the screech observed in the underexpanded test cases. With the probe positioned at $x / H_{e\ \mathrm{nozzle}} = 11.5$, the induced peak emissions have a fundamental frequency and several well defined higher harmonics. The probe induced emissions are considerably less when the probe is installed farther downstream ($x / H_{e\ \mathrm{nozzle}} = 22.6$). Further, the only screech like frequency observed at this position ($f = 3.0$ kHz) is different from any frequency observed at the shorter probe position.

For test cases 5 and 9, on the other hand, the probe seems to have a buffering effect when installed at $x / H_{e\ \mathrm{nozzle}} = 11.5$. The screech observed when the probe is not in the flow field is almost completely attenuated. The only exception is the fundamental screech frequency which, although greatly reduced in intensity, is still present in the spectra. At $x / H_{e\ \mathrm{nozzle}} = 22.6$, the probe appears to have little effect on the sound emissions, as the spectra for this probe location closely resemble their counterparts obtained without the probe.

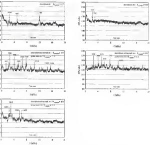

Figure 4.55 Comparison of acoustic emissions measured with and without the probe installed, for test case 1

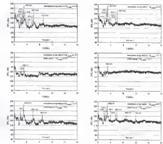

Figure 4.56 Comparison of acoustic emissions measured with and without the probe installed, for test case 5

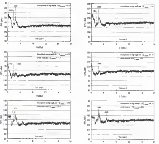

Figure 4 57 Comparison of acoustic emissions measured with and without the probe installed, for test case 9

Because of the limited data points considered in these validation tests and the large number of variables involved, it is difficult to make a clear assessment of how the probe affects the acoustic emissions in each test case. However, the results provide some clues.

For the six cases considered, the flow is supersonic in the center of the core at both probe positions considered. The probe at these locations results in strong waves as demonstrated by the flow-visualization results discussed in Section 4.6.1. The interaction of these waves with eddies in the shear layers (which is otherwise absent in the ideally expanded flow) result in screech emissions. Therefore, the probe acts as a source of screech in ideally or near ideally expanded flows.

In the case of underexpanded flows, the results suggest that the probe breaks up the wave pattern inherent to these flows. The periodicity of the wave pattern observed in Figure 4.3(b) for case 5 is clearly disrupted by the probe as shown in Figure 4.3(c). The end result is that screech intensity decreases significantly when the probe is positioned within the shock-cell structure of the underexpanded flow. At far enough streamwise positions, the shock-cell structure has nearly dissipated and the probe has little effect on the acoustic emissions, as demonstrated by the results. This result is of great significance to this study, as ejector performance is quantified for each test case (as explained in Chapter 5) based on traverses obtained at $x / H_{e,nozzle} \approx 34.5$.

Nevertheless, the results of these tests clearly show that further study is necessary to make a more complete assessment of the intrusiveness of the probe.

CHAPTER 5
FLOW FIELD DEVELOPMENT AND EJECTOR PERFORMANCE

5.1 Mass Flow Rates and Ejector Entrainment

Computation of ejector performance, whether in terms of the predicted or the actual behavior of the device, requires the knowledge of the primary and secondary flow rates. In many instances the mass entrainment ratio m_2/m_1 is a useful parameter to quantify performance. Within the context of this investigation the entrainment ratio is, in essence, a secondary independent variable.

The actual mass flow rates were computed separately from (a) orifice plate measurements, and (b) isentropic flow relations. The calculations are described in Appendix C. The first approach was used to determine the secondary flow rate and the total air flow rate into the ejector rig; the primary flow was deduced from the difference of the two flows. The orifice-plate measurements are expected to be more accurate and, therefore, were used for performance calculation. The second method was used as a backup and provided the ideal flow rates for the primary and each coflowing secondary stream.

The exit flow properties necessary to compute ejector performance were calculated using static-pressure measurements and pitot-pressure traverses made at the mixing-tube exit. To insure consistency of the results, the flow rates used to calculate performance are those measured for the exit-traverse runs, and correspond to the mean flow rate for three different runs. The results and uncertainties are presented in Table 5.1, along with the corresponding entrainment ratios.

Table 5.1. Mass flow rates and entrainment ratios computed from orifice plate and plenum measurements

Test Case	Orifice Plate Measurements			Isentropic Calculations from Plenum Pressures			
	$\dot{m}_1$ (kg/s)	$\dot{m}_2$ (kg/s)	$\dot{m}_2/\dot{m}_1$	$\dot{m}_1$ (kg/s)	$\dot{m}_{2a}$ (kg/s)	$\dot{m}_{2b}$ (kg/s)	$\dot{m}_2/\dot{m}_1$
1	0.103	0.049	0.478	0.105 ± 0.002	0.024 ± 0.010	0.025 ± 0.009	0.460
2	0.111	0.049	0.444	0.113 ± 0.002	0.025 ± 0.009	0.024 ± 0.010	0.433
3	0.118	0.049	0.416	0.120 ± 0.002	0.024 ± 0.010	0.024 ± 0.010	0.406
4	0.125	0.049	0.393	0.127 ± 0.002	0.024 ± 0.010	0.024 ± 0.010	0.384
5	0.132	0.049	0.371	0.134 ± 0.002	0.024 ± 0.010	0.024 ± 0.009	0.363
6	0.139	0.048	0.347	0.141 ± 0.002	0.024 ± 0.010	0.024 ± 0.009	0.343
7	0.146	0.048	0.329	0.148 ± 0.002	0.024 ± 0.010	0.024 ± 0.009	0.328
8	0.154	0.048	0.312	0.156 ± 0.002	0.024 ± 0.010	0.025 ± 0.009	0.311
9	0.161	0.048	0.298	0.163 ± 0.002	0.024 ± 0.009	0.024 ± 0.010	0.299
10	0.168	0.048	0.286	0.170 ± 0.002	0.024 ± 0.009	0.024 ± 0.009	0.287
11	0.177	0.048	0.271	0.178 ± 0.002	0.024 ± 0.010	0.025 ± 0.009	0.276

The results from both methods are in close agreement, and meet closely the test matrix requirements (Table 3.1). Since method (b) is based on the assumption of uniform exit properties, its agreement with the more reliable real flow orifice-plate measurements provides further evidence that the exit flows are near uniform. The orifice-plate results in Table 5.1 are plotted in Figure 5.1, together with the mean flow rates for the entire pressure traverse, side-wall pressures, and sound measurements test series. Figure 5.1 clearly shows that the flow conditions for the exit-traverse runs are representative of the flow conditions throughout the experiments. The entrainment ratios based on the orifice-plate measurements are plotted against primary exit pressure in Figure 5.2.

5.2 Streamwise Variation of Flow Speed

The Mach numbers at transverse coordinates of $y / H_{e\ \mathrm{nozzle}} = 0$ and ±1.56 were computed using the corresponding measurements of side-wall and pitot pressures. To this extent, it was assumed that the static pressure is approximately constant in the spanwise direction. The details of the calculations are given in Appendix C. The uncertainty of the off-center Mach numbers is high, particularly in the low Mach range ($M \leq 0.5$). As discussed in Section 4.1.1, Mach number calculations are very sensitive to errors in pressure for pressure ratios (P_{pt} / P_s) near unity. The pitot pressure at the off-center locations is relatively low in comparison to the full range of the probe transducer and, therefore, the uncertainty of the off-center measurements can be as high as 6%. The off-center Mach numbers are presented primarily to show trends and to aid in the discussion.

Figures 5.3 through 5.13 show the streamwise variation of Mach number for test cases 1 through 11. In these plots, only data points spaced with the smallest increment ($\Delta x = 1$ cm) were connected, and the uncertainties for the off-center Mach numbers were

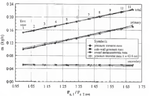

Figure 5.1 Flow rates versus normalized exit primary pressure for the pressure traverse side-wall pressure, and sound measurements test series

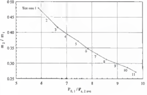

Figure 5.2 Entrainment ratio versus normalized total primary pressure for the exit-plane ($x / H_{e\,nozzle} = 34.5$) traverse runs

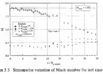

Figure 5 3   Streamwise variation of Mach number for test case 1

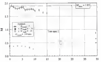

Figure 5 4   Streamwise variation of Mach number for test case 2

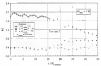

Figure 5.5   Streamwise variation of Mach number for test case 3

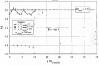

Figure 5.6 Streamwise variation of Mach number for test case 4

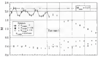

Figure 5.7 Streamwise variation of Mach number for test case 5

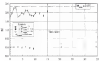

Figure 5.8 Streamwise variation of Mach number for test case 6.

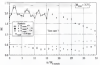

Figure 5 9 Streamwise variation of Mach number for test case 7

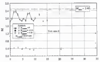

Figure 5 10 Streamwise variation of Mach number for test case 8

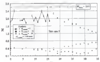

Figure 5 11 Streamwise variation of Mach number for test case 9

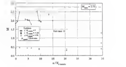

Figure 5 12 Streamwise variation of Mach number for test case 10

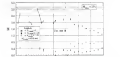

Figure 5 13 Streamwise variation of Mach number for test case 11 omitted for reasons discussed above The predicted, maximum Mach number (Table 4 5) is also shown for comparison.

All test cases exhibit a trend typical of ejector flows The high speed center flow decelerates in the axial direction while the surrounding flow in general accelerates At short distances the primary free stream Mach number fluctuates in accordance with the flow structure in this region (Sections 4.2.1 and 4.2.2). The fluctuations are small for the ideally and near ideally expanded test cases, becoming more pronounced as the primary pressure is increased. In this initial region the free-stream velocity of the primary core (Figure 1 1) also decreases slightly with distance due to viscous and nonideal effects The results agree qualitatively with those presented by Yu and Dosanjh (1972) for a Mach 1.5 free jet from an axisymmetric contoured nozzle

The *near-field* variation in Mach number is less clear for the most underexpanded flow cases (9 – 11) because of pitot-pressure data are not available at some locations In Section 3.5 2 it is explained that some traverses were not made due to probe induced choking Inspection of Figures 5 11 and 5 13 and the Schlieren images of Figures 4 5 and 4.6 shows that the choking occurs when the probe stem is positioned where the primary core is fully expanded (i.e. in regions of relatively high flow speed)

In most cases, the highest Mach number measured is very close to the predicted value. The agreement seems to decrease somewhat with increasing primary underexpansion, which is not unexpected for the ideal-flow predictions are less accurate as the strength of the waves in the core increases. However it is difficult to demonstrate this loss of accuracy because the data for the highly underexpanded cases are sparse in the fully expanded regions of the core

The speed of the core flow decreases at a faster rate farther downstream, where the Mach number no longer fluctuates (i.e. once the primary core is consumed, Section 4.3.3.1). The deceleration is approximately constant for each flow case. In test cases 1 through 5 the flow at the center of the mixing tube exit is in the high subsonic/sonic range ($0.8 \le M \le 1.0$). In all other cases the center flow remains slightly supersonic ($1.1 \le M \le 1.3$) at the end of the mixing tube.

In test case 1, the flow at $y = 0$ and $x / H_{e,nozzle} = 21.8$ has a Mach number of $M \approx 1.25$, whereas at $x / H_{e,nozzle} = 28.2$ it becomes subsonic everywhere across the mixing tube (the latter location corresponds to x_3 in Figure 1.1). Therefore, the flow break up which is observed in this region for test case 1 (Section 4.3.3.1) may be linked to the transition in flow speed. The same argument can be made for case 5, which becomes subsonic near the exit of the mixing tube and exhibits flow break-up in the region $21.8 \le x / H_{e,nozzle} \le 31.3$.

At small streamwise distances, the secondary flow regions on either side of the primary core have nearly the same free-stream velocity (i.e. the flow field is approximately symmetric), and the flow decelerates slightly. Close inspection of the results reveals a small fluctuation in flow speed for the more underexpanded cases. It will be shown later that this is caused by a local reduction of the effective secondary flow area.

At longer distances, approximately for $x / H_{e,nozzle} \ge 15$, the flow surrounding the core regains speed once the shear layers reach the wall. Further beyond this point one side always accelerates more than its counterpart. In test case 11 the slower side seems to reach very low velocities before it regains speed (these occurrences are denoted by $M = 0$ in Figure 5.13 and correspond to $P_{pit} / P_s \le 1$). However, because the accuracy of the calculations effectively decreases for $P_{pit} / P_s \sim 1$, it is difficult to determine with certainty the flow speed at these locations. However, it has been suggested that for low entrainment ratios the flow near the wall may separate, stagnate or recirculate when the shear layers reach the mixing-tube wall (Hickman et al. 1972).

In Sections 4.3.3.1 and 4.3.3.2 it was explained that, in all test cases, one shear layer always reaches the wall first. In test case 1 the upper shear layer reached the wall first in traverses made at $x / H_{e,nozzle} \leq 15$, while the opposite is true for traverses made at longer distances. It is unclear what caused this shift, although it appears to be related to the streamwise position of the probe.

The results suggest that the shear layer which first reaches the wall in essence trips the entire flow field, causing it to lean to that side of the mixing tube. This phenomenon can be seen in the Schlieren photographs. Others also have reported asymmetry of the flow at the mixing tube exit, although no explanation has been provided for the skewness. In his study of an axisymmetric ejector, Quinn (1976) observed that the flow at the exit of the mixing tube was asymmetric, in spite of many attempts to align the primary nozzle with the cylindrical mixing tube.

5.3 Shear-Layer Growth Rates and Development

It is stated earlier that ejector performance depends to a large extent on how rapidly and efficiently the primary and secondary streams mix and exchange momentum. The spreading rates of the shear layer and its boundaries provide a measure of where the mixing process occurs in the flow field. One objective of this investigation is to compare the shear layer development among the different levels of primary underexpansion.

5.3.1 Growth Rates for the Ideally Expanded Test Case

The *near field* growth rates for the upper and lower shear layers in the *baseline* test case were calculated from measurements of the local shear-layer thickness. The thickness was found from pitot-pressure measurements using a widely accepted definition of thickness based on the local maximum and minimum pitot pressures (Figure 4.8). According to this definition, the inner and outer edges of the shear layer correspond to the transverse locations where pitot pressure is equal to

$$P_{pit,\,95\%}(x) = P_{pit,\,min}(x) + 0.95\left(P_{pit,\,max}(x) - P_{pit,\,min}(x)\right) \tag{5.1a}$$

and

$$P_{pit,\,5\%}(x) = P_{pit,\,min}(x) + 0.05\left(P_{pit,\,max}(x) - P_{pit,\,min}(x)\right), \tag{5.1b}$$

respectively. The coordinates for the inner and outer edges are denoted by $y_{95\%}(x)$ and $y_{5\%}(x)$ respectively. The local shear layer thickness based on pitot-pressure measurements is defined as

$$\delta_{pit}(x) = \left|y_{95\%}(x) - y_{5\%}(x)\right|, \tag{5.1c}$$

and the shear-layer growth rate is given by

$$\delta'_{pit} = \frac{d}{dx}\delta_{pit}(x) \tag{5.1d}$$

In a few traverses, the values of $P_{pit,\,5\%}(x)$ and $P_{pit,\,95\%}(x)$ were found at more than one location. It was determined that the extreme occurrences clearly do not fit within the expected behavior. Hence the calculations were based on the innermost occurrence of $P_{pit,\,5\%}(x)$ and the outermost occurrence of $P_{pit,\,95\%}(x)$ relative to $y = 0$. Each shear layer was found using the corresponding side of the traverses.

The data used to calculate growth rates had to meet two criteria. First, only traverses within the flow region that extends to the end of the primary core were considered (i.e. traverses in the region between x_0 and x_1 in Figure 1.1). Inspection of the Schlieren image on Figure 4.1(a) reveals that the primary core in test case 1 ends at a streamwise distance of approximately x = 15 cm ($x / H_{e,\,nozzle} = 11.9$). This compares well with the location where $P_{pit,\,min}$ begins decreasing rapidly, relative to the values observed upstream in the core (Figure 4.11).

Secondly, only data from the fully developed region were considered in the calculations. The shear layers are considered fully developed once they exhibit a visible thickening in the streamwise direction, and when the pressure profiles across the layers become self-similar irrespective of streamwise position. To find the location where the flow becomes self-similar, the traverse data were normalized using the local thickness $\delta_{pit}(x)$ and the pressure difference across the layer $P_{pit,\,95\%}(x) - P_{pit,\,5\%}(x)$, as the normalization parameters. Hence the traverse for a given streamwise distance x is represented by

$$\eta(x) = \pm\frac{y(x) - y_{95\%}(x)}{y_{5\%}(x) - y_{95\%}(x)} \quad \text{and} \quad \pi = \frac{P_{pit}(x,y) - P_{pit,\,5\%}(x)}{P_{pit,\,95\%}(x) - P_{pit,\,5\%}(x)} \qquad (5.2)$$

The plus and minus signs correspond to the positive and negative sides of the traverse, respectively. Each side was normalized using the corresponding inner and outer quantities.

The normalized traverses are shown in Figure 5.14 for streamwise distances in the range $0 \le x / H_{e,\,nozzle} \le 20.6$. According to the definitions used, the local inner and outer edges of the shear layer correspond to $\eta(x) = 0$ and $\eta(x) = \pm 1$, respectively. The results show that the *near field* shear layers become self-similar at a relatively short distance. On the positive side of the flow field, similarity can first be observed at $x / H_{e,\,nozzle} = 1.58$

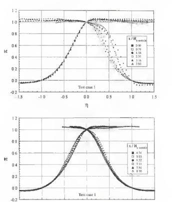

Figure 5.14 Pitot pressure traverses for test case 1, normalized using similarity parameters

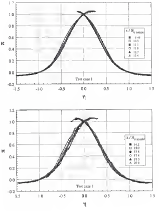

Figure 5.14 (continued)

approximately. The shear layer on the negative seems self-similar even at $x = 0$. This surprising result can be attributed to several factors.

Although every effort was made to build identical nozzle blocks, the trailing edges of the nozzles are slightly different. On the upper nozzle block there is a very subtle bump across the tip on the secondary side. Further, the trailing edge in the upper nozzle is slightly thicker (approximately 0.13 mm). Consequently, the wake flow must be more significant behind the top trailing edge, which in turn is expected to delay the development of the top shear layer. In addition, the flow entering the mixing tube is not perfectly symmetrical, as shown by the traverses made at $x = 0$ (Figure 4.9).

The shape of the normalized profiles remains remarkably constant once self-similarity is reached. Small deviations from the average profile are observed towards the center ($|\eta| \leq 0.7$) where the profiles become wider and narrower in a pattern which is repeated in the streamwise direction. Results presented in Section 5.3.3 show that this variation occurs mainly in the supersonic region of the shear layer, and is most likely caused by the waves in the primary core. Self-similarity of the profiles is highest towards the outer flow region ($|\eta| \geq 0.7$), where the flow is not directly influenced by the waves.

The waves in the core may also lead to the trend reversal observed on the positive side for the traverses made at $x / H_{c\,nozzle} = 0.79$, 1.58 and 2.37 (Figure 5.14). The traverse at $x / H_{c\,nozzle} = 2.37$ is not self-similar and its shape is almost identical to the one at $x / H_{c\,nozzle} = 0.79$ while the traverse at $x / H_{c\,nozzle} = 1.58$ is approximately self-similar. These three positions ($x = 1$ cm, 2 cm and 3 cm, Figure 4.1) are in consecutive fields of the wave structure. The first and third positions are nearly one complete wave cycle apart and lie on the upstream and downstream sides of a wave reflection, respectively. Therefore, the free-stream properties at these locations are similar.

Figure 5.14 also shows that the shape of the self-similarity profile remains approximately unchanged far beyond the end of the primary core, and past the end of the core and the point where the shear layers reach the walls. The similarity profile is still preserved at $x / H_{e\,\mathrm{nozzle}} = 20$ (where $M_{y=0} = 1.4$) well beyond the end of the primary core and the point where the shear layers reach the wall. This result is surprising and contrary to expectation (see for example Hill, 1965). As the free-streams become completely entrained by the shear layers, it seems reasonable that a different similarity profile would develop.

The shear-layer edges for the *baseline* test case defined by Equations 5.1a and 5.1b are shown in Figure 5.15. Both shear layers are approximately symmetric with respect to the "true" center of the flow, in agreement with the flow visualization and the traverse measurements. The apparent offset of the flow field towards the negative side is attributed to a systematic error in the position of the probe (as discussed in Section 4.3.2). The plot shows that both shear layers begin to grow at $x / H_{e\,\mathrm{nozzle}} = 1.58$.

The local thickness of the shear layers is plotted in Figure 5.16. This figure confirms that both layers begin to grow at $x / H_{e\,\mathrm{nozzle}} = 1.58$, approximately. Benjamin (1994) investigated a similar flow using the same test section and found that the flow at this location meets Bradshaw's criteria for fully developed turbulent shear layers. Figures 5.15 and 5.16 show that the thickness found for the positive side at $x / H_{e\,\mathrm{nozzle}} = 2.37$ does not fit well with the adjacent data points. This result can be expected given that at this location the positive side of the traverse is not self-similar (Figure 5.14). For this reason, this measurement was omitted from the calculations. The solid symbols in Figure 5.16 correspond to the points

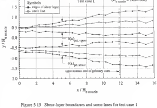

Figure 5 15 Shear-layer boundaries and sonic lines for test case 1

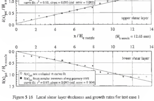

Figure 5 16 Local shear layer thickness and growth rates for test case 1 used to compute the growth rates. The linear curve fits through the solid symbols are given in the figure.

From the curve fits it is found that the *near-field* growth rates for test case 1 are $\delta'_{pit} = 0.092$ for the upper layer and $\delta'_{pit} = 0.095$ for the lower layer (or an average of $\delta'_{pit} = 0.094$). The high correlation factors and the small standard errors show that a constant spread rate is a good model for the ejector shear layers in this region of the flow. It should be noted that, if the distance to fully developed conditions was underestimated, the error in the computed growth rate is small because the results do not change much (less than 10%) by excluding from the calculations additional measurements near the inlet plane.

Figure 5.17 compares the growth rate for test case 1 with measurements obtained in several investigations of compressible shear layers. The data have been normalized by the theoretical growth rate for an incompressible ($M \to 0$) constant pressure shear layer having the same velocity and density ratios (Equation 2.12). As discussed in Chapter 2, the data normalized in this fashion is only a function of convective Mach number (Equation 2.21). For the flow conditions of test case 1 (i.e. $M_{c1} = 0.595$, $V_2 / V_1 = 0.248$ and $\rho_2 / \rho_1 = 0.611$), Equations 2.12 and 2.20 yield $\delta'_0 = 0.157$ and $\delta' / \delta'_0 = 0.50$ (the experimental value of the latter is $\delta'_{pit} / \delta'_0 = 0.60$). Hence, it follows that for a constant-pressure shear layer similar to those in test case 1 the predicted growth rate is $\delta' = 0.080$.

Benjamin (1994) investigated an air/air flow for which $M_1 = 1.78$ and $M_2 = 0.30$ using the same test section used in this investigation, but for test-section pressures three times higher. The predicted growth rate for these flow conditions (i.e. $M_{c1} = 0.62$, $V_2 / V_1 = 0.214$ and $\rho_2 / \rho_1 = 0.623$) is $\delta' = 0.082$ (or $\delta' / \delta'_0 = 0.48$). Benjamin found an average growth rate of $\delta'_{pit} = 0.080$. The small differences in test conditions are expected to

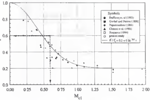

Figure 5.17 Normalized shear-layer growth rates for two-dimensional ejector shear layers and constant-pressure mixing layers

result in different growth rates, however, the difference between the two results is more than anticipated.

The growth rate obtained for test case 1 seems high (13%) when compared to those reported for constant pressure mixing layers and even ejector shear layers. This apparent discrepancy can be attributed to several factors.

In most planar, mixing-layers studies the static pressure remains nearly constant in the flow direction, whereas in ejector flows the pressure always increases. Also, the primary free stream velocity varies considerably more in ejector flows, where the core velocity always decreases some in the flow direction. In essence, the boundary conditions for ejector shear layers are different and are expected to result in higher growth rates. The higher growth rate can also be attributed to the waves originated inside the nozzle. Papamoschou (1986) found that growth rates can increase by up to 25% when waves are present in the flow. Papamoschou also found that a 5% reduction in growth rate is conceivable if the pressure distribution is near ideal (i.e., constant pressure).

Close inspection of the results revealed that the apparent discrepancies with Benjamin's measurements can be traced to the method of calculation. The positive-side of the two most upstream traverses used by Benjamin to compute growth rates do not meet the self similarity requirement imposed here. Further, the length of the primary core may have been underestimated by using as a guideline the convergence of the inner shear layer edges found from the pressure traverses. As a result, some data for the region of interest may have been excluded from Benjamin's calculations. The same is true for the ejector shear layer measurements reported by this author and his coworkers (1993).

Growth rates can differ by up to 11%, depending on which data are included for the calculations. Results as low as $\delta'_{pit} = 0.085$ were obtained by assuming a shorter primary core and by including the data for $x / H_{e,nozzle} = 2.37$ on the positive side. However, the approach used here to estimate the length of the primary core is believed to provide better accuracy. This is supported by Benjamin's visual measurements of local thickness from Schlieren photographs which resulted in $\delta'_{vis} = 0.11$.

Due to the sensitivity of the results to the particular apparatus, test conditions, and the data and criteria used in the calculations, no attempts were made here to examine the virtual origin of the shear layers.

The accuracy of growth rates obtained from pitot pressure measurements has been reported as ±10%, approximately (Papamoschou, 1986). Hence, it can be concluded that within experimental uncertainty the *near-field* shear layers for the *baseline* case develop at a rate similar to that of constant-pressure mixing layers.

5.3.2 Shear Layer Development for the Underexpanded Test Cases

Measuring the growth of the shear layers in the underexpanded flows is less trivial. The primary difficulty is finding the inner edge of the shear layer from the test measurements. The waves present in these flows result in transverse gradients which affect the local free-stream properties of the primary, unlike in the ideally expanded case, where properties are nearly constant across the primary. The magnitude of these gradients is directly related to the strength of the waves (Section 4.2.2) and is considerable for the highly underexpanded cases. Further, the waves penetrate the shear layers and, consequently, they also affect the flow properties inside the layers.

The wavy or lobed shape of the underexpanded primary core represents an additional complication. The Schlieren images (Figures 4 2 through 4 6) clearly show that the shear layers adopt this wavy shape in contrast to the perfectly expanded case for which the layers are approximately uniform. In the ideal inviscid case the boundary of the underexpanded primary core (i e the inner edge) can be predicted from a knowledge of the flow conditions. The predicted boundary would resemble the representation in Figure 4 7 However the inviscid predictions depart significantly from the real flow except at very short distances from the primary exit plane.

The available numerical solutions which take into account turbulence and nonideal viscous effects (Dash et al , 1985 Seiner et al 1985 Tam et al., 1985 for example) are limited to free jets (constant surrounding pressure) The accuracy of these algorithms is limited by the inability of the turbulent models to represent the turbulent structures over the full range of conditions particularly in jets dominated by acoustic interactions of screech tones Further the available data suggests that accuracy declines with increasing distance from the jet axis

Due to the flow complexities, the pressure traverses are insufficient to find accurately the inner edge of the shear layers in the underexpanded cases In addition, the shear layer definition used for the *baseline* test case is unsuitable for these flow cases. Such definition relies on a monotonic variation of pitot pressure across the layer and near uniform free stream pitot pressures

An alternate approach to examine the development of ejector shear layers is to determine the growth of the *plume* of the ejector flow field (defined in Section 4 3 3 1) By definition the boundaries of the *plume* correspond to the outer edges of the shear layers. In all test cases the *plume* boundaries can be found from the pressure traverses for the flow near these boundaries is subsonic and, therefore, is not directly affected by the waves in the core.

The *plume* boundaries can be defined in a manner analogous to the traditional shear-layer definition (Equations 5.1a, 5.1b and 5.1c), but using only the secondary free-stream properties. Thus the *plume* boundaries are defined here as the transverse distances at which pitot pressure is equal to

$$P_{pit,\,15\%}(x) = 1.15\,P_{pit,\,min}(x) \tag{5.3a}$$

The coordinates for these boundaries are denoted by $y_{15\%}(x)$. The local width of the *plume* and the *plume* growth rate are given by

$$\omega_{pit}(x) = y_{15\%}(x)\big|_{pos.\ side} - y_{15\%}(x)\big|_{neg.\ side} \tag{5.3b}$$

and

$$\omega'_{pit} = \frac{d}{dx}\omega_{pit}(x), \tag{5.3c}$$

respectively. The criterion chosen (i.e. 15% above free-stream) is somewhat arbitrary, yet it provides good agreement with the conventional shear layer definition. Further, because pitot-pressure gradients are very steep in the shear layer, different criteria result in almost identical boundaries.

Figure 5.18 shows the streamwise variation of the *plume* width in the *near-field*. For the *baseline* case, the local width was also computed using $y_{5\%}(x)$ instead of $y_{15\%}(x)$. The results show that there is excellent agreement between the *plume* boundaries proposed here (Equation 5.3a) and those found using the more traditional outer-edge definition (Equation 5.1b).

The streamwise variation of the *plume* reflects clearly the level of primary underexpansion in each flow field. In the *baseline* case the *plume* boundaries are nearly

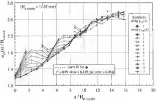

Figure 5.18 *Near field* variation of *plume* width

straight, while in the underexpanded flows the *plume* widens and narrows in a repetitive manner due to the wavy shape of the shear layers. This behavior is observed clearly from the Schlieren images. The *plume* boundaries could not be determined everywhere for the highly underexpanded cases. As explained earlier, pressure traverses were not obtained at a few locations in these cases due to probe-induced choking.

At short streamwise distances, there are substantial differences in $\omega_{pl}(x)$ among the flow cases. In the highly underexpanded cases the *plume* reaches far into the secondary, in essence reducing the effective flow area of the secondary free stream. As a result, the local free-stream velocity increases and the pressure decreases (explaining the results of Sections 4.4.2 and 5.2).

At longer distances, however, the width of the *plume* is remarkably similar in all cases. Contrary to expectation, the large distortions of the outer edges observed initially in the underexpanded flows seem to have very little effect on the average outward development of the shear layers and the average net growth of the *plume*. This result is in agreement with observation that the shear layers in all cases seem to reach the wall at approximately the same streamwise distance (Section 4.3.3).

The *plume* growth rate computed for the *baseline* case is $\omega'_{pl} = 0.12$. In essence, this growth rate is twice the average shear-layer growth in the direction of the secondary. Thus, by comparing this result with the actual shear-layer growth rate (i.e. $\delta'_{pk} = 0.094$), it can be concluded that the shear layers lean towards the outward direction.

5.3.3 Sonic Lines of the Shear Layers

In addition to the *plume* boundaries, the boundaries of the supersonic core or sonic lines (Figure 1.1) can also be used in supersonic/subsonic flows to characterize compressible shear layers. The sonic lines represent the boundaries beyond which the shock-cell system in the underexpanded jet cannot extend, and where the apparent acoustic sources are located (Pao and Seiner, 1983). It appears that these boundaries have not been studied in detail experimentally, particularly in bounded jets or ejector flow fields.

The sonic lines are defined by the critical pressure ratio $(P_{pt} / P_s)_{cr} = 1.893$. Hence, the points on either side of the traverses where this condition is met were found using measurements of pitot-pressure and side-wall pressure. For calculation purposes, it was assumed that side wall pressure is approximately constant in the transverse direction outside the supersonic core. More specifically, it was assumed that $P_s(x,y) \approx P_s(x,y = \pm 19.2 \text{ mm})$ wherever $M \le 1$. This approximation will be examined in detail in the following section.

In computing P_{pt} / P_s, the side-wall pressures at $y = +19.2$ mm and $y = -19.2$ mm were used for the positive and negative sides of the traverse, respectively. Since the spacing between the off-center pressure taps is twice the spacing between traverses, the side-wall measurements were averaged for calculations at the intermediate positions. This approach is within the accuracy of the constant pressure assumption, and is justified because the off-center pressure varies continuously and monotonically (Section 4.4.2). The traverse points for which the ratio P_{pt} / P_s more closely matches the critical pressure ratio were then found. The traverse data were not interpolated which led to no measurable loss of accuracy given that the spacing between traverse points is only 0.13 mm.

The sonic lines are shown in Figure 5.19 for all test cases. The shear layers for the *baseline* case are also shown for comparison. In all cases the sonic lines originate at approximately the same transverse distance, near the outer edge of the shear layers, and follow the shape of the shear layers closely. In the *baseline* case the sonic lines are nearly

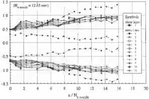

Figure 5.19 Comparison of sonic lines in the *near field*

straight while in the underexpanded flows they have a wavy or lobed appearance. In the underexpanded flows the sonic lines clearly mark the position of the first two or three shock cells in the primary core. At the end of each shock cell, the sonic lines turn inwards, moving closer to those for the ideally expanded flow. The results agree qualitatively with predictions for an underexpanded free jet (Dash et al., 1985).

The sonic lines for test cases 1 through 5 seem to converge near $x / H_{e\ nozzle} = 4$, and to a lesser extent near $x / H_{e\ nozzle} = 8$. This trend is very clear in Figure 5.18. In the remaining cases there is a noticeable departure from this pattern. These observations seem to correlate with those made from the sound measurements. Namely, it was found that screech was detected predominantly in the initial region of the mixing tube ($2.01 \leq x / H_{e\ nozzle} \leq 8.33$). Further, screech intensity was found to increase with primary underexpansion up to test case 5 (i.e. $P_{s,1} / P_{s,2} = 1.28$, $P_{0,1} / P_{s,1} = 7.35$, and $\dot{m}_2 / \dot{m}_1 = 0.133$), and then decrease for the remaining cases. Davies and Oldfield (1962a) found a similar correlation between the shock-cell structure and the screech emissions in an axisymmetric free jet.

In cases 4 through 11 the expansions in the first two shock cells are sufficiently strong to move the sonic lines beyond the location of outer edges in the *baseline* case. At longer distances ($x / H_{e\ nozzle} \geq 12$), however, the sonic lines are grouped together like the *plume* boundaries. This result provides additional evidence that, on average, the outward *near field* development of the shear layers is similar in all cases.

An interesting result was obtained by normalizing the sonic-line coordinates for the ideally expanded case according to Equation 5.2. The results which are plotted in Figure 5.20 show that the supersonic region of the shear layer shrinks somewhat with increasing distance as the sonic line moves towards the inner edge of the shear layer (i.e. closer to $\eta = 0$). On average, the distance to the inner edge decreases from $\eta_{M=1} = \pm 0.68$ at $x / H_{e,nozzle} = 1.58$ to $\eta_{M=1} = \pm 0.56$ at $x / H_{e,nozzle} = 15.8$. Inspection of Figure 5.3 shows that in the same region the Mach number at the center of the core decreases by 17%.

While these results are not surprising, they explicitly show that the extent of the supersonic region in the shear layers is related to the local free-stream Mach number in the core, $M_{\infty,1}(x)$. Strictly speaking, the extent of this region most likely depends on other variables, such as the Mach number of the secondary free stream. For example, the equation for the sonic line may be expressed as

$$\eta_{M=1}(x) = F\left\{M_{\infty,1},\ M_{\infty,2},\ V_2/V_1,\ \rho_2/\rho_1,\ \gamma_1/\gamma_2\right\} \tag{5.4a}$$

where V, ρ, and γ are velocity, density, and specific heat ratio, respectively. It is plausible that $\eta_{M=1}$ is a function of the convective Mach number, M_c, rather than the actual Mach numbers of the free streams (as appears to be the case for compressible shear layer growth rates, Equation 2.19). By definition, the function F must meet at least the conditions

$$\begin{aligned} \eta_{M=1}(x) &= 0 \quad \text{for} \quad M_{\infty,1}(x) = 1,\ M_{\infty,2}(x) < 1 \\ \eta_{M=1}(x) &\to 1 \quad \text{for} \quad M_{\infty,1}(x) \to \infty,\ M_{\infty,2}(x) < 1 \end{aligned} \tag{5.4b}$$

Figure 5.21 shows the sonic line normalized position, $\eta_{M=1}$, plotted against Mach number for the *baseline* test case (i.e. ideally expanded air/air, $M_1 = 1.80$, $M_2 = 0.35$, $P_{t,1} = P_{t,2} = 34.5$ kPa). As could be expected, the figure clearly shows that a greater portion of the shear layer is subsonic (i.e. $\eta_{M=1} \to 1$) as the Mach number of the core, $M_{\infty,1}(x)$, decreases. This type of data can be used to determine empirically the form of Equation 5.4a, or to confirm analytical models. However, a comprehensive database would be required to accomplish such undertaking.

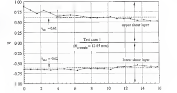

Figure 5.20 Sonic line for test case 1, normalized using similarity parameters

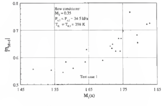

Figure 5.21 Sonic-line variation with core Mach number for test case 1

The results in Figure 5.20 also demonstrate that the cyclic variation observed near the center of the similarity profiles ($|\eta| \leq 0.7$, Figure 5.14) is caused by the waves in the supersonic core, for these waves do not occur in the subsonic region (i.e. $|\eta| \geq 0.7$). Further, this result demonstrates that it is unlikely that self-similarity can exist in the underexpanded flows where waves of significant strength are present (in support of the claim that the traditional shear-layer definition is not suitable for these flows).

5.3.4 Variation of Static Pressure Across the Flow Field

In Chapter 4 it is claimed that static pressure varies primarily in the streamwise and transverse direction, and also that the transverse gradients are confined primarily to the supersonic core. Later in this section it will be argued that pressure is approximately constant in the spanwise direction (i.e. z direction).

The assumption that transverse pressure gradients are relatively small outside the primary core can be argued as follows. In internal flows such as those considered here, static pressure varies across the flow because compression and/or expansion waves are present or because the streamlines are curved. The Schlieren images show that compression and/or expansion waves are present in all cases. However, these waves are confined to regions where $M \geq 1$. Hence, the first scenario directly supports the proposed assumption.

The test results provide no evidence of any significant streamline curvature in the *baseline* flow case. However, in the *near-field* of the underexpanded flows, the streamlines in the shear layers are curved due to the wavy shape of the layer. The curvature increases with primary underexpansion and is most pronounced at short streamwise distances (as shown by the *plume* boundaries and sonic line results). Consequently, transverse pressure gradients must exist outside the supersonic core in the underexpanded flows.

Some insight about the effect of streamline curvature on pressure can be derived from the classic solution for inviscid, subsonic flow past a wave-shaped wall (Shapiro 1953). The pressure coefficient, C_p, at any point (x,y) in a flow over a wall shaped as a cosine function is given by the expression

$$C_p = -\frac{4\pi}{\sqrt{1-M_\infty^2}}\frac{h}{\ell}\cos\left(\frac{2\pi x}{\ell}\right)e^{-2\pi\sqrt{1-M_\infty^2}\,(y/\ell)} \qquad (M_\infty < 1) \qquad (5.5)$$

In this expression M_∞ is the free-stream Mach number, and h and ℓ are the amplitude and wavelength of the wall shape, respectively The pressure coefficient also takes the usual form

$$C_p = \frac{P_s/P_{s,\infty} - 1}{\frac{1}{2}\gamma M_\infty^2} \qquad (5.6)$$

The wavy wall model was obtained for a semi-infinite inviscid flow field where the free stream Mach number (M_∞) is constant However, it is possible to assume that (a) the Mach number variation of the secondary and the wall effects are small and (b) the shear-layer and its boundaries have a shape similar to a cosine function (a reasonable assumption based on the Schlieren images) Then Equations 5.5 and 5.6 can give a first-order estimate of the pressure variation near the edges of the shear layers

The highest streamline curvature occurs in test case 11 Visual inspection of Figure 4.6(a) shows that, in the region of the first shock-cell, the outer edge of the top shear layer can be approximated by a cosine function with 2h = 10 mm and ℓ = 64 mm (with 2h measured from a cord connecting the top trailing edge with the outer edge at $x = \ell$) Using these values and $M_\infty = M_2 = 0.35$ Equations 5.5 and 5.6 give $(P_s - P_{s,\infty})/P_{s,\infty} = \pm 0.09$ at the highest and lowest points of a cosine shape wall Therefore within the approximation of this model the static pressure difference between the outer edge and the adjacent secondary free-stream is no more than 9% anywhere in the *near field* Inspection of the side wall pressure distributions for test case 11 shows that the variations in the off-center measurements are indeed in close agreement with this estimate

Inside the shear layer specifically in the region $y_{5\%}(x) \le y \le y(x)_{M_s=1}$, the Mach number is higher (i.e. $M_\infty \le M(y) \le 1$) Equation 5 5 then predicts larger pressure gradients when applied to a streamline in this region It is easily shown from Equations 5 5 and 5 6 that the maximum transverse pressure gradient in the flow over a cosine-shaped wall is given by

$$\left.\frac{\partial(P_s/P_{s,\infty})}{\partial y}\right|_{max} = \pm 4\pi^2 \frac{h}{\ell^2} \gamma M_\infty^2 \qquad (M_\infty < 1) \qquad (5\ 7)$$

This expression can be rewritten as

$$\left.\frac{\partial(P_s/P_{s,\infty})}{\partial(y/H_{e\ nozzle})}\right|_{max} = \pm 4\pi^2 \frac{h}{\ell} \gamma M_\infty^2 \left(\frac{H_{e\ nozzle}}{\ell}\right) \qquad (M_\infty < 1) \qquad (5\ 8)$$

The plus and minus signs correspond to the peak magnitudes of the cosine function By taking the same values used earlier for h and ℓ and $M_\infty = 0.9$ for example as representative of a streamline near the sonic line, it is found that the maximum pressure gradients near the sonic line for test case 11 are of order

$$\left.\frac{\partial(P_s/P_{s,\infty})}{\partial(y/H_{e\ nozzle})}\right|_{max} = \pm 0\ 69$$

Undoubtedly this result shows that the pressure gradients near the sonic lines are quite large for high underexpansion However these gradients are relatively small in comparison to those measured for pitot pressure Inspection of all traverses in the *near field* and for all test cases shows that pitot pressure gradients are of order

$$3 \le \left| \frac{\partial\left(P_{pit}/P_{s,2sec}\right)}{\partial\left(y/H_{c\ nozzle}\right)} \right| \le 20$$

across the shear layers (i.e. between $y_{95\%}(x)$ and $y_{5\%}(x)$). In the above result, the steepest gradients are for cases of high primary underexpansion and/or for traverses at short streamwise distances (i.e. where streamline curvature is greatest), and the absolute sign is shown to include the gradients on either side of the traverses. After noting that $P_{s,2sec} = P_{s,\infty}$ in the *near field*, it can be concluded, even within the crudeness of the wavy wall approximation, that pitot-pressure gradients in the transverse direction are at least an order of magnitude larger than the corresponding static-pressure gradients. Therefore, the ratio P_{pit} / P_s varies much faster due to changes in P_{pit}. Consequently, $y(x)_{M_s=1}$ (i.e. where $P_{pit} / P_s = 1.893$) depends almost exclusively on P_{pit}, which demonstrate that the constant-pressure assumption leads to relatively small errors in finding the sonic line.

The wavy-wall solution provides additional insight about the pressure in the *near field* of the underexpanded cases. The solution predicts that in regions where the layer moves into the secondary (i.e. in regions of maximum core expansion) the pressure near the outer edge is lower than the free-stream pressure. The trend is reversed when the shear layers bend inwards as the core contracts. This is precisely the behavior observed from the measurements (Section 4.4.2). Also, the solution predicts that the difference in pressure decays exponentially with increasing distance from the outer edge.

Inside the supersonic core, the transverse pressure gradients are similar in magnitude to the changes in centerline side-wall pressure (Section 4.4.1). This is a direct result of the waves inside the core, which are responsible not only for the pressure field but also for the shape and structure of the core (Section 4.2). The transverse gradients in the supersonic core are difficult to predict with sufficient accuracy. The complexity of the flow field coupled with viscous effects and the wave/shear layer interaction, renders such predictions inadequate for the objective of this investigation.

With increasing streamwise distance the wave structure and the streamline curvature are diminished. As a result, the transverse variation of static pressure decreases accordingly, which is clearly shown by the side-wall pressure distributions (Figures 4.24 through 4.34). At $x / H_{e\,nozzle} = 34.5$ the side-wall pressure is nearly constant in the transverse direction.

That pressure is everywhere approximately constant in the spanwise direction, particularly at the mixing-tube exit, can be argued on the following grounds. The dominant gradients in these flow fields (including pressure gradients) arise from

(a) differences between the properties of the primary and secondary streams (i.e. transverse gradients between the center and outer flow regions),

(b) the streamwise development of the flow field as the two streams exchange momentum and interact with the solid boundaries (i.e. streamwise gradients), and

(c) the wave structure in the supersonic core (i.e. streamwise and transverse gradients caused by the waves).

Hence, there is no inherent mechanism which can lead to large pressure gradients in the spanwise direction. The excellent agreement obtained for Mach numbers computed from (a) Mach angles and (b) pitot pressure and side wall pressure measurements (Section 4.2.3) implies that side-wall pressure is indeed representative of the static pressure across the flow in support of the above claim. At the mixing-tube exit, the transverse pressure variation is minimal. Therefore, it is reasonable to conclude that static pressure is also constant in the spanwise direction, and that pressure varies only in the streamwise direction.

5.4 Ejector Performance

To determine the relative benefits obtained from primary underexpansion, the performance computed from the test measurements is compared with the ideal performance predicted for the same flow conditions. Ejector performance is evaluated in terms of the thrust augmentation Φ, the ejector pressure ratio, $P_{0,2}/P_{0,1}$, and the Stagnation Momentum Exchange Effectiveness or SMEE, (Equation 2.28). The ejector entrainment ratio was a secondary independent variable and, therefore, was not used to compare performance.

Different definitions have been used for thrust augmentation. In the present investigation, the thrusts of the ejector and the nozzle are referenced to the inlet pressure of the mixing tube. The thrust augmentation is then given by

$$\Phi = \frac{\text{ejector thrust}}{\text{primary thrust}} = \frac{\int_{A_3} V \rho V \, dA + \int_{A_3} (P - P_2) \, dA}{\int_{A_1} V \rho V \, dA + \int_{A_1} (P - P_2) \, dA} \tag{5.9}$$

where the subscripts 1, 2, and 3 refer to the primary, secondary and mixing tube exits respectively. This choice is somewhat arbitrary but is based on the fact that the secondary pressures are subatmospheric, a different choice will only change the relative magnitude of the computed thrust, but trends will remain unchanged.

The ideal performance was computed using exit properties predicted through a control volume analysis. The "actual" performance was computed using average exit properties obtained from the test data and a model for the velocity profile at the mixing tube exit.

5.4.1 Ideal Ejector Performance

The ideal ejector performance was computed for each flow case from the predicted exit properties. These properties were calculated by applying the conservation equations (continuity, momentum, and energy) to a control volume enclosing the mixing tube. The formulation has been used by other investigators (Addy et al., 1981, and Quinn, 1976, for example) and is described in detail in Appendix C, Section C.4.

Quinn (1976) included in the analysis an empirical friction term and also allowed for flow skewness at the mixing-tube exit by introducing skewness factors into the governing equations (also known as the first, second and third moments). In addition, Quinn's formulation allowed for a nonuniform temperature distribution for cases in which $T_{0,1} \neq T_{0,2}$. His formulation was adapted to flows with fully mixed exit conditions and constant T_0, and was used to obtain performance for each test case, for the following conditions:

(a) no wall friction

(b) with wall friction, $C_f = 0.004$

(c) with wall friction, $C_f = 0.004$ and mixing tube 50% longer (or $C_f = 0.006$)

(d) with wall friction, $C_f = 0.004$ and mixing tube 100% longer (or $C_f = 0.008$)

Above, C_f is the turbulent wall friction coefficient suggested by Quinn (1976). The results are discussed in Section 5.4.4, where they are compared with the actual performance.

5.4.2 Exit Flow Model

The thrust augmentation ratio, the ejector pressure ratio, and the SMEE parameter, all depend on flow properties at the mixing tube exit. In the ejector flow cases considered here (and in most real ejectors flows) the mixing and exchange of momentum and energy between the primary and secondary is never truly complete due to the finite length of the mixing tube As a result, the exit properties are nonuniform, and the performance parameters must be calculated using average properties obtained from integration over the exit cross section

Due to the limited number of measurements obtained at the exit cross section the flow here was modeled to obtain approximate values of the local and average properties The model is based on the available measurements and the following assumptions about the exit flow

(1) static pressure is constant in the spanwise direction (i.e. $P_s(x,y,z)=P_s(x,y)$),

(2) at the exit, compression and/or expansion waves are either absent or very weak,

(3) the flow is symmetric about $z = 0$;

(4) the flow is adiabatic and total temperature is constant (i.e $T_{E,1} = T_{E,2} = T_0 = \text{const}$)

(5) the flow distribution can be approximated by a power function of the form

$$\left.\frac{u(y,z)}{u(y,z=0)}\right|_{exit} = \left(1 - \frac{2|z|}{W}\right)^{\frac{1}{n}} \tag{5 10}$$

where W is the width of the mixing tube, n is an empirical constant and $u(y,z=0)$ is the velocity along the line of the traverse.

The validity of assumptions (1) and (2) was discussed in the previous section Assumption (3) is supported by preliminary measurements made in this investigation and also by the results reported by Benjamin (1994) which show that side-wall pressures are approximately the same on both sides of the mixing tube Assumption (4) is well justified particularly since the variation in total temperature near the wall due to viscous effects is small for $M \leq 2$ (Shapiro, 1954). Lastly, assumption (5) is partly justified by the Reynolds number of the flows considered, after noting that Equation 5.10 provides a good approximation in turbulent flows. Reynolds numbers between $Re_{D_h} = 2.3 \cdot 10^5$ and $Re_{D_h} = 3.4 \cdot 10^5$ were computed, using the velocities predicted for fully mixed exit conditions and the mixing-tube hydraulic diameter.

The representation of the exit velocity is undoubtedly the most arguable part of the model. The mixing tube is relatively short ($L_{MT} / D_h = 12.8$), and the inlet flow is not uniform. Therefore, in all likelihood the flow does not reach a fully developed turbulent condition in the mixing tube. On the other hand, the boundary layers which normally lead to fully developed turbulent flow, are aided in an ejector by the highly turbulent shear layers. Nevertheless, the flow does not need to be fully developed for the model to provide an acceptable representation of the spanwise velocity profile.

Perhaps the largest error associated with the model comes from the fact that the spanwise velocity distribution most likely varies in the transverse direction (i.e. $n \neq$ const. in Equation 5.10). Some variation is likely due to the piecewise nature of the inlet flow and the rectangular cross section of the mixing tube, particularly if the flow is not fully developed.

With all other factors held constant, ejector performance is largely determined by how well momentum is distributed at the mixing-tube exit. In the ejector considered here, momentum is exchanged primarily in the transverse direction. Consequently, the transverse velocity distribution is expected to have the greatest impact on the relative performance for the different flow cases. The spanwise distribution should only have secondary effects on the exit properties and the performance parameters. In support of this view are the results obtained by assuming uniform and logarithmic spanwise profiles, in addition to the power profile The results differ only in magnitude yet follow the same trends Further, Hsia (1984) found that the transverse mixing plays a dominant role on the performance of a two-dimensional ejector with an area ratio much larger than the one considered here

Based on these considerations the model given by Equation 5 10 is considered suitable for the purpose of comparing the relative performance Further, a single value of n was used for each flow case for the entire cross section The value used was found through iteration by requiring that the exit velocity distribution satisfies continuity Using a constant value of n is a convenient simplification, considering that the choices of n(y) that satisfy continuity are unlimited

The calculation procedure is explained in the following section and in Appendix C, Section C.5 Figure C 1 shows the spanwise velocity distributions for selected tests cases and gives the average n values obtained for each flow case based on calculations for three different traverses made at the exit plane For flows with $Re_{D_h} \sim 10^5$ n is known that $n \sim 7$ (Schlichting, 1979 Fox and McDonald, 1978) This value is very close to the those obtained for cases 1 and 2 showing that it is possible that these flows are close to fully developed at the mixing tube exit.

The results for the remaining cases show that these flows do not reach fully developed conditions The Reynolds number is higher, and the difference in primary and secondary inlet conditions increases for higher primary pressures Both of these factors can lead in longer entry lengths As mentioned earlier however this does not imply that the model fails to provide an acceptable representation of the exit flow

In addition to aiding in the computation of the exit properties, Equation 5.10 can be used in the *baseline* test case to examine the velocity distribution in other regions of the mixing tube. This is possible because in this case the flow field is free of strong waves and static pressure is nearly constant in the transverse and spanwise directions, everywhere in the mixing tube. Figure C.2 shows the spanwise velocity distributions obtained for the *baseline* case at selected streamwise distances in the region $0 \leq x / H_{t,\,nozzle} \leq 12.7$. The results help demonstrate that the inlet flow is approximately piecewise uniform and also show that wall friction causes the flow to become increasingly three-dimensional in the streamwise direction.

5.4.3 Calculation of Exit Properties and Actual Ejector Performance

The average exit properties were obtained by integrating numerically the local properties given by the model over the exit cross section. Thus, the exit cross section was divided into a grid of finite area elements having 373 rows and 101 columns, as shown in Figure 5.22. For convenience the grid spacing in the transverse direction is the same as the spacing between the pitot pressure data points ($\Delta y = 0.127$ mm). The two regions not included by the pressure traverse (i.e. the regions adjacent to the top and bottom walls) were subdivided into single rows of area elements. A constant spanwise spacing of $\Delta z = 0.252$ mm was used for the entire cross section. This grid places a pitot-pressure measurement at the center of each area element in the center column (i.e. $j = 2, \ldots, 372$ and $k = 51$, Figure 5.22) with the exception of the two elements outside the traverse (i.e. $j = 1, 373$ and $k = 51$, Figure 5.22).

The calculation of the local and average exit properties is outlined in detail in Appendix C, Section C.5. Basically, it consists of first finding the flow properties for the

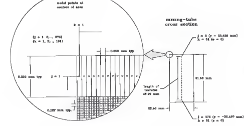

Figure 5.22 Grid used for computation of the average properties at the mixing-tube exit.

elements in the center column based on the local value of $P_{pit} / P_s|_{j,k}$. The properties for the rest of the grid are than found using an assumed velocity distribution (Equation 5.10) and the local value of $P_{s,j,k}$. To this extent, the side-wall pressures measured at the exit plane were interpolated to obtain an approximate value of $P_{s,j,k}$. Interpolation was used primarily for consistency, as side wall pressure is nearly constant at the exit plane in all flow cases.

For the two area elements in the center column but not covered by the traverse (i.e. $j = 1, 373$ and $k = 51$), it was further assumed that they comprise the boundary layers and that the velocity here varies linearly (i.e. $u_{j=1,k} = u_{j=2,k}/2$ and $u_{j=373,k} = u_{j=372,k}/2$). These assumptions certainly oversimplify the nature of the flow near the wall. However computations made using other models showed that these end regions have very little impact on the average exit properties. The properties for these element are found from the static pressure and the assumed local velocities.

Once the properties for the entire grid are available, the total mass flux is computed and compared with the orifice plate measurements. The assumed velocity distribution is updated as necessary (by varying n), and the calculations are repeated until continuity is satisfied within the desired accuracy. The algorithm seems well behaved because the final result is independent of the initial guess and convergence always occurs in less than 10 iterations.

The average exit properties and the performance parameters are computed using the local properties obtained in the final iteration. The exit model and grid were also used to compute the flow skewness or moments for each test case, according to Equations C.23c, C.23d, and C.23e (Appendix C, Section C.4). All the calculations were implemented by a simple computer program run in a PC with a 90 MHz processor.

5.4.4 Ideal and Actual Exit Properties and Performance

Among the properties which directly determine ejector performance are the velocity static pressure, and total pressure at the mixing-tube exit. The average exit static pressure and velocity obtained from the data and the exit flow model are plotted against normalized total primary pressure in Figures 5 23 and 5 24, respectively Also shown in these figures are the control volume predictions for the fully mixed conditions outlined in Section 5 4 1

The curve labeled (a) represents the limiting or maximum performance of the ejector for the range of flow conditions considered here Prediction curves (b) (c) and (d) take into account friction losses (Appendix C, Section C 4) Because these curves are based on fully mixed exit conditions (i.e for unusually high velocities near the wall), they represent "the worst of the optimum" ejector output. However, the empirical friction term used to find these curves is not only approximate but it also depends on the friction coefficient, C_f Therefore, these curves provide relative performance and are used primarily to demonstrate the effects of friction and mixing-tube length

The effects of wall friction and incomplete mixing are evident from Figure 5 23 and 5.24 As expected the average exit properties never reach the levels predicted for the fully mixed frictionless case Further the difference between the average exit properties and the predictions of curve (a) becomes larger as the primary pressure is increased. For higher primary flow rates there is a larger momentum difference between the primary and secondary Hence, in general a longer mixing length is required to obtain a given level of mixing. In addition, friction losses increase with primary underexpansion because in some regions the velocities are higher than in the ideally expanded flow (for example, where the primary core is fully expanded and towards the end of the mixing tube)

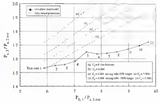

Figure 5.23 Average exit static pressure versus normalized total primary pressure

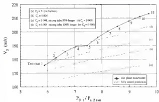

Figure 5.24 Average exit velocity versus normalized total primary pressure

fully mixed frictionless case. Further, the difference between the average exit properties and the predictions of curve (a) becomes larger as the primary pressure is increased. For higher primary flow rates there is a larger momentum difference between the primary and secondary. Hence, in general, a longer mixing length is required to obtain a given level of mixing. In addition, friction losses increase with primary underexpansion because in some regions the velocities are higher than in the ideally expanded flow (for example, where the primary core is fully expanded, and towards the end of the mixing tube).

Most striking about the results in Figures 5.23 and 5.24 is the departure from the general trend observed for test case 5, and to a lesser degree for cases 4 and 6. The exit properties for case 5 are closer to the predicted values than would be expected. In this flow case a larger portion of the total available momentum is retained by the pressure term. Close inspection of the side wall pressure distributions reveals that the mixing process is somewhat accelerated in test case 5. Figure 5.25 shows the average side wall pressure distribution for the off-center measurements, in the region $x / H_{e,\mathrm{nozzle}} \geq 20$. The off-center pressures are a good indicator of the average pressure in the flow field (Section 4.4).

As expected, Figure 5.25 shows that the average streamwise pressure gradient (i.e. the slope of the pressure distribution) increases with primary underexpansion. However, in cases 4 and 5 the onset of the streamwise pressure rise occurs earlier in the mixing tube. Because of this anomaly, the pressure for case 5 is higher than for other more underexpanded cases except at the end of the mixing tube. For example, the pressure in test cases 6 and 7 is lower than for case 5 up to nearly the end of the mixing tube ($x / H_{e,\mathrm{nozzle}} = 30$). Quinn (1976) obtained similar results using an axisymmetric ejector with a convergent nozzle and an area ratio $A_3/A_1 = 25.8$, although the effect was more pronounced in his experiments.

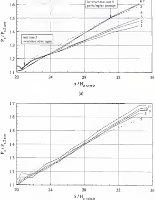

(a)

(b)

Figure 5.25 Average off-center side wall pressure distribution for test cases (a) 1 through 7 and (b) 5, and 8 through 11

The sound measurements showed that flow case 5 generates the strongest screech emissions. Hsia, 1984, reported a similar correlation between screech levels and the skewness of the exit flow.

Figure 5.24 also shows the tradeoff between the extent of mixing and the friction losses, which is well-known to ejector designers. For example, mixing is more complete when the length of the mixing tube is doubled; however, friction losses are higher. Therefore, based on the assumed friction coefficient ($C_f \approx 0.004$), the longer mixing tube does not provide any benefits from better mixing except for test cases 6 and higher. Further, such benefits may be overshadowed by the increase in weight and size of the hardware, depending on the particular application of the ejector. Similarly, a 50% increase in length is not expected to improve performance in the *baseline* flow case.

The total exit pressure, $P_{0,3}$, is plotted in Figure 5.27, in terms of the ejector pressure ratio ($P_{0,3} / P_{0,2}$), against (a) normalized total primary pressure and (b) entrainment ratio. In all cases the actual performance parallels the fully mixed predictions. This shows that although friction increases locally, the total losses remain in proportion to the total available momentum. The total exit pressures are in closest agreement with curve (d). Hence, a mixing tube 50% longer is likely to allow for more complete mixing and increase the total exit pressure, while resulting in moderate friction losses.

The anomaly or "hump" observed in Figure 5.23 and 5.24 for case 5 is also displayed to a lesser extent by the ejector pressure ratio, indicating that $P_{0,3}$ is somewhat higher than expected. However, the benefits of primary underexpansion and acoustic interactions are less evident. One possible explanation is that, because of the relatively low entrainment ratios considered here, the primary stream dominates the flow field and the ejector output.

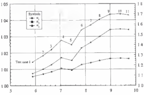

Figure 5.26 Skewness factors for the flow at the mixing-tube exit.

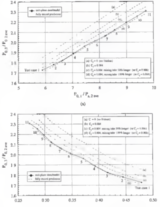

Figure 5.27 Average ejector pressure ratio versus
(a) normalized total primary pressure
(b) entrainment ratio

Hence the improvement to case 5 is overshadowed by the other factors such as friction losses which occur towards the end of the mixing tube as a result of higher velocities. Yet another explanation is that faster mixing also leads to high velocities over a larger section of the mixing tube. This in turn results in additional friction losses which partially counteracts the benefits obtained from more complete mixing. Under this scenario test case 5 may yield better performance with a slightly shorter mixing tube

The ejector thrust augmentation, Φ, is plotted against entrainment ratio in Figure 5 28. The results are similar to those for total exit pressure in that actual performance follows closely the trend predicted However, unlike the other parameter discussed to this point, Φ is in closer agreement with the predictions of curve (c) This result suggests that Φ is less likely to increase by using a longer mixing tube Figure 5.27 also reflects a small improvement for case 5 relative to the rest of the flow cases The small augmentation obtained in these ejector flows is a clear reflection of the low entrainment ratios investigated. For the range of conditions the ejector behaves more like a pump than a thrust augmenter

Lastly, Figure 5 29 shows the Stagnation Momentum Exchange Effectiveness (SMEE) plotted against entrainment ratio for all cases For a given entrainment ratio, primary and secondary gases, and inlet flow conditions (i.e $P_{0,1}$ $P_{0,2}$, $T_{0,1}$, and $T_{0,2}$), SMEE depends only on the total exit pressure Therefore, the results for SMEE are similar to those obtained for the total pressure ratio There is a distinct "bump" on the SMEE curve centered around case 5 which indicates a slightly better performance for that level of primary underexpansion.

The results show that there is a moderate to small improvement in performance for test case 5 The higher performance is attributed to an earlier onset of the mixing process

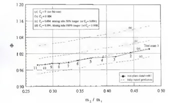

Figure 5.28 Thrust augmentation versus entrainment ratio

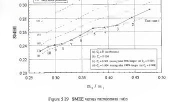

Figure 5.29 SMEE versus entrainment ratio

and correlates well with the occurrence of intense flow-generated screech. Perhaps this early development is triggered by a different distribution and/or different scale of turbulence in the shear layer changes (as suggested to be the case by Quinn, 1976).

It would be premature to characterize the benefits as too small to be practical, for the flows considered here may not reveal the full potential of inducing acoustic interactions. The flow conditions were chosen primarily to isolate the effect of underexpansion on the shear layers in the *near field* and for this the secondary flow conditions were kept constant. This was done by varying the downstream losses in the ejector (by opening and closing the exhaust butterfly valve). In doing this, the ability of each individual primary flow to entrain a given amount of secondary was somewhat suppressed, which is evidenced by the low thrust augmentation and the high exit-to-inlet static-pressure ratios. Therefore, the effects observed pertain only to the primary's ability to mix with the fixed amount of secondary.

5.5 Summary of Effects of Primary Underexpansion

The measurements obtained in this investigation have shown that the flow field of a supersonic primary ($M_1 = 1.80$) subsonic-secondary ($M_2 = 0.35$) ejector can undergo considerable changes when the primary jet is underexpanded (exit static pressure ratios in the range $1.0 \le P_{s,1} / P_{s,2} \le 1.7$). These changes affect both the mean as well as the time varying turbulent flow properties. Collectively, these changes not only affect the nature of the flow field but can also lead to more efficient mixing processes, which in turn can lead to better ejector performance. The following sections provide a summary of the main effects of primary underexpansion, and explain how these effects appear to interact to influence the ejector flow field and performance.

5.5.1 Effect of Primary Underexpansion on Flow Field Development

Most notably among all effects of primary underexpansion is that it changes the shape of the flow field, particularly in the *near field*, as a result of the adjustment of the primary jet to the surrounding local pressure conditions. Inherent to the adjustment of the underexpanded jet is the occurrence of a quasi-periodic system of pressure waves (Figures 4.1 through 4.6), which exists in the supersonic core for as long as there is a significant local static-pressure imbalance between the jet and the surrounding flow. This pressure imbalance diminishes in the streamwise direction (Figures 4.25 through 4.34), primarily as a result of the mixing and exhange of momentum between the primary and secondary streams, but also due to viscous dissipation.

As the pressure imbalance diminishes, so does the wave system in the supersonic core. Unlike in an underexpanded free jet, in which the pressure in the core gradually adjusts to a constant surrounding pressure, in the ejector the pressure of the underexpanded primary core must adjust to a surrounding pressure which gradually increases in the streamwise direction (Figures 4.24 through 4.34).

Directly linked to the adjustment of the underexpanded jet is the streamwise variation of (a) the core's cross sectional dimension and (b) the core flow properties. The core expands and contracts in a periodic-like fashion. Similarly, the core velocity increases and decreases (Figures 5.3 through 5.13) as the static pressure varies in opposite fashion (Figures 4.24 through 4.34).

The changes experienced by the supersonic core in the *near field* have a direct impact, not only on the shear layers, but also on the adjacent secondary streams. The expansion and contraction of the underexpanded core forces the shear layers to bend accordingly, in a zig-zag fashion (as shown by the *plume* boundaries in Figure 5.18). As a result, the shear layers differ increasingly in shape and nature with increasing primary underexpansion, from those in the ideally expanded ejector (Figure 5.15). For sufficiently high underexpansion, the bending of the shear layers locally reduces the secondary flow area (Figure 5.18), causing the speed of the unmixed secondary to accelerate accordingly.

All the effects mentioned above depend directly on the extent of primary underexpansion and, therefore, on the strength of the pressure waves in the supersonic core. For increased primary underexpansion, the pressure waves are stronger, the shock-cells in the wave pattern are larger (longer and wider), and the influence on the surrounding flow is more significant.

Despite the significant differences found early in the flow field, at the end of the *near field* (i.e. $x / H_{e,nozzle} = 9 - 14$) the net spatial growth of the shear layers is very similar in all cases, irrespective of total primary pressure.

5.5.2 Effect of Primary Underexpansion on Acoustic Emissions

The flow generated acoustic emissions also vary considerably in the range of flow conditions investigated. Acoustic peaks or spectral features were detected in all flow cases in the 2 kHz – 20kHz frequency range. These emissions appear to originate predominantly in the *near field*, in the neighborhood of the first two or three shock cells of the wave pattern ($2.01 \le x / H_{e,nozzle} \le 8.33$). In general, for the ideally and near ideally expanded flow cases ($1.0 \le P_{s,1} / P_{s,2} \le 1.2$) these peaks are broadband in nature, such as those typically associated with broadband shock associated noise. As the primary pressure is increased ($P_{s,1} / P_{s,2} \ge 1.13$), narrow discrete-like peaks appear in the acoustic spectra. These narrow peaks have been associated with the "screech" observed in underexpanded jets. In most instances the screech consists of several distinct frequencies; however, one frequency is normally more dominant.

The frequency and intensity of the screech emissions change with the extent of underexpansion in a way which indicates that a unique condition exists near test case 5 (Figure 4.39) or more specifically near a primary-to-secondary exit static pressure ratio of $P_{s,1}/P_{s,2} = 1.27$ (corresponding to $P_{0,1}/P_{s,2} = 7.3$). In general, the screech intensity increases with primary underexpansion up to test case 5 and then decreases with further underexpansion, while the peak screech frequency decreases slightly with increasing primary underexpansion (as predicted by theoretical models).

The screech observed in test case 5 consists of up to 4 overtones, and has a fundamental frequency of ~3.0 kHz. The fundamental frequency reached sound pressure levels of up to 153 db, which is more than 15 db than the highest screech intensities measured for any other flow case. Further, unlike all other flow cases, the fundamental frequency and the first overtone in case 5 persisted even at the most downstream microphone position ($x / H_{e,nozzle} = 22.6$).

The peak screech emissions exhibited by test case 5 correlate with the sonic-line results presented in Section 5.3.3. Namely, it was found that the sonic lines for test cases 1 through 5 (i.e. for cases for which screech intensity increases with underexpansion) seem to converge near the end of the first and second shock cells. At higher underexpansion (i.e. for cases in which screech intensity decreases with underexpansion) the sonic lines depart increasingly from this initial pattern.

These findings are in fundamental agreement with results reviewed in Section 2.2, previously reported for underexpanded jets (free-jets and ejector primary jets) from convergent nozzles (i.e. lower primary supply pressures and velocities).

5.5.3 Effect of Primary Underexpansion on Mixing and Ejector Performance

Primary underexpansion also affected the flow properties at the mixing-tube exit. In general, upon increasing the flow rate and the stagnation momentum of the primary stream (i.e. $P_{0,1}$), the measured static pressure at the mixing-tube exit becomes increasingly lower than the pressure which could be attained if the flow were ideal (inviscid) and fully mixed (uniform at the exit). However, a distinct departure from this trend was found near the flow case which resulted in the most intense screech emissions of all flows investigated (i.e. test case 5, for which $P_{s,1} / P_{s,2} = 1.27$). For this case, the exit static pressure (determined to be constant across the exit cross section in all cases) is unexpectedly closer to the ideal value (Figure 5.23). The same is true, but to a lesser extent, for test cases 4 ($P_{s,1} / P_{s,2} \approx 1.20$) and 6 ($P_{s,1} / P_{s,2} = 1.34$). Similarly, the exit flow velocities for test case 5 (obtained from measurements of static and pitot pressures) are relatively low and depart from the general trend exhibited by the other flow cases.

The unusually high exit static pressure in test case 5 can be traced to the earlier onset of the overall pressure rise inherent to the ejector flow field (Figure 5.25). This phenomenon indicates that the mixing process for this case is somewhat accelerated, relative to the other flow cases, leading to an exit flow which is slightly more mixed or uniform (i.e. lower flow skeweness, Figure 5.26). Further, these results lead to the conclusion that a greater portion of the total momentum is retained by the pressure term in test case 5.

The accelerated or enhanced mixing observed in test case 5 is perhaps due to a redistribution of turbulence within the shear layers (Quinn 1976), rather than the result of higher shear-layer growth rates (for no evidence of the latter was found, at least in the *near field*)

The unusual values of the exit flow properties for test case 5 also translate into a computed ejector performance which is slightly higher than expected.

CHAPTER 6
CONCLUSIONS AND RECOMMENDATIONS

6.1 Conclusions

An experimental investigation was conducted to examine in detail the effect of primary underexpansion on the flow field of a two-dimensional ejector particularly in the *near field*. All the main objectives were successfully met, including (a) developing the experimental facility (b) obtaining a detailed database for the range of flow conditions considered, (c) comparing shear layer development among the different flow cases and (d) establishing whether primary underexpansion can lead to better ejector performance for the range of conditions investigated Due to the large number of tests required, a secondary objective was to devise a test procedure that would ensure precise setting of the test conditions throughout the experiments. The results show that the test conditions were maintained within narrow margins of the desired values

The mean *near field* structure of the flow field was characterized in detail using the test measurements Schlieren visualization of the flow field provided qualitative and quantitative confirmation of the mean measurements The results are in close agreement with the fundamental behavior observed in these type of flow fields

The investigation showed that in the underexpanded flow cases the shear layers have a wavy or zigzag shape unlike the shear layers in the perfectly expanded *baseline* flow case for which the boundaries are straight At high primary pressures and short streamwise distances, the shear layers reach far into the original secondary flow area. At the end of the *near field* however, the net growth of the high-momentum center region (or *plume*) is very similar in all cases Despite the similar growth rate, one flow case results in slightly better mixing and ejector performance Further, the acoustic measurements revealed that this flow case also results in the strongest flow-generated screech among all cases considered

In addition the boundaries of the supersonic core (or sonic lines) were determined for all flow cases These boundaries represent an important parameter in compressible shear layers and, to this author's knowledge have not been considered in great detail previously particularly in ducted flows with adverse pressure gradients (e.g ejector flows) The results showed that the size of the shear-layer region where M ≥ 1 depends on the local free-stream Mach number of the primary core.

Several validation tests were also conducted to determine the extent to which the traversing probe disturbs the flow field. These type of validation experiments have not been included in other similar investigations It was found that the effect of the probe on the mean flow properties is relatively small However time-accurate measurements show that the probe intrusiveness can have a more significant effect on the turbulent properties

The results and conclusions obtained from this investigation can be summarized as follows

(1) The experimental flow conditions followed the test plan closely in all test series (i.e. Schlieren, side-wall pressures, pitot-pressures, and acoustic measurements) The largest deviations occurred for the Schlieren test series, and are attributed to the different surface quality provided by the optical windows. Further, the high repeatability of all the measurements shows that the test conditions were duplicated even in completely independent runs

(2) The flow at $x = 0$ is approximately piece-wise uniform. This is shown in all cases by the traverses made at $x = 0$, and more explicitly for the *baseline* case by the spanwise velocity distribution also used to model the flow at the mixing-tube exit. In addition, the velocity model shows that the *baseline* flow field gradually becomes three-dimensional as a result of wall effects. A similar transition is expected for the other test cases.

(3) The flow field is approximately symmetric about $y = 0$ between the mixing-tube inlet and streamwise distances ranging from $x / H_{e,nozzle} = 15$ to $x / H_{e,nozzle} = 20$. This is shown by the flow visualization experiments and also by the side-wall pressure, pitot-pressure, and acoustic measurements.

(4) The Schlieren photographs for the *baseline* case show that the expansion waves originating at the nozzle throat are not completely canceled at the trailing edge. Side wall pressure measurements show that these residual waves are weak, and result in free stream pressure changes of less than 5%. Opposite waves (i.e. from different families) are slightly different and as a result, the primary jet is not perfectly symmetric.

(5) The Schlieren photographs show that the shear layers in the *baseline* case are uniform and grow at a near constant rate. The photographs also show that the shear layers merge near $x / H_{e,nozzle} = 11.9$ indicating the end of the unmixed primary core. The waves mentioned in (4) experience multiple reflections from the shear layers.

(6) The Schlieren photographs for the underexpanded flow cases show Prandtl-Meyer expansions at the nozzle exit. These expansion waves are reflected from the shear layer as compression waves, forming a shock-cell structure and causing the primary

core to expand and contract repeatedly The shear layers in these flow cases have a wavy or zigzag shape, as they adapt to the expansion and contraction of the core.

(7) The Schlieren photographs show that the waves discussed in (4) and (6) penetrate the shear layer with each reflection and gradually dissipate in the streamwise direction

(8) The Mach number of the fully expanded primary core was computed for all cases using (a) inviscid flow predictions (b) Mach angles measured from the Schlieren images, and (c) pitot pressures, side wall pressures and isentropic relations All the results are in excellent agreement up to case 9 The results from (b) and (c) are in close agreement in all cases

(9) The side-wall pressure distributions show clearly the development of the flow field and the effect of underexpansion The centerline pressure varies in a quasi-periodic pattern which reflects the wave structure in the supersonic core In the *baseline* case the variation is small and occurs only at short distances, while in the highly underexpanded cases the variation is significant and is observed along the entire length of the mixing tube The centerline pressure gradually stabilizes as the waves in the core dissipate At the mixing-tube exit, the centerline pressure is approximately equal to the off-center pressures in all cases The waves also result in transverse pressure gradients across the supersonic core

(10) Outside the supersonic core static pressure also varies in the transverse direction as a result of streamline curvature This occurs mainly in the *near field* of the underexpanded flow cases inside or near the shear layers First order estimates indicate that the static pressure near the shear layer outer edges can differ from the local secondary free-stream pressure by as much as 9% The effect is more

significant near the sonic lines. However, transverse static-pressure gradients are always small in comparison to those observed for pitot pressure.

(11) The various measurements and calculations are in support of the assumption that static pressure is approximately constant in the spanwise direction, in all flow cases and irrespective of streamwise position.

(12) The pitot pressure traverses show that the shear layers reach the walls near $x / H_{e\,nozzle} = 15$ in all cases. Further, the results show that one shear layer reaches the wall first, tripping the flow field and causing it to lean to that side of the mixing tube.

(13) The shear layers in the *baseline* case exhibit self-similarity as early as $x / H_{e\,nozzle} = 1.58$. The similarity profile is still preserved at $x / H_{e\,nozzle} = 20$ (where $M_{y=H} = 1.4$), well beyond the end of the primary core and the point where the shear layers seem to reach the wall.

(14) The average *near field* shear layer growth rate for the *baseline* case is $\delta'_{pit} = 0.094$. This result is 13% higher than the predicted value for a planar, two-stream, constant pressure (i.e. free jets, etc.) mixing layer having the same free-stream conditions. The difference is attributed to the waves mentioned in (4) and also to the small increase in static pressure which occurs in the *near field* of the ejector flow. Nevertheless, the results are in good agreement with those reported for similar ejector shear layers and constant pressure mixing layer.

(15) In the *baseline* case, the shear-layer outer-edge definition (i.e. the edge adjacent to the secondary) based only on the secondary free stream pressure provides excellent

agreement with the traditional shear-layer definition. Therefore, the streamwise development of the *plume* is a suitable measure of shear-layer growth.

(16) The growth rate of the *plume* in the *near field* is $\omega'_{pl} = 0.12$ for the *baseline* case. By comparing this result with the growth rate given in (14) it can be concluded that the shear layers are skewed in the outward direction.

(17) In the underexpanded flows, the *plume* reflects clearly the shock-cell structure of the primary core and the wavy shape of the shear layers. At high primary pressures and short streamwise distances, the *plume* is considerably wider than in the *baseline* flow field as its boundaries reach far into the secondary free stream. However, at the end of the *near field*, the net spatial growth of the *plume* appears unaffected by underexpansion, in agreement with (12).

(18) The *near-field* sonic lines resemble the *plume* boundaries in all cases. In the *baseline* case the sonic lines are nearly straight, while in the underexpanded flows they have a wavy shape. At high primary pressures the sonic lines are found well outside the outer edges of the shear layers in the *baseline* case.

(19) The sonic line results for the *baseline* case demonstrate that, in compressible shear layers, the local width or extent of the supersonic region depends on the free-stream Mach numbers.

(20) Flow-generated screech was detected in most underexpanded flows. These emissions have a narrow bandwidth and relatively high intensity. In most cases they consist of a fundamental frequency or first harmonic and one or two overtones or higher harmonics. The measured screech emissions are most intense in the *near field* ($2.01 \le x / H_{e,nozzle} \le 8.33$) and the acoustic spectra are nearly identical on both sides

of the flow field. In test case 5 (for which $P_{s,1} / P_{s,2} = 1.27$, $P_{0,1} / P_{s,2} = 7.3$) the fundamental screech frequency ($f_{F1} = 3.0$ kHz) can reach up to 153 db, and up to four higher harmonics were identified (both highest among all flow cases). In general, the intensity of these emissions increases with primary underexpansion up to case 5. The trend is reversed as the primary is underexpanded further. The fundamental screech frequency decreases with increasing primary underexpansion, in agreement with results reported for choked jets.

(21) In test case 5, the average static pressure and velocity at the mixing-tube exit are in better agreement with the predicted fully-mixed conditions (relative to the other flow cases). The main streamwise pressure gradient begins earlier in the mixing tube, suggesting that the development of the mixed flow region is somewhat accelerated in this flow case. The relatively low exit flow skewness computed for this case also supports this view. The effect is small in magnitude, possibly due to the low entrainment ratios investigated, yet it is in good agreement with similar results reported for different geometry and flow conditions (Quinn, 1976).

(22) The effects summarized in (21) result in small improvements in test case 5 in terms of the ejector pressure ratio and the Stagnation Momentum Exchange Effectiveness and the ejector thrust augmentation.

(23) The effect of primary underexpansion on performance is small, but correlates well with the flow-generated screech mentioned in (20). Primary underexpansion and the resulting acoustic interactions are likely to benefit more ejectors with higher entrainment ratios, which normally suffer from incomplete mixing.

The tests conducted to determine the extent of probe intrusiveness on the flow field and the measurements showed that

(24) The presence of the traversing probe disrupts primarily the flow downstream from the probe. The probe seems to have only a small effect on the mean properties of the incoming flow. It was determined that the probe disturbs the incoming flow primarily when it is installed in regions where the core flow is subsonic (i.e. downstream in the mixing tube), where disturbances can propagate upstream more easily. When installed at short distances, the probe has little effect on the mean properties. This conclusion is clearly supported by Schlieren images obtained with the probe in the flow field. The acoustic measurements show that the probe can have a more significant effect on the turbulent properties.

6.2 Recommendations

Several areas deserve further consideration. Probably, most important among these is the cross sectional variation of flow properties. The characterization of the flow field could be improved by making additional pitot-pressure traverses to map completely each flow cross section sampled. Further, it would be very useful to complement pitot-pressure with static-pressure traverses. The additional measurements can be used to calculate more accurately the average exit properties and the ejector performance. In the underexpanded flows, the data would help quantify more precisely the property gradients across the supersonic core and the effect of streamline curvature.

Obtaining more detailed measurements, however, necessitates increasing the scale of the test section. This drawback partly explains why in most experimental investigations only one traverse was used at each cross section.

Measurements of turbulent wall pressures would also be useful to determine the fluctuating-pressure distributions and quantify the shear-layer growth rates in the underexpanded flows. It has been demonstrated for an ideally expanded ejector (Benjamin, 1994) that growth rates obtained from turbulent wall pressures are in good agreement with those computed from pitot-pressure. The turbulent pressure distribution across the shear layers can help explain the early development exhibited by test case 5. Further, turbulent wall pressures can help locate the inner edge of the shear layers in the underexpanded flows and can be measured without disturbing the flow field.

The implementation of other nonintrusive techniques such as LDV or Planar Laser Induced Fluorescence would also be desirable. These techniques have been utilized extensively in studies of constant-pressure mixing layers.

The scope of this investigation can be expanded to include higher entrainment ratios, ejectors with variable mixing tube length, dissimilar primary and secondary gases, and different primary and secondary flow conditions (i.e. M, T_0, etc.). The database could be used to identify the flow regimes for which ejector performance benefits most from primary underexpansion. The data could also be used to obtain a functional correlation for the sonic lines, as suggested in Chapter 5.

Lastly, it would be useful to investigate means by which to enhance screech, and determine the effect of the augmented emissions on ejector performance.

APPENDIX A
INSTRUMENTATION SPECIFICATIONS AND MEASUREMENT ERRORS

A.1 Instrumentation Specifications

Pressure measurements

(1) total primary pressure

designation	$P_{0,1}$
instrument (make/model)	transducer (Omega PX181G 5V)
range	0 – 413 kPa (gage)
accuracy	linearity (BSFL) ±0.25% span repeatability & hysterisis ±0 05% span

(2) total secondary pressure

designation	$P_{0,2a}$ $P_{0,2b}$
instrument (make/model)	transducer (Micro Switch 140PC)
range	±101 4 kPa (differential 203 kPa total)
accuracy	linearity ±0 75% FSO repeatability ±15% FSO

(3) primary and secondary exit static pressures

designation	$P_{s,1}$ $P_{s,2a}$ $P_{s,2b}$
instrument (make/model)	transducer (Micro Switch 140PC)
range	±101 4 kPa (differential, 203 kPa total)
accuracy	linearity ±0 75% FSO repeatability ±15% FSO

(4) total-flow orifice upstream static pressure

designation	$P_{o1,tot}$
instrument (make/model)	transducer (Omega PX241G-5V)
range	2070 kPa (gage)
accuracy	linearity (BSFL) ±0 25% span repeatability & hysterisis ±0 05% span

(5) total-flow orifice downstream static pressure

designation	$P_{o2,tot}$
instrument (make/model)	transducer (Validyne DB15)
range	0 – 69 0 kPa (differential)
accuracy	±0 25% span

(6) secondary-flow orifice upstream static pressure

designation	$P_{r1,2}$
instrument (make/model)	transducer (Validyne DB15)
range	0 – 103 kPa (differential)
accuracy	±0 25% span

(7) secondary-flow orifice downstream static pressure

designation	$P_{r2,2}$
instrument (make/model)	transducer (Validyne DB15)
range	0 – 69 0 kPa (differential)
accuracy	±0 25% span

(8) pitot pressure

designation	P_{pit}
instrument (make/model)	transducer (Validyne DB15)
range	0 – 414 kPa (differential)
accuracy	±0 25% span

(9) static side-wall pressure at probe streamwise position, upper (y = +19 69 mm), center (y = 0), and lower taps (y = +19 69 mm)

designation	$P_{s,pit,u}$, $P_{s,pit,c}$, $P_{s,pit,l}$
instrument (make/model)	transducer (Micro Switch 140PC)
range	±101 4 kPa (differential, 203 kPa total)
accuracy	linearity ±0 75% FSO repeatability ±15% FSO

(10) other static side wall pressures

designation	P_{gic}
instrument (make/model)	mercury manometer (Merian Instrument Co , model 33M1335)
range	N/A
accuracy	scale accuracy ±1.25 mm Hg estimated effective accuracy ±5 mm Hg

Temperature measurements

(1) primary and secondary plenum temperatures

designation	$T_{0,1}$, $T_{0,2s}$
instrument (make/model)	type T copper-constantan thermocouple Omega (exposed junction of 1 59 mm dia.)
range	N/A
accuracy	given ±0 25°C estimated effective accuracy ±1 5°C

(2) ambient temperature

designation	T_{amb}
instrument (make/model):	mercury in glass thermometer (Fisher Scientific)
range	50 – 100°F (10 – 38°C)
accuracy:	given ±0.25°F (±0.1°C)

Acoustic measurements

spectral sound pressure level

instrument (make/model):	microphone (Kulite MIC-062 LT)
range	100 – 190 dba nearly flat response to 50 kHz
sensitivity	−129.12 db at 1 μbar
thermal sensitivity:	±0.5 db/100°F
instrument (make/model):	Fourier analyzer (Tektronix 2642)
frequency	±0.01%

A.2. Measurement Errors

Several months of testing were required to collect all the necessary data. As a result the calibration of the pressure transducers was checked several times to ensure that their accuracy was preserved. Further, the zero-output reading of each transducer was measured before each series of tests and the calibration was adjusted as necessary. Similarly, because the ambient pressure was used to compute absolute pressure levels, this pressure was monitored several times during each day of testing. The gains and outputs of the multiplexer boards were also checked periodically, and adjustments were made when necessary. The uncertainties of various computed quantities (e.g. Mach, mass flow rate, etc.) which result from the uncertainties of the basic measurements are discussed in Appendix C.

In addition to the measurement errors associated with the accuracy limits of the different instrumentation, there are other possible sources of error which could have affected the various measurements. These errors are related to the test procedure, the way in which the instrumentation was used, or a combination of these factors However, the errors are believed to be small and of little importance to the objectives of this investigation

A.2.1 Flow Conditions and Mass Flow Rates

Among the sources of error that can be identified was the resetting of the flow conditions required to collect all the data (as discussed in Section 4 1). This was particularly true insofar as the secondary flow and the inlet mixing-tube static pressure is concerned The secondary flow was always unchoked and its adjustment, together with the adjustment of the inlet static pressure was done simultaneously by trial and error

Errors in the secondary flow conditions were also introduced as a result of the hardware changes required by the test procedure (probe position, side-wall position, etc) This is also true for the primary flow rate although to a much lesser extent. As explained in Section 4 1.2, the hardware changes may have resulted in small changes in the distribution of the quality of the wetted surface and/or the cross section of the mixing tube, which in turn sometimes affected the pressure distribution in the mixing tube The variation in pressure distribution was small yet inevitable and its effect was felt primarily by the secondary Mach number (for reasons discussed in Section 5 2) Therefore rather than collecting data for a flow with considerably different secondary flow velocity it was decided to vary the secondary flow rate when necessary to maintain the nominal inlet static pressure and secondary flow velocities. Thus the secondary flow was slightly different from the nominal flow rate in a few test runs (the difference was never more than ~4%)

Another possible source of error is the use of the total primary and secondary temperatures, measured at the respective plenums, for the orifice plate calculations This procedure was followed after assuming constant air temperature between the orifice plates and the plenums. This assumption is justified because (a) the supply air is at near room temperature, (b) the velocities in the supply lines leading from the orifice plates to the plenums are relatively low, (c) these supply lines are relatively short, and (d) the duration of the test runs is only a few seconds. Therefore, error is believed to be small, particularly since the mass flow rate depends on temperature as $T_0^{1/2}$.

A.2.2 Pitot Pressures

Small errors in the measurement of pitot pressures can result from the transient response of the probe. During the early stages of the probe design, numerous attempts were made at determining the ability of the probe to accurately detect transients (such as those encountered by the probe when it traverses across the shear layer). The result of these efforts showed that the response of the probe/transducer configuration must be similar to that of the transducer alone (i.e. ~1 ms). The time traveled by the probe during that time is 0.0261 mm, approximately, which is slightly more than the position resolution of the probe (0.0254 mm). Thus the measured pitot pressure is expected to lag somewhat the actual pitot pressure.

Another source of error inherent to pitot pressure measurement in supersonic flow are the losses experienced across the shock which forms in front of the probe. While small, these losses are evident from results presented in Table 4.5. Thus, in these flow regions the pitot pressures in general are slightly lower than those predicted for the ideal case, which results in Mach numbers that are lower than those computed from Mach angle.

A.2.3 Side Wall Pressures

The procedure used to measure side-wall pressure (Sections 3.5.1 and 3.5.3) made possible to achieve the most consistent flow conditions among all test series. The main source of uncertainty and error in these measurements was due to the residual oscillation of the manometer columns that persisted even after allowing for a relatively long settling time. This oscillation was the result of the initial sudden change in test-section pressure.

While the oscillation of the mercury columns never decayed completely, all the columns appeared to oscillate approximately in phase after the initial settling time. Therefore, it was assumed that the pressure in each column had reached a steady-state condition representative of the pressure field in the test section. The readings obtained from two photographs of the manometer (obtained in separate runs as explained in Section 3.3.3) were always very similar (almost always within 1.7 kPa and in most cases within 0.68 kPa) confirming the above assumption. It was therefore concluded that the errors which resulted due to the unsteadiness of the manometer columns are relatively small. Further, because the readings obtained from the two photographs were always very similar, a mean side-wall pressure was obtained. Benjamin (1994) obtained mean measurements of side-wall pressure using readings from 4 and 5 photographs taken during the same run. His results provide additional support for the above assumption and approach used here.

APPENDIX B
SUMMARY OF TEST MEASUREMENTS

Table B.1 Pitot-pressure traverses made with long brass walls installed upstream

Test Case	1	2	3	4	5	6	7	8	9	10	11
x = 0.0 mm	TU	TU	TU	TU	TU	TU	TU	TU	TU	TU	C
10.0	TU	TU	TU	TU	TU	TU	TU	TU	TU	TU	TU
20.0	TU	TU	TU	TU	TU	TU	TU	TU	TU	TU	TU
30.0	TU	TU	TU	TU	TU	TU	TU	TC	C	C	C
40.0	TU	TU	TU	TU	TU	TU	TU	TC	C	C	C
50.0	TU	TU	TU	TU	TU	TU	TU	TU	TU	TC	C
60.0	TU	TU	TU	TU	TU	TU	TU	TU	TU	TC	C
70.0	TU	TU	TU	TU	TU	TU	TU	TU	TU	TU	TU
80.0	TU	TU	TU	TU	TU	TU	TU	TU	TU	TU	TU
90.0	TU	TU	TU	TU	TU	TU	TU	TU	C	C	C
100.0	TU	TU	TU	TU	TU	TU	TU	TU	C	C	C
110.0	TU	TU	TU	TU	TU	TU	TU	TU	TU	TU	TC
120.0	TU	TU	TU	TU	TU	TU	TU	TU	TU	TU	TC
130.0	TU	TU	TU	TU	TU	TU	TU	TU	TU	TU	TU
140.0	TU	—	TU	—	TU	—	TU	—	TU	—	TU
150.0	TU	TU	TU	TU	TU	TU	TU	TU	TC	C	C
160.0	TU	—	TU	—	TU	—	TU	—	TC	—	C
170.0	TU	TU	TU	TU	TU	TU	TU	TU	TU	TU	C
180.0	TU	—	TU	—	TU	—	TU	—	TU	—	C
190.0	TU	TU	TU	TU	TU	TU	TU	TU	TC	TU	TU
200.0	TU	—	TU	—	TU	—	TU	—	TC	—	TU
210.0	—	—	—	—	—	—	—	—	—	—	—
220.0	TU	—	TU	—	TU	—	TU	—	TC	—	C
230.0	—	—	—	—	—	—	—	—	—	—	—
240.0	TU	—	TU	—	TU	—	TU	—	TU	—	TC
250.0	—	—	—	—	—	—	—	—	—	—	—
250.0	TU	TU	TU	TU	TU	TU	TU	TU	TU	TU	TU

T – traverse U – flow unchoked C – flow choked — no attempts made

Table B.2 Pitot-pressure traverses made with long brass walls installed downstream

Test Case	1	2	3	4	5	6	7	8	9	10	11
x = 176.2 mm	—	—	—	—	—	—	—	—	—	—	—
186.2	—	—	—	—	—	—	—	—	—	—	—
196.2	—	—	—	—	—	—	—	—	—	—	—
206.2	—	—	—	—	—	—	—	—	—	—	—
216.2	—	—	—	—	—	—	—	—	—	—	—
226.2	—	—	—	—	—	—	—	—	—	—	—
236.2	—	—	—	—	—	—	—	—	—	—	—
246.2	—	—	—	—	—	—	—	—	—	—	—
256.2	—	—	—	—	—	—	—	—	—	—	—
266.2	—	—	—	—	—	—	—	—	—	—	—
276.2	TU	—	TU	—	TU	—	TU	—	TU	—	TU
286.2	—	—	—	—	—	—	—	—	—	—	—
296.2	TU	—	TU	—	TU	—	TU	—	TU	—	TU
306.2	—	—	—	—	—	—	—	—	—	—	—
316.2	TU	—	TU	—	TU	—	TU	—	TU	—	TU
326.2	—	—	—	—	—	—	—	—	—	—	—
336.2	TU	—	TU	—	TU	—	TU	—	TU	—	TU
346.2	—	—	—	—	—	—	—	—	—	—	—
356.2	TU	—	TU	—	TU	—	TU	—	TU	—	TU
366.2	—	—	—	—	—	—	—	—	—	—	—
376.2	TU	—	TU	—	TU	—	TU	—	TU	—	TU
386.2	—	—	—	—	—	—	—	—	—	—	—
396.2	TU	—	TU	—	TU	—	TU	—	TU	—	TU
406.2	—	—	—	—	—	—	—	—	—	—	—
416.2	TU	—	TU	—	TU	—	TU	—	TU	—	TU
426.2	—	—	—	—	—	—	—	—	—	—	—
436.2	TU	TU	TU	TU	TU	TU	TU	TU	TU	TU	TU

T – traverse, U – flow unchoked, C – flow choked, — no attempts made

Table B 3 Streamwise microphone positions used for acoustic measurements (z = 0 for all cases)

Test Case	x (mm)							
	25 4	45 4	65 4	85 4	105 4	125 2	185 4	285 4
1	T B	T	T	T B T^1 T^2	T	T T^1	T	T
2	T			T				T
3	T B	T	T	T B	T	T	T	T
4	T			T				T
5	T B	T	T	T B T^1 T^2	T	T T^1 T^2	T	T
6	T			T				T
7	T B	T	T	T B	T	T	T	T
8	T			T				T
9	T B	T	T	T B T^1 T^2	T	T T^1 T^2	T	T
10	T			T				T
11	T B	T	T	T B	T	T	T	T

T measurements made at y = + 25 8 mm, z = 0 (top wall)
B measurements made at y = - 25 8 mm z = 0 (bottom wall)
1 impact probe installed at x = 120 0 mm (stem at x = 145 4 mm)
2 impact probe installed at x = 260 4 mm (stem at x = 285 4 mm)

APPENDIX C
EQUATIONS AND CALCULATIONS

C.1 Manometer Side-Wall Pressure Calculations

Manometer readings for side wall pressure measurements were converted to pressure using the expression

$$P_s = P_{ref} - \left(h_{ref} - h_s\right)c_1 \qquad \text{(C.1)}$$

where P_s – side-pressure measurement (kPa)

P_{ref} – reference pressure (kPa)

h_{ref} – height of reference manometer column (in of Hg)

h_s – height of manometer column (in of Hg) corresponding to P_s

$c_1 = 3.3854$ (kPa/in Hg)

Corrections for temperature variation were too small to have any effect on the results.

C.2 Mass Flow Calculations

The mass flow rate, $\dot{m}$, was computed from orifice plate measurements using the expression (Holman, 1978)

$$\dot{m} = \frac{C_d Y A_{o2}}{\sqrt{1 - \beta^2}} \sqrt{\frac{2 P_{o2} M_w (P_{o1} - P_{o2})}{R_u T_{o1}}} \qquad \text{(C.2a)}$$

where P_{o1} – upstream pressure measurement

T_{o1} – upstream air temperature

P_{o2} – downstream pressure measurement

M_w – molecular weight (for air 28.97)

R_u – universal gas constant (8314 J/kgmol K)

β – diameter ratio (d_{o2} / d_{o1})

d_{o1} – pipe diameter (49.2 mm)

d_{o2} – orifice diameter (25.4 mm)

A_{o2} – orifice area ($\pi d_{o2}^2/4$)

Y – expansion factor

C_d – orifice discharge coefficient

For a sharp-edge orifice plate with flange taps, the expansion factor is given by (Holman 1978)

$$Y = 1 - \left(0.41 + 0.35\beta^4\right)\frac{P_{o1} - P_{o2}}{\gamma P_{o1}} \qquad \text{(C.2b)}$$

where γ is the specific heat ratio (for air 1.4). The discharge coefficient for a sharp-edge orifice is given by the expression (White, 1994)

$$C_d = \mathscr{F}(\beta) + 91.71\,\beta^{2.5}\mathrm{Re}_{d_{o1}}^{-0.75} + \frac{0.09\beta^4}{1 - \beta^4}F_1 - 0.0337\beta^3F_2 \qquad \text{(C.2c)}$$

where $\mathscr{F}(\beta) = 0.5959 + 0.0312\beta^{2.1} - 0.184\beta^8$ (C.2e)

$F_1 = 0.4333$ (for flange taps where $5.08 \text{ cm} \le d_{o1} \le 5.84 \text{ cm}$)

$F_2 = 1 / d_{o1}$ (for flange taps: d_{o1} in inches)

$\mathrm{Re}_{d_{o1}}$ – Reynolds number based on the pipe diameter d_{o1}

The above formulation required an iterative solution, using $C_d = 1$ as initial guess. From the resulting mass flow rate a value for $\mathrm{Re}_{d_{o1}}$ was obtained, and a new C_d, and the calculations were repeated until convergence occurred.

The mass flow rate was also computed using ideal, isentropic relations and the pressure measurements from the plenums. Here, it was assumed that the primary and secondary flows in the settling chambers and across the exits are approximately uniform (one-dimensional). The isentropic mass flow equation is

$$\dot{m} = \sqrt{\frac{M_w \gamma}{R_u T_0}}\, P_0 A_e \frac{M}{\left(1 + \frac{\gamma - 1}{2} M^2\right)^{\frac{\gamma + 1}{2(\gamma - 1)}}} \tag{C.3}$$

where M – primary or secondary exit Mach number

P_0 – primary or secondary total pressure

T_0 – primary or secondary total temperature

A_e – primary or secondary exit area ($A_e = H_e \cdot W_e$, $W_e = 25.4$ mm, primary $H_e = 12.65$ mm, each secondary $H_e = 19.05$ mm)

The Mach number can be eliminated from Equation C.4 with the aid of the isentropic relation (Equation 4.1)

$$\frac{P_0}{P_s} = \left(1 + \frac{\gamma - 1}{2} M^2\right)^{\frac{\gamma}{\gamma - 1}} \tag{C.4}$$

where P_s is the primary or secondary exit (static) pressure. The resulting expression is

$$\dot{m} = \sqrt{\frac{2 M_w}{R_u T_0} \frac{\gamma}{\gamma - 1}}\, P_0 A_e \sqrt{\left\{\left(\frac{P_0}{P_s}\right)^{\frac{\gamma - 1}{\gamma}} - 1\right\}\left(\frac{P_s}{P_0}\right)^{\frac{\gamma + 1}{\gamma}}} \tag{C.5}$$

The uncertainty of the mass flow rate was obtained using propagation of uncertainties. The dominant uncertainties in Equation C.6 are those for P_0 and P_s. Hence, it can be shown that the mass flow uncertainty, $w_{\dot{m}}$, is given by

$$w_{\dot{m}} = c_2 \frac{\sqrt{r_p^{c_3} - 1}}{r_p^{c_4}} \sqrt{\left(1 + \frac{c_3}{2}\frac{1}{1 - r_p^{c_3}} - c_4\right)^2 w_{P_0}^2 + \left(c_4 r_p - \frac{c_3}{2}\frac{r_p}{1 - r_p^{c_3}}\right)^2 w_{P_s}^2} \tag{C.6}$$

where $c_2 = \sqrt{\frac{2M_w}{R_u T_0}\frac{\gamma}{\gamma - 1}} A_e$

$r_p = P_0 / P_s$

$c_3 = (\gamma - 1) / \gamma$

$c_4 = (\gamma + 1) / (2\gamma)$

w_{P_0} – uncertainty of P_0

w_{P_s} – uncertainty of P_s

Equation C.5 was also used for the area integral calculations at the mixing tube exit (Section C 5) The calculation in this case involved a finite area element, ΔA, and the pressures used where $P_0(y,z)$ and $P_s(y)$ The mass total mass flow was obtained from the summation over all area elements

$$\dot{m} = \sum_{j,k} \Delta\dot{m}_{j,k} \qquad j = 1 \ldots 373 \quad k = 1 \ldots 101 \tag{C 7}$$

C 3 Mach Number Calculations

The primary and secondary exit Mach numbers where computed by assuming one-dimensional isentropic flow and using the isentropic relation Equation 4 1 (also C 4) The Mach number uncertainty was obtained using propagation of uncertainties, and is given by

$$w_M = \frac{\sqrt{c_5}}{2} \frac{r_p^{c_3 - 1}}{\sqrt{r_p^{c_3} - 1}} \sqrt{\left(\frac{w_{P_0}}{P_s}\right)^2 + r_p^2\left(\frac{w_{P_s}}{P_s}\right)^2} \tag{C.8}$$

where $c_5 = (\gamma - 1) / 2$ and r_p is defined in the previous section

In other regions of the flow field, the Mach number is computed from measurements of pitot pressure and side-wall pressure as described in Section 4 3 1 Equation 4 1 is used for cases where $P_{pt} / P_s \leq 1.8929$, in which case $P_0 = P_{pt}$. Otherwise, the Rayleigh formula (Equation 4 3)

$$\frac{P_{pt}}{P_s} = \left(\frac{\gamma+1}{2}M^2\right)^{\frac{\gamma}{\gamma-1}} \left(\frac{2\gamma}{\gamma+1}M^2 - \frac{\gamma-1}{\gamma+1}\right)^{\frac{1}{1-\gamma}} \qquad (C\ 9)$$

is solved by iteration In this case it can be shown that by applying the chain rule to Equation C 9, propagation of uncertainty analysis gives

$$w_M = \left\{\frac{2}{c_3 M} - \frac{2M}{\left(2M^2 - c_5\right)c_5}\right\}^{-1} \sqrt{\left(\frac{w_{P_{pt}}}{P_s}\right)^2 + \left(\frac{w_{P_s}}{P_s}\right)^2} \qquad (C\ 10)$$

where M is the Mach number obtained from Equation C 9, and the constants c_3 and c_5 are defined earlier

In either case, it is assumed that the flow static pressure is approximately constant in the spanwise direction (i.e. $P_s \neq f(z)$) and, hence, approximately equal to the corresponding side-wall pressure

C.4 Predicted Exit Flow Properties

The ideal and actual ejector performances were calculated using a quasi one-dimensional control volume approach for the momentum, continuity and energy equations Similar formulations have been used by many (Addy et. al 1981, Quinn, 1976 for example) and is presented here for reference. The formulation is developed for the specific case where the same gas is used for the primary and secondary, and for an ejector having a constant area mixing tube. After the formulation is presented, the working equations are simplified further for the case where the primary and secondary have the same stagnation temperature

Several assumptions were used in solving the governing equations, which include

(1) steady flow,

(2) uniform and parallel primary and secondary exit flows

(3) the air used for the primary and secondary behaves as a thermally and calorically perfect gas (i.e. perfect gas with constant properties),

(4) adiabatic flow,

(5) negligible body forces,

(6) negligible changes in potential energy,

(7) no shaft or shear work in the mixing tube, and

(8) isentropic primary and secondary flows up to their respective exit planes

In the analysis presented below the stations corresponding to the primary and secondary exit planes (x_0 in figure 2.1) are denoted by 1 and 2 respectively The mixing tube exit plane (x_e in figure 2 1) is denoted as station 3 The first assumption leads to the steady state form of the governing equations

continuity $$\oint_{cs} \rho \mathbf{V} \cdot d\mathbf{A} = 0 \qquad \text{(C 11a)}$$

x-momentum $$\oint_{cs} V_x \rho \mathbf{V} \cdot d\mathbf{A} = F_x \qquad \text{(C 11b)}$$

energy $$\oint_{cs} \left(h + \frac{V^2}{2} + gz\right) \rho \mathbf{V} \cdot d\mathbf{A} = \frac{dQ}{dt} - \frac{dW_s}{dt} \qquad \text{(C 11c)}$$

In addition to these governing equations the following equations of state are available

ideal gas $$P = \rho \frac{R_u}{M_w} T \qquad \text{(C 12)}$$

isentropic $$P = \rho^{\gamma} \tag{C.13}$$

The steady state energy equation for any perfect gas obtained using assumption (3) is

$$h_0 = h + \frac{V^2}{2} \tag{C.14}$$

which, for an ideal gas (i.e. $h = c_p T$) also takes the form

$$\frac{T_0}{T} = 1 + \frac{V^2}{2c_p T} = 1 + \frac{\gamma - 1}{2} M^2 \tag{C.15}$$

In this equation, the Mach number (for a perfect gas) is given by

$$M = \frac{V}{\sqrt{\gamma R_u T / M_w}} \tag{C.16}$$

Using assumption (2) continuity becomes

$$\rho_1 V_1 A_1 + \rho_2 V_2 A_2 = \int_{A_3} \rho V \cdot dA \tag{C.17}$$

which in terms of the mass flow rates can also be expressed as

$$\dot{m}_1 + \dot{m}_2 = \dot{m}_3 \tag{C.18}$$

By introducing the Equations C.12, C.15 and C.16, the mass flow rate can be expressed as

$$\dot{m}_i = \rho_i V_i A_i = P_i A_i \sqrt{\frac{M_w}{R_u T_{0i}}}\, f_1(\gamma, M_i) \qquad (i = 1, 2, 3) \tag{C.19}$$

where the function $f_1(\gamma_i, M_i)$ known as the flow function is defined as

$$f_1(\gamma, M_i) = M \sqrt{\gamma \left(1 + \frac{\gamma - 1}{2} M^2\right)} \tag{C.20}$$

After introducing assumption (2) the x-momentum equation becomes

$$P_1 A_1 + \rho_1 A_1 V_1^2 + P_2 A_2 + \rho_2 A_2 V_2^2 = F_x + \int_{A_3} P dA + \int_{A_3} V_x \rho V \cdot dA \tag{C.21}$$

Similarly, after introducing assumptions (2), (4), (6), and (7), and Equation C.14, the energy equation becomes

$$\dot{m}_1 h_{0,1} + \dot{m}_2 h_{0,2} = \int_{A_3} \rho h_0 \mathbf{V} \cdot d\mathbf{A} \tag{C.22}$$

Quinn (1976) accounted for incomplete mixing at station 3 by introducing the following definitions

$$\bar{V} = \int_A u\, d\left(\frac{a}{A}\right) \tag{C.23a}$$

$$\bar{\lambda} = \int_A \lambda\, d\left(\frac{a}{A}\right) \qquad (\lambda - \text{any property}) \tag{C.23b}$$

$$\alpha_1 = \int_A \left(\frac{\rho}{\bar{\rho}}\right)\left(\frac{u}{\bar{V}}\right) d\left(\frac{a}{A}\right) \tag{C.23c}$$

$$\alpha_2 = \int_A \left(\frac{\rho}{\bar{\rho}}\right)\left(\frac{u}{\bar{V}}\right)^2 d\left(\frac{a}{A}\right) \tag{C.23d}$$

$$\alpha_3 = \int_A \left(\frac{\rho}{\bar{\rho}}\right)\left(\frac{u}{\bar{V}}\right)^3 d\left(\frac{a}{A}\right) \tag{C.23e}$$

$$\varepsilon = \int_A \left(\frac{\rho}{\bar{\rho}}\right)\left(\frac{u}{\bar{V}}\right)\left(\frac{T}{\bar{T}}\right) d\left(\frac{a}{A}\right) \tag{C.23f}$$

The last four equations represent the moments or skewness factors of the exit flow. By introducing equations C.19, C.23a, and C.23b, equation C.18 can be written as

$$\frac{P_1 A_1}{\sqrt{T_{0,1}}} f_1(\gamma, M_1) + \frac{P_2 A_2}{\sqrt{T_{0,2}}} f_1(\gamma, M_2) = \alpha_1 \frac{\bar{P}_3 A_3}{\sqrt{T_{0,3}}} f_1(\gamma, \bar{M}_3) \tag{C.24}$$

Similarly, substitution of Equations C.23a, C.23b, and C.23d into Equation C.21 gives

$$P_1 A_1 + \rho_1 A_1 V_1^2 + P_2 A_2 + \rho_2 A_2 V_2^2 = F_x + \bar{P}_3 A_3 + \alpha_2 \bar{\rho}_3 \bar{V}_3^2 A_3 \tag{C.25}$$

The force F_x corresponds to the friction force in the wall. Quinn (1976) used an empirical correlation for friction which as the form

$$F_s = F_f = C_f\left(\frac{A_{wet}}{A_3}\right)\left(\frac{V_{wall}}{\bar{V}_3}\right)^2\frac{1}{2}\bar{\rho}_3 V_3^2 A_3 \tag{C.26}$$

where C_f, A_{wet} and V_{wall} are the coefficient of skin friction the surface area of the mixing tube and the velocity at the edge of the boundary layer at station 3 respectively The value of V_{wall} is obtained from the line integral around the perimeter of the mixing-tube cross section, near the edge of the boundary layer

$$V_{wall} = \oint_P u\, d\left(\frac{s}{P}\right) \tag{C 27}$$

With the aid of Equations C 12 and C 16 Equation C 26 can also be written as

$$F_f = \xi_f \gamma \bar{P}_3 M_3^2 A_3 \tag{C 28}$$

where

$$\xi_f = C_f\left(\frac{A_{wet}}{A_3}\right)\left(\frac{V_{wall}}{\bar{V}_3}\right)^2 \tag{C 29}$$

Substitution of Equation C.28 into Equation C.25 gives

$$P_1A_1 + \rho_1A_1V_1^2 + P_2A_2 + \rho_2A_2V_2^2 = \xi_f\gamma\bar{P}_3\bar{M}_3^2A_3 + \bar{P}_3A_3 + \alpha_2\bar{\rho}_3\bar{V}_3^2A_3 \tag{C 30}$$

which can be rearranged with the aid of Equations C.12 and C 16 in the form

$$\left(1 + \gamma M_1^2\right) + \frac{P_2A_2}{P_1A_1}\left(1 + \gamma M_2^2\right) = \frac{\bar{P}_3A_3}{P_1A_1}\left(1 + (\xi_f + \alpha_2)\gamma M_3^2\right) \tag{C.31}$$

By letting $\mu = \dot{m}_2/\dot{m}_1$ (entrainment ratio) Equation C 18 can be written as

$$1 + \mu = \frac{\dot{m}_3}{\dot{m}_1} \tag{C.32}$$

Combining Equation C 19 the entrainment ratio μ and Equation C 15 leads to

$$\frac{P_2A_2}{P_1A_1} = \sqrt{\frac{T_{0,2}}{T_{0,1}}}\,\frac{f_1(\gamma,M_1)}{f_1(\gamma,M_2)}\,\mu \quad \text{and} \quad \frac{P_3A_3}{P_1A_1} = \sqrt{\frac{T_{0,3}}{T_{0,1}}}\,\frac{f_1(\gamma,M_1)}{f_1(\gamma,M_3)}\,\frac{(1+\mu)}{\alpha_1} \tag{C.33}$$

After introducing Equations C.33, Equation C.30 can be written in the form

$$\sqrt{\frac{T_{0,2}}{T_{0,1}}}\mu\frac{1+\gamma M_2^2}{f_1(\gamma,M_2)}+\frac{1+\gamma M_1^2}{f_1(\gamma,M_1)}=\sqrt{\frac{\bar{T}_{0,3}}{T_{0,1}}}\frac{(1+\mu)}{\alpha_1}\frac{1+(\xi_f+\alpha_2)\gamma\bar{M}_3^2}{f_1(\gamma,\bar{M}_3)} \qquad \text{(C.34)}$$

For an ideal gas the energy equation (Equation C.22) can be written in the form

$$\dot{m}_1T_{0,1}+\dot{m}_2T_{0,2}=\int_{A_3}\left(T+\frac{u^2}{2c_p}\right)\rho u\,dA=\int_{A_3}T_0\rho u\,dA \qquad \text{(C.35)}$$

After introducing Equations C.23e and C23f the above expression becomes

$$\dot{m}_1T_{0,1}+\dot{m}_2T_{0,2}=\frac{\dot{m}_3}{\alpha_1}\varepsilon\bar{T}_3+\frac{\dot{m}_3}{\alpha_1}\alpha_3\frac{\bar{V}_2^2}{2c_p} \qquad \text{(C.36)}$$

By adding an subtracting the terms

$$\frac{\dot{m}_3}{\alpha_1}\varepsilon\frac{\bar{V}_3^2}{2c_p} \qquad \text{and} \qquad \frac{\dot{m}_3}{\alpha_1}\alpha_3\bar{T}_2$$

to Equation C.35, it is possible to show after some algebra that

$$\frac{\bar{T}_{0,3}}{T_{0,1}}=\kappa\frac{\alpha_1}{\varepsilon}\left(\frac{1+\mu T_{0,2}/T_{0,1}}{1+\mu}\right) \qquad \text{(C.37)}$$

where

$$\kappa=\left\{1+\left(\frac{\alpha_3}{\varepsilon}-1\right)\left(1-\frac{\bar{T}_3}{\bar{T}_{0,3}}\right)\right\}^{-1} \qquad \text{(C.38)}$$

In flows where the primary and secondary streams have the same stagnation temperatures ($T_{0,1}=T_{0,2}$) Equation C.35 gives $\bar{T}_{0,3}=T_{0,1}=T_{0,2}$. In the special case where the flow is fully mixed and has uniform properties at the exit (i.e. $\alpha_1=\alpha_2=\alpha_3=\varepsilon=\kappa=1$) Equation C.37 reduces to

$$\frac{\bar{T}_{0,3}}{T_{0,1}}=\frac{1+\mu T_{0,2}/T_{0,1}}{1+\mu} \qquad \text{(C.39)}$$

Equation C.39 also reduces to $\bar{T}_{0,2}=T_{0,1}=T_{0,2}$ when $T_{0,1}=T_{0,2}$. For this particular case Equation C.34 can be simplified and rearranged further in the form

$$F_3(\gamma,\bar{M}_3,\xi_f,\alpha_2) = \alpha_1 \frac{\mu f_3(\gamma,M_2) + f_3(\gamma,M_1)}{1+\mu} \tag{C.40}$$

where

$$F_3(\gamma,\bar{M}_3,\xi_f,\alpha_2) = \frac{1+(\xi_f+\alpha_2)\gamma M_3^2}{f_1(\gamma,\bar{M}_3)} \tag{C.41}$$

$$f_3(\gamma,M_i) = \frac{1+\gamma M_i^2}{f_1(\gamma,M_i)} \qquad (i = 1,\ 2) \tag{C.42}$$

Equation C.40 is a biquadratic which can be solved for the average Mach number at the mixing tube exit. The result is

$$\bar{M}_3 = \left\{ \frac{-\left(F_3^2-2(\xi_f+\alpha_2)\right) \pm \left\{\left(F_3^2-2(\xi_f+\alpha_2)\right)^2 + 2\frac{\gamma-1}{\gamma}\left(F_3^2-\frac{2(\xi_f+\alpha_2)\gamma}{\gamma-1}\right)\right\}^{\frac{1}{2}}}{(\gamma-1)\left(F_3^2-\frac{2(\xi_f+\alpha_2)\gamma}{\gamma-1}\right)} \right\}^{\frac{1}{2}} \tag{C.43}$$

The solution represents the behavior for an ejector in which the exit flow has a given skewness. The calculations are as follows:

(1) The constants α_1, α_2, and α_3 are computed from Equations C.23c, C.23d, and C.23e respectively, using the semi-empirical model for the exit velocity distribution ($\alpha_1 = \alpha_2 = \alpha_3 = 1$ for fully mixed, uniform flow).

(2) The value of ξ_f is obtained from Equations C.27 and C.29 using an appropriate value for the skin-friction coefficient, C_f (the special case of no wall friction corresponds to $\xi_f = C_f = 0$).

(3) The functions f_1 and f_3 (Equations C.20 and C.42) are evaluated at stations 1 and 2 and are used to compute the value of the function F_3 from Equation C.41.

(4) The average exit Mach number $\bar{M}_3$ is computed from Equation C.43, which in turn is used to evaluate the function f_1 at station 3.

(5) The average exit static pressure, $\bar{P}_3$, is found from the second of Equations C.33 (using the the simplification $T_{0,3} = T_{0,1}$ in the special case of constant total temperature).

(6) The average exit Mach number is used to calculate

$\bar{T}_3$ from Equation C.15

$\bar{P}_{0,3}$ from Equation C.5

$\bar{V}_3$ from Equation C.16

C.5 Average Exit Flow Properties

The model and assumptions used for the exit flow are discussed in Section 5.4.4. The sequence and procedure used to compute the exit flow is outlined below.

1 Calculations of flow properties for area elements in the center column $j = 2, \ldots 372$, $k = 51$

	parameter		required equations and input variables
(1)	$P_{pit} / P_s\|_{j,k}$	variables.	$P_{pit,j,k}$ and $P_{s,j,k=101}$ found from interpolation of side wall pressure (i.e. assuming $P_{s,j,k=51} = P_{s,j,k=101}$)
(2)	local Mach umber $M_{j,k}$	variables Equations.	$P_{pit} / P_s\|_{j,k}$ 4.1 or 4.4 (see also Section C.3)
(3)	local temperature $T_{j,k}$	variables Equations:	$M_{j,k}$ C.15 (Section C.4)
(4)	local total pressure $P_{0,j,k}$	variables Equations.	$M_{j,k}$ 4.1 for $M_{i,j} \ge 1$ (otherwise $P_{0,j,k} = P_{pit,j,k}$)
(5)	local density $\rho_{j,k}$	variables Equations	$T_{j,k}$ and $P_{s,j,k=101}$ found from interpolation of side-wall pressure (i.e. assuming $P_{s,j,k=51} = P_{s,j,k=101}$) ideal gas equation
(6)	local velocity	variables	$M_{j,k}$ and $T_{j,k}$

	$u_{j,k}$	Equations:	C.16 (Section C.4)
(7)	local mass flow rate $\Delta\dot{m}_{j,k}$	variables:	T_0, $P_{0,j,k}$, and $P_{s,j,k}$ found from interpolation of side wall pressure (i.e. assuming $P_{s,j,k=51} = P_{s,j,k=101}$)
		Equations:	C.5 with corresponding area element, $\Delta A_{j,k}$ (Section C.2)

II. Calculations of flow properties for the two area elements in the center column, outside the traverse $j = 1, k = 51$ and $j = 373, k = 51$

	parameter		required equations and input variables
(8)	local velocity $u_{j,k}$	variables:	$u_{j,k}$
		Equations:	$u_{j=1,k} = u_{j=2,k}/2$ or $u_{j=373,k} = u_{j=372,k}/2$ (from boundary layer and linear velocity profile assumptions, Section 5.4.3)
(9)	local temperature $T_{j,k}$	variables:	T_0 and $u_{j,k}$
		Equations:	C.15 (Section C.4)
(10)	local Mach umber $M_{j,k}$	variables:	$u_{j,k}$ and $T_{j,k}$
		Equations:	4.16 (Section C.3)
(11)	local total pressure $P_{0,j,k}$	variables:	$M_{j,k}$ and $P_{s,j,k}$ found from interpolation of side-wall pressure (i.e. assuming $P_{s,j,k=51} = P_{s,j,k=101}$)
		Equations:	4.1
(12)	local density $\rho_{j,k}$	variables:	$T_{j,k}$, and $P_{s,j,k=101}$ found from interpolation of side-wall pressure (i.e. assuming $P_{s,j,k=51} = P_{s,j,k=101}$)
		Equations:	ideal gas equation
(13)	local mass flow rate $\Delta\dot{m}_{j,k}$	variables:	T_0, $P_{0,j,k}$, and $P_{s,j,k}$ found from interpolation of side-wall pressure (i.e. assuming $P_{s,j,k=51} = P_{s,j,k=101}$)
		Equations:	C.5 with corresponding area element, $\Delta A_{j,k}$ (Section C.2)

III. Calculations of flow properties for area elements in all off-center grid columns $j = 1,..373$, $k = 1,..50$ and $k = 52,..101$

	parameter		required equations and input variables
(14)	constant n (Equation 5.10)		guess initial value
(15)	local velocity $u_{j,k}$	variables. Equations	$u_{j,k=51}$ (i.e. $u(y, z=0)$), n and $z_{i,k}$ 5.10
(16)	local temperature $T_{j,k}$	variables Equations	T_0 and $u_{j,k}$ C.15 (Section C.4)
(17)	local Mach umber $M_{j,k}$	variables Equations	$u_{j,k}$ and $T_{j,k}$ C.16 (Section C.4)
(18)	local total pressure $P_{0,j,k}$	variables	$M_{j,k}$ and $P_{s,j,k}$ found from interpolation of side wall pressure (i.e. assuming $P_{s,j,k} = P_{s,j,k=101}$)
		Equations.	4.1
(19)	local density $\rho_{j,k}$	variables:	$T_{j,k}$, and $P_{s,j,k=101}$ foud from interpolation of side-wall pressure (i.e. assuming $P_{s,j,k} = P_{s,j,k=101}$)
		Equations:	ideal gas equation
(20)	local mass flow rate $\Delta m_{j,k}$	variables	T_0, $P_{0,j,k}$, and $P_{s,j,k}$ found from interpolation of side-wall pressure (i.e. assuming $P_{s,j,k} = P_{s,j,k=101}$)
		Equations:	C.5 with corresponding area element $\Delta A_{j,k}$ (Section C.2)

IV Calculations of total mass flow rate and update constant n (if necessary) or computation of average exit properties.

	parameter		required equations and input variables
(21)	local mass flow rate $\dot{m}$	variables Equations.	$\Delta\dot{m}_{j,k}$, ($j = 1, \ldots 373$, $k = 1 \ldots 101$) C.7 (Section C.2)

(a) if $\dot{m}$ differs from the orifice plate measurements (Section C.2) by more than 0.1% the value of n is changed as necessary and the computations are repeated beginning at step (15)

(b) if $\dot{m}$ is within 0.1% of the orifice plate measurements (Section C.2), the average exit properties and average exit properties are computed as indicated below

(22)	average velocity $\overline{V}_3$	variables Equations	$v_{j,k}$, ($j = 1,\ldots 373$, $k = 1,\ldots 101$) C.23a (Section C.4)
(23)	average total pressure $\overline{P}_{0,3}$	variables Equations	$P_{0,j,k}$ ($j = 1,\ldots 373$, $k = 1,\ldots 101$) C.23b (Section C.4)
(24)	average temperature $\overline{T}_3$	variables Equations	$T_{j,k}$ ($j = 1,\ldots 373$, $k = 1,\ldots 101$) C.23b (Section C.4)
(25)	average density $\overline{\rho}_3$	variables Equations	$\rho_{j,k}$, ($j = 1,\ldots 373$, $k = 1,\ldots 101$) C.23b (Section C.4)
(26)	average static pressure $\overline{P}_3$	variables Equations	$P_{s,j,k}$ found from interpolation of side-wall pressure (i.e. assuming $P_{s,j,k} = P_{s,j,k=101}$) ($j = 1,\ldots 373$, $k = 1,\ldots 101$) C.23b (Section C.4)

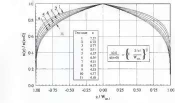

Figure C.1 Spanwise velocity distributions assumed at the mixing-tube exit.

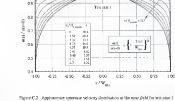

Figure C.2 Approximate spanwise velocity distribution in the *near field* for test case 1

REFERENCES

Abramovich G N , 1963, The Theory of Turbulent Jets Cambridge Massachusetts M.I.T Press pp 36–42

Addy A. L., 1972, "The Analysis of Supersonic Ejector Systems " AGARDograph No 163 on Supersonic Ejectors (Ginoux J J , ed) pp 31–101

Addy, A L. Dutton, J. C , and Mikkelson, C D 1981 ' Supersonic Ejector Diffuser Theory and Experiments " Report No UILU-ENG–82–4001 Department of Mechanical and Industrial Engineering University of Illinois at Urbana-Champaign, Urbana, Illinois

Anderson, B H., 1974, "Computer Program for Calculating the Flow Field of Supersonic Ejector Nozzles," NASA TN D–7602

Barna, P S , 1971, "Performance and Noise Generation Studies of Supersonic Air Ejectors " Proceedings of the Seventh International Congress on Acoustics, Budapest, Paper 24 N 15 pp 481–484

Benjamin M A , 1990, "A Methodology for the Design of a Two-Dimensional Constant Pressure Combustor Utilizing Reacting Shear-Layers," Master's Thesis, University of Florida, Gainesville Florida

Benjamin M A , 1994 "Pressure Measurement and Flowfield Characterization of a Two-Dimensional Ideally Expanded Constant Area, Air/Air Ejector " Ph D Dissertation, University of Florida, Gainesville, Florida.

Bevilaqua, P M 1974 "Evaluation of Hypermixing for Thrust Augmenting Ejectors " Journal of Aircraft Vol 2, No 6, pp 348–354

Birch, S F and Eggers J M 1973 "A critical Review of the Experimental Data for Developed Free Turbulent Shear Layers " NASA SP–321, pp 11–40

Bishop K. A , Ffowcs Williams J E. and Smith W. 1971 "On the Noise Sources of the Unsuppressed High-Speed Jet " Journal of Fluid Mechanics, Vol 50 Part 1 pp 21–32

Blumen W., 1970 "Shear Layer Instability of an Inviscid Compressible Fluid," Journal of Fluid Mechanics Vol 40 Part 4 pp 769–781

Blumen W Drazin P G and Billings D F 1975 "Shear Layer Instability of an Inviscid Compressible Fluid Part 2," Journal of Fluid Mechanics Vol 71 Part 2 pp 305–316

Bogdanoff D W 1983 "Compressibility Effects in Turbulent Shear Layers," AIAA Journal Vol 21, No 6 pp. 926–927

Bradshaw P 1966 "The Effect of Initial Conditions on the Development of a Free Shear Layer," Journal of Fluid Mechanics Vol 26 Part 2, pp. 225–236

Brown G B 1935, "On Vortex Motion in Gaseous Jets and the Origin of their Sensitivity to Sound," Proceedings of the Physical Society (London) Vol 47 pp 703–732

Brown G L. 1974 "The Entrainment and Large Scale Structure in Turbulent Mixing Layers Proceedings of the 5th Australasian Conference in Hydraulics and Fluid Mechanics, Christchurch New Zealand pp 352–359

Brown, G L. and Roshko, A., 1974, "On Density Effects and Large Scale Structure in Turbulent Mixing Layers," Journal of Fluid Mechanics Vol 64 Part 4 pp 775–816

Chinzei N Masuya, G Komuro, T, Murakami, A and Kudou, K. 1986, "Spreading of Two-stream Supersonic Turbulent Mixing Layers" Physics of Fluids, Vol 29 No 5 pp 1345–1347

Chow W L and Addy L 1964 "Interaction Between Primary and Secondary Streams of Supersonic Ejector Systems and Their Performance Characteristics," AIAA Journal Vol 2, No 4 pp 686–695

Chow W L and Yeh P S 1965 "Characteristics of Supersonic Ejector Systems with Nonconstant Area Shroud," AIAA Journal Vol 3 No 3, pp 525–527

Coles, D, 1985 "Dryden Lecture The Uses of Coherent Structure" AIAA 23rd Aerospace Science Meeting, Reno Nevada

Dash, S M Wolf D E. and Seiner, J M 1985 "Analysis of Turbulent Underexpanded Jets Part 1 Parabolized Navier-Stokes Model SCIPVIS AIAA Journal, Vol 23 No 4 pp 505–514

Davies, M G and Oldfield, D E. S 1962a, "Tones from a Choked Axisymmetric Jet. I. Cell Structure Eddy Velocity, and Source Locations," Acustica, Vol 12, No. 4, pp 257–266

Davies, M G and Oldfield D E S 1962b "Tones from a Choked Axisymmetric Jet. II. The Self Excited Loop and Mode of Oscillation" Acustica, Vol 12, No 4 pp 267–277

Dimotakis P E. 1986 "Two-Dimensional Shear Layer Entrainment," AIAA Journal Vol 24 No 11 pp 1791–1796

Dimotakis P E., 1989 "Turbulent Free Shear Layer Mixing" AIAA 27th Aerospace Sciences Meeting Reno Nevada, AIAA 89–0262

Dimotakis P E. and Brown G L. 1976 "The Mixing Layer at High Reynolds Number Large Structure Dynamics and Entrainment " Journal of Fluid Mechanics Vol 78 Part 3 pp 535–560

Dosanjh, D S , Abdelhamid, Amr N and Yu J C., 1969 "Noise Reduction from Interacting Coaxial Supersonic Jet Flows," Basic Aerodynamics Noise Research, NASA SP–207 pp 63–101

Dufflocq, M Benjamin, M A., Roan V P. 1993, "Comparison of Initial Development of Shear Layers in Two-Dimensional and Axisymmetric Ejector Configurations " AIAA/SAE/ASME/ASEE 29th Joint Propulsion Conference, Monterrey, California, AIAA 93–2440

Dufflocq, M , Benjamin M A., Roan V P and Lear W P. 1992 "Initial Development of the Axisymmetric Ejector Shear Layer." AIAA/SAE/ASME/ASEE 28th Joint Propulsion Conference Nashville Tennessee July AIAA 92–3567

Dutton, J C and Carroll B F 1983 "Optimized Ejector Diffuser Design Procedure for Natural Gas Vapor Recovery " ASME Journal of Energy Resources Technology Vol 105, No. 3, pp 388–393

Dutton, J C and Carroll B F , 1986, "Optimal Supersonic Ejector Designs," ASME Journal of Fluids Engineering Vol. 108 pp 414–420

Dutton J C , Mikkelsen, C D , and Addy A L , 1982 "A Theoretical and Experimental Investigation of the Constant Area, Supersonic-Supersonic Ejector," AIAA Journal, Vol 20 No 10 pp 1392–1400

Fabri J and Siestrunck, R. 1958 "Supersonic Air Ejectors," Advances in Applied Mechanics, Vol V (Dryden H L. and von Karman Th , eds.), Academic Press Inc , Publishers New York pp 1–34

Federspiel J F and Kuchar A P, 1988 "Performance Evaluation of a Two-Dimensional Convergent-Divergent Ejector Exhaust System," AIAA/ASME/SAE/ASEE 24th Joint Propulsion Conference Boston Massachusetts July AIAA 88–2999

Fox R W and McDonald A. T 1978 Introduction to Fluid Mechanics 2nd edition John Wiley & Sons New York

Glass D R 1968 "Effects of Acoustic Feedback on the Spread and Decay of Supersonic Jets," AIAA Journal Vol 6 No 10 pp 1890–1897

Goebel S G and Dutton J C , 1990, "An Experimental Investigation of Compressible Turbulent Mixing Layers," University of Illinois at Urbana-Champaign Technical Report UILU ENG 90-4005

Gutmark, E., Schadow, K. C., and Bicker, C. J., 1990. "Near Acoustic Field and Shock Structure of Rectangular Supersonic Jets," AIAA Journal, Vol. 28, No. 7, pp. 1163–1170.

Hammitt, A. G., 1961. "The Oscillation and Noise of an Overpressure Sonic Jet," Journal of the Aerospace Sciences, Vol. 28, No. 9, pp. 673–680.

Harper-Bourne, M. and Fisher, M. J., 1973. "The Noise From Shock Waves in Supersonic Jets," Proceedings (No. 131) of the AGARD Conference on Noise Mechanisms, Brussels, Belgium, pp. 11.1–11.13.

Hickman, K. H., Hill, P. G. and Gilbert, G. B., 1972. "Analysis and Testing of Compressible Flow Ejectors with Variable Area Mixing Tubes," ASME Journal of Basic Engineering, pp. 407–416.

Hill, P. G., 1965. "Turbulent Jets in Ducted Streams," Journal of Fluid Mechanics, Vol. 22, Part 1, 161–186.

Holman, J. P., 1978, Experimental Methods for Engineers, 3rd Edition, McGraw Hill, Inc., New York.

Hsia, Y. C., 1984, "An Experimental Investigation of an Underexpanded Rectangular Jet Ejector," Ph.D. Dissertation, Department of Aeronautics and Astronautics, Stanford University, California.

Keenan, J. H. and Neumann, E. P., 1942. "A Simple Air Ejector," ASME Journal of Applied Mechanics, pp. A-75–A-81.

Keenan, J. H., Neumann, E. P. and Lustwerk, F., 1950. "An Investigation of Ejector Design by Analysis and Experiment," ASME Journal of Applied Mechanics, Vol. 17, pp. 299–309.

Koochesfahani, M. M., Catherasoo, C. J., Dimotakis, P. E., Gharib, M. and Lang, D. B., 1979. "Two-Point LDV Measurements in a Plane Mixing Layer," AIAA Journal, pp. 1347–1351.

Konrad, J. H., 1976. "An Experimental Investigation of Mixing in Two-Dimensional Turbulent Shear Flows with Applications to Diffusion Limited Chemical Reactions," Ph.D. Dissertation, California Institute of Technology, California.

Krothapalli, A., Baganoff, D., and Hsia, Y., 1983. "On the Mechanism of Screech Tone Generation in Underexpanded Rectangular Jets," AIAA 8th Aeroacoustics Conference, AIAA 83–0727.

Krothapalli, A., Hsia, Y., Baganoff, D. and Karamcheti, K., 1982, "On the Structure of an Underexpanded Rectangular Jet," Joint Institute for Aeronautics and Acoustics Report TR–47, Stanford University, California.

Long M J 1992 "Experimental Investigation of an Ejector Powered Free-Jet Facility" AIAA/SAE/ASME/ASEE 28th Joint Propulsion Conference Nashville Tennessee AIAA 92 3569

Luffy R J and Hamed, A., 1992, "A Study on the Impact of Shroud Geometry on Ejector Pumping Performance," AIAA/ASME/SAE/ASEE 28th Joint Propulsion Conference, Nashville, Tennessee, AIAA 92–3260

Manin V, Pykhov, Z., and Rimski-Korsakov, A , 1971, 'Discrete Tone Radiation Arising From a Supersonic Jet Flowing into an Unlimited Gaseous Medium and into a Cylindrical Ejector," Proceedings of the Seventh International Congress on Acoustics Budapest, Paper 24 N 11, pp 469–472

Miles, J B and Shih J , 1968, "Similarity Parameter for Two-Stream Turbulent Jet-Mixing Region" AIAA Journal, Vol 6, No 7, pp 1429–1430

Nagaraja, K S Hammond D L and Graetch J E 1973 "One Dimensional Analysis of Compressible Ejector Flows Applicable to V/STOL Aircraft Design" AIAA 73–1184

Norum T D , 1983, "Screech Suppression in Supersonic Jets" AIAA Journal Vol 21 pp 235–240

Norum, T D and Seiner J M 1982, "Broadband Shock Noise from Supersonic Jets" AIAA Journal Vol 20, No 1 pp. 68–73

Pao S P and Seiner, J M , 1983 "Shock Associated Noise in Supersonic Jets," AIAA Journal Vol 21 No. 5 pp 687–693

Papamoschou D., 1986, "Experimental Investigation of Heterogeneous Compressible Shear Layers," Ph D Dissertation California Institute of Technology California.

Petersen, E. L. 1990. 'Experimental and Theoretical Investigation of Ejectors Employing Dissimilar Fluids" Master's Thesis University of Florida, Florida.

Petersen, E L Pfahler J N and Roan V P 1992, "Experimental Investigation of Supersonic Primary Dissimilar Fluid Ejectors" AIAA/SAE/ASME/ASEE 28th Joint Propulsion Conference Nashville Tennessee AIAA 92–3793

Poldervaart, L J , Vink A T and Wijnands A. P J , 1968 "The Photographic Evidence of the Feedback Loop of a Two Dimensional Screeching Supersonic Jet of Air" Proceedings of The 6th International Congress on Acoustics Tokyo, Japan, pp f101 f104

Pope A and Goin, K L., 1978 High Speed Wind Tunnel Testing, Robert E. Krieger Publishing Co , Malabar, Florida.

Porter J L and Squyers R A, 1978 "A Summary/Overview of Ejector Augmentor Theory and Performance Phase – II Technical Report," ATC Report No R–91100/9CR–47A Vol I – Technical Discussion, Vought Corporation Advanced Technology Center Dallas Texas

Porter, J L and Squyers, R. A., 1979 "A Summary/Overview of Ejector Augmentor Theory and Performance Phase – II Technical Report," ATC Report No R–91100/9CR–47A, Vol II – Bibliography Vought Corporation Advanced Technology Center, Dallas, Texas

Powell, A , 1953a, "On the Mechanism of Choked Jet Noise," Proceedings of the Physics Society Vol B66, pp 1039–1056

Powell A. 1953b, 'On the Noise Emanating from a Two-Dimensional Jet Above the Critical Pressure," The Aeronautical Quarterly Vol IV pp 103–122.

Quinn B 1973, "Compact Ejector Thrust Augmentation" Journal of Aircraft Vol 10 No 8 pp 481–486

Quinn, B 1975 "Effect of Aeroacoustic Interactions on Ejector Performance" Journal of Aircraft Vol 12 No 11 pp 914–916

Quinn B , 1976, "Ejector Performance at High Temperatures and Pressures Journal of Aircraft, Vol 13 No. 12, pp 948–954

Quinn, B 1977, "Interactions between Screech Tones and Ejector Performance," Journal of Aircraft Vol 14, No 5, pp 467–473

Roan, V P Jr , 1966 'On the Turbulent Mixing of Semi-Contained Compressible Streams at Constant Pressure and Small Relative Flow Angles," Ph D Dissertation, University of Illinois at Urbana, Illinois

Roan V P , 1991 "An Ejector Performance Correlation Factor," AIAA/SAE/ASME/ASEE 27th Joint Propulsion Conference Sacramento California, AIAA 91–2545

Roan, V P , Dufflocq M , and Benjamin M A 1993 'Ejector Code Calibration Investigation Phase II – Axisymmetric Tests," NASA Lewis Research Center, Contract Report No NAG3-1187

Roan V P Lear W E Dufflocq, M., and Benjamin, M A. 1992, 'Ejector Code Calibration Investigation Phase I – Axisymmetric Tests," NASA Lewis Research Center Contract Report No NAG3-1187

Rosfjord, T J and Toms H L., 1975 "Recent Observations Including Temperature Dependance of Axisymmetric Jet Screech," AIAA Journal Vol. 13, No 10, pp 1384–1386

Sabin, C. M., 1965, "An Analytical and Experimental Study of the Plane, Incompressible Turbulent Free Shear Layer with Arbitrary Velocity Ratio and Pressure Gradient," ASME Journal of Basic Engineering, pp. 421–428.

Schlichting, H. (J. Kestin transl.), 1979, Boundary-Layer Theory, 7th edition, McGraw Hill, New York, pp. 737–738.

Seiner, J. M., Dash, S. M., and Wolf, D. E., 1985, "Analysis of Turbulent Underexpanded Jets, Part II: Shock Noise Features Using SCIPVIS," AIAA Journal, Vol. 23, No. 5, pp. 669–677.

Seiner, J. M. and Yu, J. C., 1984, "Acoustic Near Field Properties Associated with Broadband Shock Noise," AIAA Journal, Vol. 22, No. 9, pp. 1207–1215.

Shapiro, A. H., 1953, The Dynamics and Thermodynamics of Compressible Fluid Flow, Volume I, John Wiley & Sons, New York.

Shapiro, A. H., 1954, The Dynamics and Thermodynamics of Compressible Fluid Flow, Volume II, Robert E. Krieger Publishing Co., Malabar, Florida.

Succi, G. P., Baumeister, K. J., and Ingard, K. U., 1978, "Interaction of a Turbulent-Jet Noise Source with Transverse Modes in a Rectangular Duct," NASA TP–1248.

Tam, C. K. W., 1972, "On the Noise of Nearly Ideally Expanded Supersonic Jet," Journal of Fluid Mechanics, Vol. 51, Part 1, pp. 69–95.

Tam, C. K. W., 1986, "On the Screech Tones of Supersonic Rectangular Jets," AIAA 10th Aeroacoustics Conference, Seattle, Washington, AIAA 86–1866.

Tam, C. K. W., 1993, "Screech Tones from Free and Ducted Supersonic Jets," 31st Aerospace Science Meeting and Exhibit, Reno, Nevada, AIAA 93–0732.

Tam, C. K. W., Jackson, J. A., and Seiner, J. M., 1985, "A Multiple Scale Model of the Shock-Cell Structure of Imperfectly Expanded Supersonic Jets," Journal of Fluid Mechanics, Vol. 153, pp. 123–149.

Tam, C. K. W. and Tanna, H. K., 1982, "Shock Associated Noise of Supersonic Jets From Convergent Divergent Nozzles," Journal of Sound and Vibration, Vol. 81, No. 3, pp. 337–358.

Tanna, H. K., 1977, "An Experimental Investigation of Jet Noise, Part II: Shock Associated Noise," Journal of Sound and Vibration, Vol. 50, No. 3, pp. 429–444.

Viets, H., Campell, J. R., and Korhan, K. D., 1981, "Acoustic Interactions in Ejectors," AIAA 7th Aeroacoustics Conference, Palo Alto, California, AIAA 81–2045.

Westley, R. and Wooley, J. H., 1968, "An Investigation of the Near Noise Fields of a Choked Axisymmetric Air Jet," Proceedings of the AFSOR UTIAS Symposium on Aerodynamic Noise, Toronto, Canada, pp. 147–167.

White, F. M., 1994, Fluid Mechanics, 3rd Edition, McGraw Hill, Inc., New York.

Winant, C. D. and Browand, F. K., 1974, "Vortex Pairing: the Mechanism of Turbulent Mixing Layer Growth at Moderate Reynolds Number," Journal of Fluid Mechanics, Vol. 63, pp. 237–255.

Yu, C. J. and Dosanjh, D. S., 1972, "Noise Field of a Supersonic Mach 1.5 Cold Model Jet," Journal of the Acoustical Society of America, Vol. 51, No. 5 (Part 1), pp. 1400–1410.

Yule, A. J., 1972, "Spreading of Turbulent Mixing Layers," AIAA Journal, Vol. 10, No. 5, pp. 686–687.

BIOGRAPHICAL SKETCH

Maximiano F. Dufflocq was born in Santiago, Chile, on September 27, 1961. Upon finishing high school he attended Gulf Coast Community College in Panama City, Florida. After transferring to the University of Florida, he pursued an education in mechanical engineering, receiving a Bachelor of Science in mechanical engineering with high honors in May 1984, and a Master of Engineering in mechanical engineering in August 1988

I certify that I have read this study and that in my opinion it conforms to acceptable standards of scholarly presentation and is fully adequate, in scope and quality, as a dissertation for the degree of Doctor of Philosophy

Vernon P. Roan

Vernon P. Roan, Jr., Chair
Professor of Mechanical
Engineering

I certify that I have read this study and that in my opinion it conforms to acceptable standards of scholarly presentation and is fully adequate, in scope and quality, as a dissertation for the degree of Doctor of Philosophy

William E. Lear

William E. Lear
Assistant Professor of Mechanical
Engineering

I certify that I have read this study and that in my opinion it conforms to acceptable standards of scholarly presentation and is fully adequate, in scope and quality, as a dissertation for the degree of Doctor of Philosophy

James F. Klausner

Jim Klausner
Associate Professor of Mechanical
Engineering

I certify that I have read this study and that in my opinion it conforms to acceptable standards of scholarly presentation and is fully adequate, in scope and quality, as a dissertation for the degree of Doctor of Philosophy

Elmer C. Hansen

Elmer C. Hansen
Assistant Professor of Mechanical
Engineering

I certify that I have read this study and that in my opinion it conforms to acceptable standards of scholarly presentation and is fully adequate, in scope and quality, as a dissertation for the degree of Doctor of Philosophy

Ulrich Kurzweg

Ulrich H. Kurzweg
Professor of Aerospace Engineering,
Mechanics, and Engineering Science

This dissertation was submitted to the Graduate Faculty of the College of Engineering and to the Graduate School and was accepted as partial fulfillment of the requirements for the degree of Doctor of Philosophy

August, 1996

Winfred M. Phillips
Dean, College of Engineering

Karen A. Holbrook
Dean, Graduate School